

Insights into Catalyst Degradation During Alkaline Water Electrolysis Under Variable Operation

Raul A. Marquez,¹ Jay T. Bender,² Ashton M. Aleman,^{3,4} Emma Kalokowski,¹ Thuy Vy Le,¹ Chloe Williamson,² Morten Linding Frederiksen,⁵ Kenta Kawashima,¹ Chikaodili E. Chukwuneke,¹ Andrei Dolocan,⁶ Delia J. Milliron,^{1,2,7,8} Joaquin Resasco,^{2,8} Thomas F. Jaramillo,^{3,4} and C. Buddie Mullins^{1,2,6,7,8,}*

¹ Department of Chemistry, The University of Texas at Austin, Austin, TX 78712, USA.

² McKetta Department of Chemical Engineering, The University of Texas at Austin, Austin, TX 78712, USA.

³ Department of Chemical Engineering, Stanford University, Stanford, CA 94305, USA.

⁴ SUNCAT Center for Interface Science and Catalysis, SLAC National Accelerator Laboratory, Menlo Park, CA 94025, USA

⁵ Department of Biological & Chemical Engineering, Aarhus University, Aarhus N 8200, Denmark

⁶ Texas Materials Institute, The University of Texas at Austin, Austin, Texas 78712, USA.

⁷ Allen J. Bard Center for Electrochemistry, The University of Texas at Austin, Austin, Texas 78712, USA.

⁸ H2@UT, The University of Texas at Austin, Austin, Texas 78712, USA.

* Corresponding author: mullins@che.utexas.edu

Number of pages: 140

Number of figures and schemes: 94

Number of tables: 2

Table of Contents

S1. Materials and reagents	4
S2. General electrode preparation	6
Substrate preparation	6
Film electrodeposition	7
Electrode naming scheme	8
S3. General electrochemical methods	9
Electrochemical cell setup	9
Reference electrodes	11
General voltammetry measurements and iR compensation	12
Electrochemical conditioning	13
S4. Simulated shutdown tests to study electrode discharge	15
Experimental setup	15
Measurement of the open circuit potential decay	15
Measurement of corrosion potentials from potentiodynamic polarization tests	16
S5. Accelerated catalyst degradation tests in a three-electrode cell.....	17
Experimental setup	17
Variable operation tests	17
S6. Measurement of reverse current effects using in situ SERS	19
Electrode preparation	19
In situ SERS measurements	20
Electrochemical measurements	21
S7. Chemical composition analysis via ToF-SIMS	23
S8. In-plane conductivity measurements using IDA electrodes	25
Film preparation and characterization	25
In-plane conductivity measurements	27
In-plane effective conductivity calculation.....	28
S9. Metal dissolution analysis via ICP-MS.....	29
Electrochemical flow cell setup	29
ICP-MS measurements	29
Electrochemical measurements	30
ICP-MS data analysis	31

S10. Accelerated catalyst degradation tests in a zero-gap electrolyzer	32
Electrode preparation	32
Zero-gap water electrolyzer experimental setup	33
Potentiostat configuration	34
Estimation of the reverse current for variable operation tests	35
Extended variable operation experiments	36
Ex situ X-ray photoelectron spectroscopy analysis	39
Ex situ ICP-MS measurements	40
Supporting Figures, Tables, and Schemes	42
Simulated shutdown tests to study electrode discharge	42
Accelerated catalyst degradation tests in a three-electrode cell.....	55
Measurement of reverse current effects using in situ SERS	79
Chemical composition analysis via ToF-SIMS.....	92
In-plane conductivity measurements using IDA electrodes	98
Metal dissolution analysis via ICP-MS.....	100
Accelerated catalyst degradation tests in a zero-gap water electrolyzer.....	104
References	137

S1. Materials and reagents

All the electrolytes were prepared with CO₂-free deionized (DI) water (18.2 MΩ·cm). Deionized water was boiled in a 1 L borosilicate Florence flat-bottom flask to remove CO₂, allowed to cool to room temperature in the sealed flask, and stored in polypropylene bottles wrapped with Parafilm. KOH electrolytes were prepared from reagent-grade potassium hydroxide flakes (Sigma Aldrich, 89.5% according to the certificate of analysis). Semiconductor-grade KOH (Sigma Aldrich, 99.98%) was used for inductively coupled plasma mass spectrometry (ICP-MS) experiments only. Water electrolysis tests were performed using unpurified electrolytes unless otherwise indicated. We employed established purification protocols to remove Fe impurities from KOH electrolytes.^{1,2} KOH concentrations were estimated via standard acid-base titration following established guidelines.¹ Primary standard potassium hydrogen phthalate (Thermo Scientific, ACS grade, 99.95 – 100.05%) was used for acid-base titrations.

Nickel(II) nitrate hexahydrate (Thermo Scientific, Puratronic, 99.9985% metal basis) was used for Fe purification and Ni(OH)₂ film electrodeposition. Iron(II) chloride tetrahydrate (Thermo Scientific, 99.94% metal basis) and sodium nitrate (Thermo Scientific, 99+%) were used for films containing codeposited Fe, while cobalt(II) nitrate hexahydrate was used for films containing Co. Ethanol (Pharmco, 99.5%) was used to clean metal substrates. High-purity hydrochloric acid (Thermo Scientific, 99.999% metal basis) was used to prepare 3 M HCl solutions for cleaning metallic substrates. Acid dilutions for cleaning glassware and ICP-MS analysis were prepared using TraceMetal grade nitric acid (Fisher Scientific, 67 - 70%, Fe < 1 ppb).

Ti foil (Thermo Scientific, 99.5%, annealed) with a thickness of 0.1 mm was used as the substrate for electrocatalytic film deposition. Ni foil (Thermo Scientific, 99.5%, annealed) with a thickness of 0.1 mm was used as the working electrode in control experiments. Ni foam (MTI, 99.99%, 80 - 110 ppi) with a thickness of 1.6 mm was used as a counter electrode during film electrodeposition. The thickness of the Ni foam electrodes was reduced to 800 μ m using a roller press. Nickel gauze (Thermo Scientific, 100 mesh woven from 0.1mm wire) was used as the electrode for zero-gap electrolyzer tests. Screen-printed gold electrodes (Metrohm, DRP-220BT-U75), with a working electrode diameter of 4 mm, were used for in situ SERS experiments. Interdigitated array gold electrodes (Metrohm, DRP-G-IDEAU5), with lines/gaps of 5 μ m, were used for in-plane in situ conductivity measurements.

Reagent-grade potassium phosphate (KPi, Sigma Aldrich, 99.9%, per certificate of analysis) was used to spike PO_4^{3-} into 0.1 M KOH electrolytes for variable operation in a three-electrode cell, in situ SERS, and on-line ICP-MS experiments. Note: The KPi electrolyte is not technically a phosphate-buffered saline (PBS) solution, as neither sodium nor potassium chloride were added to the solution to avoid interference with the OER.³ Iron(III) nitrate nonahydrate (Thermo Scientific, Puratronic, >99.995% metal basis) was used to spike Fe^{3+} into purified 1 M KOH electrolyte for conditioning the Fe-doped Ni mesh anode (i.e., O_2 electrode). Potassium chloride (Sigma-Aldrich, ~3 M KCl saturated with AgCl) was used for roughening Au substrates. We used the ZIRFON PERL UTP 500 (Agfa) separator and silicone gaskets (Arlon, 10-6075FS-2-0.015) in all zero-gap alkaline water electrolyzer experiments.

S2. General electrode preparation

Substrate preparation

Ti foil pieces ($20 \times 10 \times 0.1$ mm) were cut and immersed in ethanol within shell type 1 glass vials (Fisher Scientific, 15×45 mm), placed in an ultrasonic bath for 15 minutes, and dried overnight in a vacuum oven at 60°C . The exposed electrode surface area was fixed using a polydimethylsiloxane (PDMS) coating (SYLGARD 184 Silicone Elastomer Kit, Dow). The coating was prepared by vigorously mixing the curing elastomer base and the curing agent in a 10:1 ratio for 10 min using a polytetrafluoroethylene (PTFE) rod. Next, this mixture was degassed in a vacuum oven for about 5 minutes or until no bubbles remained visible. The liquid PDMS mixture was carefully applied to a 5 mm segment extending from the foil's center towards its right and rear sides, exposing a $10 \times 10 \text{ mm}^2$ area on one side. A 5 mm flat portion was intentionally left uncoated to serve as a clipping region. The PDMS-coated Ni foil pieces were cured in a small oven at 150°C for 10 min as recommended by the manufacturer. After curing, the electrodes were kept in a vacuum oven until use. Prior to electrodeposition, the PDMS-coated electrodes were placed inside clean shell type 1 vials and sequentially cleaned for 15 minutes each in three solutions: (1) ethanol, (2) 3 M HCl, and (3) DI water.

Ni gauze strips ($20 \times 65 \times 0.1$ mm) were used as electrodes for zero-gap alkaline electrolyzer tests. The strips were sequentially cleaned in ethanol, 3 M HCl, and DI water for 15 min each inside 50 mL beakers. No PDMS coating was applied, as the gaskets defined the projected geometric area (vide infra).

Film electrodeposition

We deposited electrocatalytic films on Ti foil substrates using a thin-film architecture to minimize electrical conductivity and mass transport effects.⁴ Following previous studies,^{2,4,5} hydroxide catalyst films were cathodically deposited using a two-electrode configuration from 20 mM metal(II) nitrate aqueous solutions. The pH of the plating bath was adjusted to ~3 using 1 M nitric acid. A 50 mL glass cell, pre-cleaned with nitric acid, was filled with ~15 mL of the plating bath and purged with N₂ gas for 5 min. A Ni foam counter electrode (geometric area: 2 x 2 cm²) was positioned 1 cm from the working electrode. To prevent cross-contamination, a fresh Ni foam counter electrode was used for each deposition of the same film type. The working electrode was secured with a Ti clip holder and aligned parallel to the counter electrode.

Films were deposited galvanostatically at -1 mA·cm⁻² for 90 s, corresponding to a total deposition charge of 90 mC·cm⁻² (thickness: ~110 nm). Electrodeposition was performed without stirring in three 30 s intervals, separated by 10 s resting periods to minimize concentration gradients.⁶ A constant flow of N₂ gas was maintained in the headspace to keep a positive pressure within the cell and prevent O₂ from entering. For films containing codeposited Fe and Co, the total metal content in the solution was maintained at 20 mM. For example, NiFe films were deposited from a solution of 10 mM Fe(II) and 10 mM Ni(II) nitrates, adjusted to pH ~3. While nitrate salts of Ni and Co were used directly, Fe-containing films were prepared using FeCl₂·4H₂O and NaNO₃ to prevent precipitation of insoluble Fe oxides/hydroxides. This solution was freshly prepared on the day of Fe film deposition and purged with N₂ before and after adding FeCl₂. A stoichiometric amount of NaNO₃ was added

to maintain a consistent nitrate concentration across all plating baths. After deposition, films were rinsed with DI water and dried in a vacuum oven until use. Fe-containing films were tested immediately after deposition. Co and Fe contents in bimetallic samples were quantified using energy-dispersive X-ray spectroscopy (EDX) and inductively coupled plasma mass spectrometry (ICP-MS).

Note: Despite the challenges associated with using Ti as a substrate, primarily the formation of insulating oxide layers that increase contact impedance,⁷ we selected Ti to distinguish between catalyst and substrate effects. Based on our experience, Ti also offers greater convenience and better adhesion than other substrates, such as fluorine-doped tin oxide (FTO)-coated glass or glassy carbon.

Electrode naming scheme

Electrodes are named based on their substrate and initial chemical composition:

Substrate abbreviation: Three substrates were used, Ti foil substrate (TF), screen-printed electrode with roughened gold working electrode (Au SPE), and gold interdigitated array (IDA Au) electrodes.

Chemical composition: Names reflect only the metals initially deposited before conditioning or aging. For example, Ni indicates nickel deposition only, while NiFe refers to nickel and iron bimetallic films. For Fe-doped Ni mesh anodes, Fe was incorporated during a pre-conditioning step rather than initial deposition.

Chemical phase: Oxyhydroxide films underwent electrochemical conditioning. Hydroxide films refer to as-deposited films that have not been conditioned.

S3. General electrochemical methods

Electrochemical cell setup

For three-electrode cell experiments, a 100 mL PTFE cell was used to prevent glassware contamination in alkaline electrolytes.¹ The cell was cleaned before and after experiments with 3 M HNO₃ and rinsed thoroughly with DI water. All electrochemical measurements were conducted using a Gamry Reference 620 potentiostat/galvanostat. Additional potentiostats were used for specific measurements: a CH Instruments CHI 832 bipotentiostat for in-plane in situ conductivity measurements, a BioLogic VSP-300 potentiostat for on-line ICP-MS measurements, and a Gamry Interface 1010E potentiostat/galvanostat to monitor the total cell potential in zero-gap alkaline water electrolyzer experiments.

To prevent incidental Pt incorporation,⁸ graphite rods (Gamry, diameter: 6 mm) were used as counter electrodes in all three-electrode cell experiments. Counter electrodes were stored in DI water and periodically cleaned by soaking in 3 M HNO₃. Each catalytic film composition (e.g., Ni hydroxide, Co hydroxide) was tested with a dedicated set of fresh and clean graphite rods and a PTFE cell to prevent cross-contamination.

All current densities were calculated based on the projected geometric area. For catalytic films deposited on Ti foil substrates, the geometric area ($\sim 1 \text{ cm}^2$) was defined using a PDMS coating, which prevented the electrolyte from interacting with the bare Ti foil. This ensured that only the $\sim 1 \text{ cm}^2$ region containing the electrocatalytic film was converted into the active NiOOH phase during electrochemical conditioning. Details on the preparation and application of the PDMS coating were adapted from previous studies,^{1,9} and can be

found in Section S2. The geometric area was precisely measured using non-contact profilometry (NCP) with a Keyence VK-X1100 optical profilometer. For zero-gap alkaline electrolyzer tests, the projected geometric area was defined by the gaskets and measured 4 cm², as detailed elsewhere.¹⁰ The geometric areas for in situ SERS, on-line ICP-MS, and conductivity measurements are specified in their sections below.

Fresh KOH electrolytes were prepared and standardized for each electrochemical test following our previous guidelines.¹ Before electrochemical tests, electrolytes were degassed with high-purity O₂ for 30 min using a plastic bubbler. To ensure reproducibility, magnetic stirring was used only after degassing to dislodge bubbles but not during electrochemical tests. A continuous flow of O₂ or H₂ was maintained in the headspace during tests using a three-electrode cell configuration. **Note:** high-purity H₂ was used in electrode discharge experiments under cathodic constant currents (e.g., **Fig. S7**).

Unpurified KOH electrolytes were used for variable operation tests to maintain industrial relevance. Rather than purifying all electrolytes, we aimed to keep Fe impurity concentrations consistent across experiments, as highlighted by previous works.¹¹⁻¹³ Purifying all electrolytes, especially 7 M KOH, is more time-consuming, can introduce Ni impurities, and deviates from industrial conditions essential to this study. Maintaining a known Fe concentration in a large batch of electrolyte improved experimental reproducibility compared to complete purification. For each concentration used in this study (0.1, 1, and 7 M), a single large batch (~3.5 L) was prepared and analyzed for key metrics (**Table S1**). Fe and Ni concentrations were determined using solution-mode inductively coupled plasma mass spectrometry (ICP-MS) following our previous protocol.¹

Table S1. Properties of KOH electrolytes used in this study.

Nominal KOH electrolyte concentration	Concentration ($\text{mol}\cdot\text{L}^{-1}$)	Fe concentration (ppb)	Ni concentration (ppb)
0.1 M (batch #1)	0.100 ± 0.004	5.2 ± 1.6	1.9 ± 0.7
0.1 M (batch #2)	0.100 ± 0.005	6.3 ± 0.9	2.3 ± 0.6
1 M (batch #1)	0.991 ± 0.032	67.2 ± 5.1	23.3 ± 3.7
7 M (batch #1)	6.965 ± 0.064	498.2 ± 19.1	105.8 ± 10.2

Uncertainties represent the standard deviation from three samples from the same electrolyte batch.

Reference electrodes

Electrode potentials were measured against Hg/HgO reference electrodes (CH Instruments) in all experiments. Three Hg/HgO reference electrodes were used, each with a filling solution matching its intended electrolyte: unpurified 0.1 M KOH, unpurified 1 M KOH, and purified 1 M KOH. The reference electrodes were stored separately in plastic containers filled with their respective electrolytes and were regularly calibrated against a dedicated saturated calomel electrode (SCE).

Potentials were converted to the reversible hydrogen electrode (RHE) using **Eq. 1:**

$$E_{\text{RHE}} = E_{\text{Hg/HgO}}^{\circ} + 0.0592(\text{pH}) + E_i \quad (1)$$

where E_i is the measured potential vs. Hg/HgO. The value of $E_{\text{Hg/HgO}}^{\circ}$ KOH was determined experimentally by measuring the open-circuit potential (OCP) for 5 min against the SCE. The value of $E_{\text{Hg/HgO}}^{\circ}$ was corrected for the liquid junction potential (LJP) according to **Eq. 2:**¹⁴

$$E_{\text{Hg/HgO}}^{\circ} = E_{\text{OCP}} + E_{\text{SCE}}^{\circ} - E_{\text{LJP}} \quad (2)$$

where E_{OCP} is the measured OCP value, E_{SCE}° is the half-cell standard reduction potential of the SCE (0.2412 V vs. SHE at 25 °C, KCl sat.), and E_{LJ} is the liquid junction potential difference (-0.1 mV for KCl sat.|0.1 M KOH and 6.4 mV for KCl sat.|1 M KOH).¹⁴ The experimentally determined values of $E_{\text{Hg/HgO}}^{\circ}$ were determined to be 106.0 ± 1.8 mV in 1 M KOH and 128.3 ± 4.1 mV in 0.1 M KOH. These values were periodically monitored to ensure stability between experiments.

Additionally, the SCE was calibrated using a standard hydrogen electrode (SHE) to correct for potential drift.^{14,15} The SHE was constructed with a platinized Pt electrode in an acidic electrolyte with unit activity of H⁺ and H_{2,(g)} (1 bar). The reversible hydrogen potential was estimated as the average between forward and reverse sweeps around the potential of zero current. Further details can be found elsewhere.^{14,16,17} An Ag/AgCl reference electrode (BASi RE-6, 3 M NaCl) was exclusively used for on-line ICP-MS measurements ($E_{\text{Ag/AgCl (3M NaCl)}}^{\circ} = 0.209$ V). Potentials were converted to the RHE scale using **Eqs. 1 and 2**, replacing $E_{\text{Hg/HgO}}^{\circ}$ with $E_{\text{Ag/AgCl (3M NaCl)}}^{\circ}$ and calculating the liquid junction potentials as described elsewhere.¹⁴

General voltammetry measurements and iR compensation

The OCP was measured for one hour before experiments or until the potential stabilized completely (typically between -0.05 and -0.15 V vs. Hg/HgO, with a ±5 mV variation). Unless otherwise specified, linear sweep voltammetry (LSV) and cyclic voltammetry (CV) scans were recorded at slow scan rates (1 or 5 mV·s⁻¹) to minimize capacitive contributions, with the third scan reported for all measurements.

Unless otherwise specified, electrode potentials were corrected for 85% uncompensated resistance (R_u) using the positive feedback mode in Gamry software. This iR compensation method is essential for testing transition metal-based oxides/hydroxides.⁷

The $E_{iR\text{-free}}$ value was estimated using **Eq. 3:**

$$E_{iR\text{-free}} = E - iR_u \quad (3)$$

where E is the electrode potential, and i denotes the current at the corresponding potential. R_u was determined via electrochemical impedance spectroscopy (EIS) by identifying the minimum total impedance at high frequencies (80–30 kHz). Measurements were taken at a stable OCP with a 5 mV amplitude, where the phase angle approaches zero, minimizing both capacitive and inductive impedances.^{2,18} The value of R_u varied depending on the catalyst film composition and electrolyte concentration. For instance, R_u was typically $\sim 13 \Omega$ for Ni(OH)₂ films deposited on Ti foil substrate and tested in unpurified 0.1 M KOH (**Fig. S14e**). Supplementary Nyquist plots in this document show the range of R_u values across different conditions. Importantly, R_u was measured after electrode conditioning to ensure the formation of a thin oxyhydroxide layer.

Electrochemical conditioning

The electrodes were conditioned via chronopotentiometry (CP) at a constant current density to favor the formation of a thin and compact hydrous oxide layer on the surface.¹⁹ The specific current densities and times depend on the type of experiment and cell configuration and are detailed below for each specific test. The electrolyte was stirred with a magnetic stir bar (three-electrode cell tests) or circulated at a flow rate of 200 mL·min⁻¹

(zero-gap electrolyzer tests) for 10 min before and after conditioning to dislodge bubbles. Electrochemical conditioning was typically followed by an EIS measurement under open-circuit conditions to measure the R_u value (three-electrode cell tests) or the high-frequency resistance (HFR, electrolyzer experiments) once the active oxyhydroxide phase formed on the surface. Then, electrochemical measurements were performed.

S4. Simulated shutdown tests to study electrode discharge

Experimental setup

Experiments were carried out in a three-electrode PTFE cell (**Fig. S1**) using a Hg/HgO reference electrode and a graphite rod counter electrode. The working electrode consisted of a Ti foil substrate coated with a transition metal hydroxide film, electrodeposited galvanostatically (deposition charge: $90 \text{ mC}\cdot\text{cm}^{-2}$, thickness: $\sim 110 \text{ nm}$). Three films were tested: Ni(OH)_2 , NiCo(OH)_2 , and NiFe(OH)_2 . The cell contained 40 mL of KOH electrolyte (0.1, 1, or 7 M, depending on the experiment). After assembly, the OCP was monitored for 300 s or until a stable response was achieved. The electrode was then conditioned via CP for 300 s at $5 \text{ mA}\cdot\text{cm}^{-2}$ for anodic tests or $-5 \text{ mA}\cdot\text{cm}^{-2}$ for cathodic tests. Following conditioning, a potentiostatic EIS measurement (DC potential: 0 V, frequency range: 200 to 0.1 kHz, ten points per decade, AC voltage: 5 mV, with drift correction enabled) was carried out to determine the R_u value, and the electrode discharge experiment was conducted immediately afterward.

Measurement of the open-circuit potential decay

A CP step was applied for 480 s at the specified current density. Immediately afterward, a fast two-step measurement, combining a CP step (10 s, same current density) followed by an OCP step (30 s), was performed to capture the rapid discharge of the electrode after the constant current step. This measurement was performed with a sampling period of 5×10^{-4} s. Next, an OCP measurement lasting 1 hour was recorded, with a sampling period of 0.25 s. These three steps constitute a single electrode discharge experiment (e.g., **Fig. S2b**). For

example, the fast two-step CP-OCP sequence is illustrated in **Fig. S2a**. **Note:** 100% iR compensation for CP steps was carried out manually using the R_u value from the initial EIS measurement and calculated using **Eq. 3**.

Measurement of corrosion potentials from potentiodynamic polarization tests

Following the electrode discharge experiment, the OCP was monitored in a subsequent experiment for 55 min to ensure it stabilized at a constant value. Next, a potentiodynamic polarization test (referred to as a "*Tafel scan*" in the Gamry Framework software under the DC corrosion package) was carried out, following established corrosion testing protocols.²⁰⁻²³ The potential window was set at ± 150 mV around the stabilized OCP, and the scan was conducted at a rate of 0.16667 mV·s⁻¹ with a sampling period of 0.5 s. **Note:** In certain experiments (e.g., **Fig. S11c**), the anodic potential was extended beyond 150 mV above the OCP to maintain a consistent potential window across all measurements and facilitate comparison.

S5. Accelerated catalyst degradation tests in a three-electrode cell

Experimental setup

Experiments were carried out in a three-electrode PTFE cell (**Fig. S1**) using an Hg/HgO reference electrode and a graphite rod counter electrode. The working electrode consisted of a Ti foil substrate coated with a transition metal hydroxide film, electrodeposited galvanostatically (deposition charge: 90 mC·cm⁻², thickness: ~110 nm). Four films were tested: Ni(OH)₂, Co(OH)₂, NiCo(OH)₂, and NiFe(OH)₂. The cell contained 40 mL of unpurified 0.1 M KOH electrolyte. After assembly, the OCP was monitored for 300 s or until a stable response was achieved. The electrode was then conditioned via CP for 300 s at 5 mA·cm⁻². Following conditioning, a potentiostatic EIS measurement was carried out to determine the R_u value (DC potential: 0 V, frequency range: 200 to 0.1 kHz, ten points per decade, AC voltage: 5 mV, with drift correction enabled).

Variable operation tests

An automatic sequence made using the Gamry Sequence Wizard was used to run the experiment, structured into three main sections: initial assessment, stability cycling loop, and final assessment. The initial assessment included three LSV scans (0–0.85 V vs. Hg/HgO, 5 mV·s⁻¹, step size: 1 mV, 85% *iR* compensation using positive feedback) and a potentiostatic EIS measurement conducted at the potential recorded during CP conditioning (200 kHz to 0.1 Hz, ten points per decade, AC voltage: 5 mV, drift correction enabled).

A single stability cycling loop consisted of two CP steps: a 10-min step at $50 \text{ mA}\cdot\text{cm}^{-2}$, followed by a 5-min reverse current step at $-5 \text{ mA}\cdot\text{cm}^{-2}$. The reverse step was immediately followed by a potentiostatic EIS measurement at the potential recorded during CP conditioning (200 kHz to 0.5 Hz, ten points per decade, AC voltage: 5 mV, drift correction enabled). For steady-state current tests, the cycling loop included only the step at $50 \text{ mA}\cdot\text{cm}^{-2}$, extended to 15 min; for variable steps under OCP, the second step was conducted at 0 mA. The loop was repeated 30 times for steady-state current tests and 60 times for reverse current tests. In certain reverse current experiments, the test was stopped at earlier cycles due to a significant increase in cell potential as a safety measure for the potentiostat. For the Ni foil anode experiment, the loop was cycled 120 times.

The final assessment included three LSV scans and a potentiostatic EIS measurement conducted under the same conditions as the initial assessment. Except for LSV scans, 100% iR compensation for CP steps was carried out manually using the R_u value from the initial EIS measurement and calculated using **Eq. 3**.

S6. Measurement of reverse current effects using *in situ* SERS

Electrode preparation

Ni(OH)₂, NiCo(OH)₂, and NiFe(OH)₂ films were deposited on screen-printed electrodes (SPEs), where Au served as both the working and counter electrode. First, the Au SPE was electrochemically roughened by applying ~100 µL of 0.1 M KCl saturated with AgCl onto the SPE and performing 30 CV scans from -0.3 to 1.3 V vs. Ag at 50 mV·s⁻¹. Films were cathodically deposited in a two-electrode configuration from 20 mM metal(II) nitrate aqueous solutions, with the plating bath pH adjusted to ~3 using 1 M nitric acid. A 50 mL pre-cleaned glass cell was filled with ~15 mL of the plating bath and purged with N₂ gas for 5 min. A Ni foam counter electrode (geometric area: 2 x 2 cm²) was positioned 1 cm from the working electrode, and a fresh Ni foam counter electrode was used for each deposition of the same film type to prevent cross-contamination. The SPE was secured to a Ti clip holder, ensuring electrical contact only with the working and counter electrode terminals, restricting film deposition to the gold surfaces.

Thin catalyst films were deposited galvanostatically at -1 mA·cm⁻² for 50 s (total charge: 50 mC·cm⁻², thickness: ~90 nm, determined by NCP measurements). After deposition, films were rinsed with DI water and stored in a vacuum oven until further use. Importantly, the electrodeposited films were not uniformly distributed on the surface, with noticeable particle agglomerates in certain regions of the rough Au surface. NCP images illustrating this morphology were reported in our previous study.⁹ The metal ratio in bimetallic films was nominally 1:1 according to EDX and ICP-MS measurements.

In situ SERS measurements

Experiments were conducted in a custom electrochemical cell (**Fig. S38**). Using a dedicated port in the cell design, an Hg/HgO reference electrode was directly integrated into the cell without the PTFE Luggin capillary. A Ni foam counter electrode (projected geometric area: 1.33 cm²) was placed at the bottom of the cell, while metal hydroxide films deposited on rough Au SPEs served as the working electrodes positioned at the top of the cell, just beneath the visualization window. The window consisted of a circular PFA film (Chemours, thickness: 0.0005 in) separated from the SPE surface by a PDMS gasket (thickness: 500 µm). The cell was filled with unpurified 0.1 M KOH (~3 mL), completely removing air bubbles. Once assembled, the cell was placed directly beneath the microscope objective.

Raman measurements were carried out using a Horiba LabRAM ARAMIS confocal Raman microscope equipped with a 50× magnification objective (Olympus LMPLFLN). A 633 nm laser was operated at 5% of its total power (2.5 mW). Based on the numerical aperture of the objective (NA = 0.5), the estimated laser spot size was ~1.3 µm. Calibration was verified before measurements using a silicon wafer with a reference peak of 520.7 cm⁻¹. Spectra were recorded with a 1 cm⁻¹ resolution, centered at 500 cm⁻¹.

Spectra collection varied depending on the experiment: (1) for multistep chronoamperometry (CA) runs used to construct polarization curves (e.g., **Fig. S39a**), spectra were collected during each CA step with an acquisition time of 60 s and three accumulations; (2) for electrode discharge experiments (e.g., **Figs. 3** and **S41**), each spectrum was acquired in a single accumulation with a 10 s acquisition time; (3) for variable

operation experiments (e.g., **Fig. S46**), spectra collected during both constant current and reverse steps had an acquisition time of 60 s with three accumulations.

Importantly, Raman signal intensity was significantly enhanced when the laser beam was positioned near the edges of visible particle agglomerates rather than directly on top. Researchers replicating these measurements should carefully optimize laser positioning, roughening of the gold substrate, and film electrodeposition, as these are critical for obtaining strong, well-defined signals in SERS measurements.

Electrochemical measurements

After assembly, the OCP was monitored for 300 s or until a stable response was achieved. The electrode was then conditioned via CP for 180 s at 0.5 mA·cm⁻². Following conditioning, a potentiostatic EIS measurement was carried out to determine the R_u value (DC potential: 0 V, frequency range: 200 to 0.1 kHz, ten points per decade, AC voltage: 5 mV, with drift correction enabled). Once the film was oxidized to the metal oxyhydroxide phase, spectra were collected at various locations to obtain strong metal oxyhydroxide bands between 450 and 560 cm⁻¹. This step was essential to ensure that *in situ* SERS measurements were conducted at an optimal location. Once a suitable spot was identified, the electrode was reduced to the hydroxide phase via CP for 180 s at -0.5 mA·cm⁻², after which *in situ* SERS experiments were conducted.

For multistep CA (e.g., **Fig. S39a**), multiple constant potential steps were applied from 0 to 1.0 V vs. Hg/HgO, each lasting 180 s. LSV scans (e.g., **Fig. S39b**) were recorded from -0.1 to 1.5 V vs. Hg/HgO at a scan rate of 1 mV·s⁻¹ with a step size of 0.2 mV. Electrode

discharge experiments (e.g., **Fig. 3a**) consisted of two segments: an initial CA step at 0.62 V (0.72 V for NiFe hydroxide) vs. Hg/HgO for 120 s, followed by a reverse current step via CP at 0 mA·cm⁻² (OCP), -0.05 mA·cm⁻², or -0.25 mA·cm⁻² for ~1800s (some experiments were stopped earlier if complete reduction was achieved). For variable operation experiments (e.g., **Fig. S46**), a single stability cycling loop included a 3-min CA step at 0.86 V (0.77 for NiCo, 0.72 for NiFe hydroxide) vs. Hg/HgO, followed by a 4-min reverse potential step at either OCP or -1.2 V vs. Hg/HgO. The loop was repeated for six cycles.

Note: Except for LSV scans, 100% iR compensation for constant current and potential steps was carried out manually using the R_u value from the initial EIS measurement and calculated using **Eq. 3**. Electrochemical measurements during variable operation were conducted under potentiostatic control to achieve a consistent cathodic potential during the reverse step, with the potential adjusted to maintain a current density close to 0.5 mA·cm⁻².

S7. Chemical composition analysis via ToF-SIMS

Depth profiles and high-resolution elemental maps were acquired using an IONTOF GmbH TOF-SIMS M6 instrument under ultrahigh vacuum ($\sim 10^{-9}$ Torr). For depth profiling in negative polarity, a Cs⁺ beam (40 nA, 0.5 kV) was used to sputter an area of $300 \times 300 \mu\text{m}^2$, followed by raster-scanning a $100 \times 100 \mu\text{m}^2$ area within the sputtered crater using a Bi⁺ analysis beam (4 pA, 30 keV). High-resolution imaging was performed in fast-imaging mode, achieving a lateral resolution of 200 nm with a current of 0.4 nA. TOF-SIMS analysis was conducted *ex situ*, before and after accelerated catalyst degradation tests in a three-electrode cell under variable operation (**Figs. S30 and S32**). Post-analysis films were rinsed with DI water and dried in a vacuum oven before measurement.

NCP was utilized to estimate the average sputtering rate of the catalytic films during TOF-SIMS analysis in negative polarity. The detailed calculation of the sputtering rate and depth estimation via NCP is covered in our previous work.⁹ The mean depth of the NiCo(OH)₂/TF electrode was 315.7 ± 44.7 nm, based on an average of 100 line scans in both the x and y directions. Given a sputtering time of 7385 seconds for this sample, the resulting sputtering rate was $0.043 \pm 0.01 \text{ nm}\cdot\text{s}^{-1}$. This sputtering rate was used to estimate depths in **Figs. 4 and S61**, as all films had similar thicknesses and metal hydroxide/oxyhydroxide compositions, leading to comparable densities.

A statistical depth profile analysis was performed to estimate the depth distribution ranges of secondary ion fragments shown in **Fig. 4**. ToF-SIMS secondary-ion yield plots were integrated to determine the depth range encompassing 68.27% of the total secondary-ion

yield, corresponding to one standard deviation from the mean ($\mu \pm 1\sigma$). The depth distribution range was determined by identifying the sputtering times at which the dashed lines at 68.27% of the total yield intersected the depth profile. These times were then converted to depth units (nm) using the previously determined sputtering rate of 0.043 ± 0.01 nm·s⁻¹. The resulting values are shown in **Fig. 4** as the start and end points of the colored bars, indicating that 68% of the secondary-ion fragment's total concentration falls within the range covered by the bar. **Figs. S51** and **S52** show secondary-ion yield profiles normalized to the maximum signal, with dashed lines marking the 68.27% confidence interval. **Figs. S54** and **S55** display the corresponding integrated yields within that interval. Supporting notes provide further details on the procedures used for each plot. A more detailed explanation of this method is available in our previous work.⁹

S8. In-plane conductivity measurements using IDA electrodes

Film preparation and characterization

NiCo(OH)₂ films were deposited on gold interdigitated array (IDA) electrodes for use as working electrodes. First, the IDA electrodes were cleaned in 3 M HCl for 10 min, rinsed with DI water, and allowed to dry. Films were electrodeposited in a two-electrode configuration from 100 mM metal(II) nitrate aqueous solutions, with the plating bath pH adjusted to ~3 using 1 M nitric acid. A pre-cleaned 50 mL glass cell was filled with ~15 mL of the plating bath and purged with N₂ gas for 5 min. A Ni foam counter electrode (geometric area: 2 × 2 cm²) was positioned 1 cm from the working electrode, and a fresh Ni foam counter electrode was used for each deposition of the same film type to prevent cross-contamination. The IDA electrode was secured to a Ti clip holder, ensuring electrical contact with both electrode terminals.

After an initial OCP measurement for 5 min, films were deposited galvanostatically at $-1 \text{ mA}\cdot\text{cm}^{-2}$ for 90 – 600 s (total charge: 90 – 600 mC·cm⁻²) without stirring. Depositions were performed in 30 s intervals, separated by 10 s resting periods to minimize concentration gradients. After deposition, films were rinsed with DI water and stored in a vacuum oven until further use. NiCo(OH)₂ films with varying Co content were obtained by adjusting the Ni:Co ratio in the plating bath while keeping the total metal concentration constant at 100 mM.

Importantly, increasing the Co content while maintaining a constant deposition time resulted in thicker films being more prone to peeling. We attribute this effect to Co's higher

conductivity,²⁴ which enhances deposition efficiency. In contrast, Ni(OH)₂ (0% Co) behaves as an insulator, leading to charge-trapping effects that limit electron transport and reduce deposition efficiency, requiring longer times to achieve a given thickness. As Co content increases, improved electron conductivity facilitates deposition; however, excessive growth leads to structural instability, making the film susceptible to detachment if the deposition time is too long. To address this, we optimized deposition times to ensure consistent film thicknesses and prevent peeling. Film thickness for each composition was measured via NCP and incorporated into effective conductivity calculations. The metal ratio in bimetallic films was determined using ICP-MS. A summary of the film properties at increasing Co contents is provided in **Table S2**.

Table S2. Properties of NiCo films deposited on IDA electrodes.

Co concentration in the plating bath (mM)	Co content from ICP-MS (mol%)	Deposition time (s)	Film thickness from NCP (μm)
0	0	600	5.009 ± 0.117
0.5	0.9 ± 0.1	600	4.865 ± 0.158
1.0	3.2 ± 0	600	5.011 ± 0.726
2.5	10.3 ± 0.8	300	2.596 ± 0.554
5.0	13.1 ± 1.5	240	0.999 ± 0.167
10.0	28.4 ± 0.4	240	1.515 ± 0.090
15.0	36.8 ± 0.9	240	2.075 ± 0.020
25.0	48.8 ± 0.4	180	1.276 ± 0.074
100.0	100.0	90	0.779 ± 0.085

Uncertainties represent the standard deviation from three different films.

After testing, the electrodes were dried, and the catalyst film thicknesses were measured. The surface characteristics of the films were analyzed using a Keyence VK-X1100 Optical profilometer. Surface roughness and film thickness were estimated from 3D surface profiles obtained with a 404 nm laser and a 50 \times objective lens. The Ni:Co ratio in films deposited on IDA electrodes was determined by dissolving the films in 3 M nitric acid and analyzing the resulting solution via solution-mode ICP-MS.

In-plane conductivity measurements

Electrochemical measurements were performed in a three-electrode electrochemical cell (**Fig. S57a**) using a Hg/HgO reference electrode and a graphite rod counter electrode. The cell was filled with unpurified 1 M KOH (~25 mL), and a bipotentiostat was used for data acquisition. A custom IDA electrode adapter was designed to connect one terminal of the IDA electrode to the green working electrode clip (WE₁) and the other to the yellow working electrode clip (WE₂). After assembly, the OCP was monitored for 120 s or until a stable response was achieved. Then, a series of constant potential steps from -0.02 to 0.64 V vs. Hg/HgO were applied, each lasting 180 s, with 20 mV increments. Potential stepping was performed with a 10 mV offset between WE₁ and WE₂ (i.e., WE₁ = WE₂ - 10 mV). A sample interval of 1 s was used, and the sensitivity (A/V) was increased from 1E-6 to 1E-4 as the current increased with potential stepping. A detailed description of this measurement and the corresponding plots is available elsewhere.⁵ Following the multistep CA run, LSV and CV scans were recorded from -0.1 to 0.64 V vs. Hg/HgO at a scan rate of 5 mV·s⁻¹ with a step size of 1 mV.

In-plane effective conductivity calculation

As shown in **Fig. S57b**, the catalytic film bridged two adjacent lines of the IDA array. The IDA electrode consisted of 544 lines (line width: 6.4 μm , gap spacing: 4 μm , line length: 6.6 mm). The effective in-plane conductivity, σ_{eff} , was calculated using **Eq. 4**:⁵

$$\sigma_{\text{eff}} = \frac{i_{\text{cond}} \cdot w}{N \cdot l \cdot \delta \cdot \Delta V} \quad (4)$$

where w is the IDA gap spacing (4 μm), N is the number of electrodes (544), l is the line length (6.6 mm), δ is the film thickness (from **Table S2**), ΔV is the potential offset between WE₁ and WE₂ (0.01 V), and i_{cond} is the in-plane conductivity current:

$$i_{\text{cond}} = \frac{i_{\text{WE},1} - i_{\text{WE},2}}{2} \quad (5)$$

Using **Eq. 4**, an effective conductivity value (in $\text{S}\cdot\text{cm}^{-1}$) was obtained for each potential step.

S9. Metal dissolution analysis via ICP-MS

Electrochemical flow cell setup

On-line ICP-MS experiments were conducted using an in-house electrochemical flow cell (**Fig. S59**) described in a previous work.²⁵ An Ag/AgCl reference electrode was integrated directly into the cell without a PTFE Luggin capillary, utilizing a dedicated port in the cell design. A Pt wire counter electrode was placed downstream of the cell. Ni(OH)₂, NiCo(OH)₂, and NiFe(OH)₂ films deposited on Ti foil substrates served as the working electrodes (exposed area defined by the gasket: 0.1967 cm²) and were positioned at the top of the cell. A piece of copper tape was attached to the back of the Ti foil substrate to establish electrical contact with the alligator clip. All experiments were conducted in unpurified 0.1 M KOH, degassed with high-purity O₂ gas. The KOH electrolyte was circulated from a plastic reservoir into the flow cell at a flow rate of 2 mL·min⁻¹ using a peristaltic pump (Ismatec Reglo ICC). Tubing lines (ThermoFisher Scientific, PTFE 1/16 in OD) and pump tubes (Ismatec, 2.79 mm ID Viton) were pre-rinsed in nitric acid to prevent electrolyte contamination.

ICP-MS measurements

Solution-mode ICP-MS was used to measure metal concentrations in unpurified 0.1 M KOH electrolyte. Measurements were performed on an iCAP RQ ICP-MS (Thermo Scientific) equipped with a single quadrupole mass analyzer. The spectrometer was configured to detect ⁶⁰Ni, ⁴⁸Ti, ⁵⁷Fe, and ⁵⁹Co isotopes. A collision/reaction cell was operated in kinetic energy discrimination (KED) mode to minimize the presence of polyatomic interferences (e.g., ⁴⁰Ar¹⁸OH for ⁵⁹Co, ³⁰Si¹⁷OH for ⁴⁸Ti, ⁴⁰Ar¹⁶OH for ⁵⁷Fe), with a He collision gas flow rate of

$5 \text{ mL}\cdot\text{min}^{-1}$. A parallel flow nebulizer (Burgener Research PEEK Mira Mist) was used with a gas flow rate of $1.08 \text{ L}\cdot\text{min}^{-1}$ and Pt sample and skimmer cones (Thermo Scientific). A 3.5 mm high-matrix insert was used. Plasma power was set to 1548 W, and the quartz cyclonic spray chamber temperature was maintained at 2.55°C . Calibration curves for the target isotopes were prepared from reference standards in semiconductor-grade KOH (0.1 M) at concentrations ranging from 2.5 to 500 ppb. Ni, Co, Fe, and Ti standards (Sigma-Aldrich, metal concentration: $1000 \text{ mg}\cdot\text{L}^{-1}$, ICP-MS standard in 2% w/w nitric acid) were prepared in unpurified 0.1 M KOH and fed through the electrochemical cell at $2 \text{ mL}\cdot\text{min}^{-1}$ each experimental day. A detailed explanation of ICP-MS method optimization is available elsewhere.^{1,26}

Electrochemical measurements

After assembly, the OCP was monitored for 120 s or until a stable response was achieved. The electrode was then conditioned via CP for 300 s at $0.5 \text{ mA}\cdot\text{cm}^{-2}$. A potentiostatic EIS measurement was carried out to determine the R_u value. An initial LSV scan was recorded from 0.25 to 0.6 V vs. Ag/AgCl at a scan rate of $5 \text{ mV}\cdot\text{s}^{-1}$ with a step size of 0.5 mV. For variable operation experiments (e.g., Fig. 5), a single stability cycling loop included a 3-min CP step at $1.35 \text{ mA}\cdot\text{cm}^{-2}$, followed by a 3-min reverse current step at $-1.35 \text{ mA}\cdot\text{cm}^{-2}$. The loop was repeated for five cycles. **Note:** 85% iR compensation for CP steps was carried out manually using the R_u value from the initial EIS measurement and calculated using Eq. 3.

ICP-MS data analysis

The distance between the flow cell outlet and ICP-MS inlet was optimized to minimize signal broadening, reducing the response delay to 2 s, which was accounted for when plotting electrochemical response alongside metal concentrations. Isotope intensities were converted into concentration ($\text{ng}\cdot\text{L}^{-1}$) using the slope and intercept from calibration curves. Concentrations were normalized by the projected geometric area in **Figs. 5, S61, and S62**. To convert the concentration of the dissolved metal into the electrolyte (c_{diss} , $\mu\text{g}\cdot\text{L}^{-1}$) into dissolution rates (r_{diss} , $\text{ng}\cdot\text{s}^{-1}$), **Eq. 6** was used:

$$r_{\text{diss}} = c_{\text{diss}} \cdot q \cdot \frac{1}{60} \quad (6)$$

where q is the flow rate (in $\text{mL}\cdot\text{min}^{-1}$), and 1/60 is a conversion factor to express the rate in seconds.

S10. Accelerated catalyst degradation tests in a zero-gap electrolyzer

Electrode preparation

Ni gauze was used as the Ni mesh electrodes for variable operation tests in the zero-gap alkaline water electrolyzer. Nickel gauze pieces ($20 \times 65 \times 0.1$ mm) were cut and cleaned following the procedure outlined in the general electrode preparation section. Two pieces were assembled into the electrolyzer, serving as the O₂ and H₂ electrodes.

Fe-doped Ni mesh anodes were prepared by conditioning a Ni gauze strip in a KOH electrolyte containing a known concentration of Fe. A three-electrode PTFE cell (**Fig. S1**) was used, with a Hg/HgO reference electrode, a graphite rod counter electrode, and the Ni gauze strip as the working electrode. The electrolyte consisted of purified KOH spiked with Fe³⁺ to reach a concentration of 1 mM (~ 55.85 mg Fe·L⁻¹). The Ni gauze strip was immersed so that 35 mm was wetted by the electrolyte, yielding a projected geometric area of 7 cm² (**Fig. S80b**). The working electrode was conditioned using CV cycling through a sequence built in the Gamry Sequence Wizard. CV conditioning was performed from 0.2 to 0.56 V vs. Hg/HgO at a scan rate of 10 mV·s⁻¹ and a step size of 1 mV. A total of 1000 cycles were conducted in 20 intervals of 50 cycles, allowing Fe incorporation into the porous Ni oxyhydroxide film formed during cycling. Potentiostatic EIS measurements (DC potential: 0 V, frequency range: 200 to 0.1 kHz, AC voltage: 5 mV, drift correction enabled) and intermediate CV scans (0.2 to 0.56 V vs. Hg/HgO, 5 mV·s⁻¹ scan rate, 1 mV step size) were performed every 50 cycles to monitor the experiment (**Fig. S80a**). After conditioning, the Fe-doped Ni mesh anode was rinsed with DI water, dried, and stored for further use.

Zero-gap water electrolyzer experimental setup

We used the zero-gap alkaline water electrolyzer reported in our previous study,¹⁰ incorporating a few updates to the cell design and flow system. A new acrylic endplate with a dedicated port for the Hg/HgO reference electrode was fabricated using computer numerical control (CNC) machining (**Fig. S63a**). Note: The working electrode (WE) was always positioned on this endplate to enable electrode potential measurement, with the Hg/HgO reference electrode tip placed 1 mm from the Ni mesh electrode serving as the WE. The 3D model of this endplate is freely available on [GitHub](#). The cell was assembled as outlined in our protocol,¹⁰ placing the separator between two gaskets (thickness: 0.4 mm) with Ni mesh electrodes on each side (**Fig. S63b**). The endplates featured an integrated PDMS gasket to ensure a secure seal.

Once assembled, the electrolyzer was integrated into the flow system (**Fig. S63c, d**). Two 250 mL PTFE vessels served as electrolyte reservoirs, with modified caps fitted with barbed connectors (3/16 inch) for tubing connections. The system used high-temperature silicone tubing (Fuel Cell Store, 4 mm ID × 6 mm OD) and peristaltic pumps (KAMOER) equipped with Norprene chemical tubing (3.2 mm ID × 6.4 mm OD) to circulate electrolyte at a flow rate of 200 mL·min⁻¹. A digital thermostatic water bath (JOANLAB, 6 L) maintained electrolyte temperature, with stainless-steel thermocouples ensuring accurate monitoring. The silicone tubing was carefully connected to the electrolyzer's barbed fittings following the flow scheme in **Fig. S63d**.

Following our previous guidelines,¹ fresh 7 M KOH electrolytes were prepared using polypropylene volumetric flasks. To align with industrial conditions, unpurified KOH

electrolyte was used. To maintain a constant Fe concentration, the 7 M KOH batch was spiked with iron nitrate to reach nominally 500 ppb Fe (**Table S1**), as recommended previously.^{11,12} The electrolytes were degassed with high-purity O₂ (anolyte reservoir) and H₂ (catholyte reservoir) during initial OCP measurements using a plastic bubbler. The electrolytes were circulated through the system and into the electrolyzer to remove any trapped air within the porous foam electrodes until the system reached the targeted flow rate and temperature.

The separator was prepared following our previous protocol.¹⁰ Discs (34 mm diameter) were precisely cut from an A4 sheet using a precision blade on a plastic cutting board. Before use, separators were conditioned in 7 M KOH electrolyte for at least 12 hours in an airtight plastic container.

Potentiostat configuration

Electrochemical tests were conducted with two potentiostats operating simultaneously (**Fig. S63d**). The main potentiostat (P1) was connected in a three-electrode cell setup, where the Ni mesh electrode under study (O₂ or H₂ electrodes) acted as the WE, the other Ni mesh electrode as the counter electrode (CE), and the reference electrode (RE) alligator clip was connected to the Hg/HgO reference electrode placed on the endplate with a dedicated RE port. The second potentiostat was connected in a two-electrode cell setup and was used only to monitor the total cell potential using an OCP measurement. The CE and RE alligator clips were connected to the electrode used as the CE, while the WE alligator clips were connected to the electrode tested as WE for that experiment (see **Fig. S63c**).

Estimation of the reverse current for variable operation tests

The cell was assembled to estimate the ionic resistance through the electrolyzer manifold, as shown in **Fig. S64**, with a 7.6 cm-long silicone tube connecting the anodic and cathodic endplates. The Ni mesh electrodes were assembled as usual, while the separator was replaced with a 1 mm-thick circular plastic sheet to block the internal ionic pathway, forcing ion flow exclusively through the manifold. The electrolyte was circulated at 50 °C with a flow rate of 200 mL·min⁻¹. Ionic resistance was measured using potentiostatic EIS (DC potential: OCP, frequency range: 200 to 0.1 kHz, ten points per decade, AC voltage: 5 mV, drift correction enabled) with potentiostat P1 and a multimeter. The high-frequency resistance (HFR) was nominally 11.2 ± 3.2 kΩ. The ion conduction current i_{ion} , associated with the ion conduction resistance, R_{ion} , through the manifold was estimated using Ohm's law:

$$i_{\text{ion}} = \frac{E_{\text{cell}}}{R_{\text{ion}}} \quad (7)$$

where E_{cell} represents the total cell potential. Considering a total cell potential of ~2 V during the constant current step in variable operation tests (e.g., **Fig. S68a**) and using the lower limit of the ion conduction resistance (8 kΩ), the estimated ion conduction current flowing to overcome this resistance is ~0.25 mA when applying **Eq. 7**. This value was used as the reverse current in the variable operation tests.

Note: This approach provides an approximate estimation of the reverse current in our variable operation tests. Significant variations in ionic resistance were observed, attributed to gas bubbles in the manifold, fluctuations in flow rate, and temperature gradients, all of

which influence the magnitude of shunt currents.^{27,28} We strongly recommend that researchers assess this factor carefully for their specific cell architecture, as this value should not be extrapolated to other systems without prior verification. Additionally, alternative methods for simulating reverse currents should be explored.

Extended variable operation experiments

Tests were conducted using an automated sequence in the Gamry Sequence Wizard, structured into three main sections: initial assessment, stability cycling loop, and final assessment:

Initial assessment: First, the OCP was monitored for 2 hours or until a stable response was achieved. The electrolyte reservoirs were degassed, allowing the system to reach the target temperature. Next, the electrolyzer was conditioned using a steady current of 60 mA (corresponding to a current density of 15 mA·cm⁻² based on a 4 cm²_{geo} geometric electrode area) for 24 h, closely monitoring the cell voltage until stabilization. This step ensured the formation of the active electrocatalytic phase and consistent operating conditions.

Galvanostatic EIS was used to measure the high-frequency resistance (HFR), which accounts for the ion conduction resistance, R_{ion} , from the electrolyte and separator, and the electronic resistance, R_{el} , from the electrocatalytic film and the contact resistances between the electrode, current collector, and electrolyzer terminals:²⁹

$$\text{HFR} = R_{\text{ion}} + R_{\text{el}} \quad (8)$$

Galvanostatic EIS was conducted at 15 mA·cm⁻², with an AC amplitude of 5 mA over a frequency range of 100 kHz to 1 Hz, with drift correction enabled. The HFR was obtained from the high-frequency intercept of the Nyquist plot with the real axis.³⁰ HFR values ranged typically between 10 and 20 mΩ·cm² at 50 °C in 7 M KOH (e.g., **Fig. S65c**). Next, full Nyquist plots were recorded using galvanostatic EIS at the preconditioning current density of 15 mA·cm⁻² (frequency range: 100 kHz to 0.5 Hz, AC amplitude: 5 mA, drift correction enabled).³¹ This measurement was repeated three times for reliability.

Next, multistep CP runs were used to construct full-cell polarization curves. Each constant current step lasted 600 s, followed by galvanostatic EIS at the same current (100 kHz to 0.5 Hz, AC amplitude: 5 mA). The initial current step was set at 4 mA, after which we used the Gamry Sequence Wizard to systematically increment the current using sequence loops. The first loop comprised steps from 8 to 32 mA in 8 mA increments, while the subsequent loop ranged from 40 to 600 mA in 40 mA increments. An example of this procedure is available in our protocol.¹⁰ Average cell voltages were derived from the final 60 s of each step to construct the polarization curves. The HFR measured at each step was used to calculate the *iR*-corrected potential, $E_{iR\text{-free}}$, for each corresponding cell voltage, E_{cell} , based on **Eq. 9:**³⁰

$$E_{iR\text{-free}} = E_{\text{cell}} - i \cdot \text{HFR} \quad (9)$$

where i is the current applied at each step. Examples of polarization curves and corresponding HFR values are shown in **Figs. S65-S67 and S81-S82**.

Tafel slopes were obtained from the *iR*-free polarization curves to evaluate the kinetics of water splitting. The Tafel slope was determined by plotting the *iR*-free cell potential in the y-axis against the logarithm of the current density (*j*) in the x axis:^{32,33}

$$E_{iR\text{-free}} = b \log j + C \quad (10)$$

where *b* is the Tafel slope (V·dec⁻¹), and *C* is the y-axis intercept. Linear fitting was conducted in the low-current-density region below 30 mA·cm⁻². In contrast to our previous work,¹⁰ in which the two-electrode cell setup prevented distinguishing the contribution of each reaction to the Tafel slope, our endplate with a RE port allows us to measure the electrode potential for the O₂ and H₂ electrodes separately. Thus, Tafel slopes shown in **Fig. S65e** represent the combined HER and OER contributions, while **Fig. S66f** shows the anode (O₂ electrode) Tafel slope, and **Fig. S67f** shows the cathode (H₂ electrode) Tafel slope.

Stability cycling loop: The variable operation test simulates electrode behavior during a shutdown by incorporating a reverse current step between constant current steps. A single stability cycling loop consisted of two CP steps: a 10-min step at 480 mA (corresponding to a current density of 120 mA·cm⁻²), followed by a 5-min reverse current step at -1 mA (corresponding to a current density of -0.25 mA·cm⁻²). A galvanostatic EIS measurement immediately followed the reverse step at 15 mA·cm⁻² (frequency range: 100 kHz to 0.5 Hz, AC amplitude: 5 mA, drift correction enabled). The electrolyzer underwent this test for 240 cycles (i.e., 60 h of uninterrupted operation plus the time required for EIS).

Final assessment: The same experimental routine carried out during the initial assessment was repeated: (1) galvanostatic EIS to measure the HFR, (2) full Nyquist plot using

galvanostatic EIS, and (3) multistep CP divided in two current loops (from 8 to 32 mA and 40 to 600 mA) to construct polarization curves, followed by galvanostatic EIS at each current step. Polarization curves and Nyquist plots from the initial and final assessments were used to compare the electrolyzer performance before and after variable operation tests.

For the high current density experiments, we applied the same stability cycling loop, with the only change being a 10-minute step at 4 A ($1 \text{ A} \cdot \text{cm}^{-2}$), followed by a 5-minute reverse current step at -200 mA ($-50 \text{ mA} \cdot \text{cm}^{-2}$, 5% of the forward load). A power supply (Matsusada R4K-80) was used in a two-electrode setup. Galvanostatic EIS ($15 \text{ mA} \cdot \text{cm}^{-2}$) was performed separately with the Gamry Reference 620 potentiostat immediately after the reverse step. Electrode potentials were monitored using two Gamry potentiostats with Hg/HgO reference electrodes on each side of the zero-gap electrolyzer.

Ex situ X-ray photoelectron spectroscopy analysis

XPS analyses were carried out with a PHI VersaProbe 4 instrument using a nonmonochromatic Mg Ka source (1253.6 eV). Using a Mg source over a traditional Al source is critical to prevent the overlap between Ni LMM Auger features and Fe 2p peaks, which would otherwise make Fe detection more challenging.² The base pressure of the instrument was $\sim 10^{-9}$ Torr. High-resolution spectra were collected over an analysis area of $\sim 250 \times 250 \mu\text{m}^2$ using a pass energy of 10 eV. The charge neutralizer was not employed to prevent partial reduction of the NiOOH phase. Binding energy calibration was carried out using the C 1s peak for adventitious hydrocarbons at 284.8 eV. Data analysis was performed using CasaXPS software. The spectral fitting parameters for the O 1s and Ni 2p peaks were

adopted from previous studies.³⁴⁻³⁶ Fitting components were modeled using a combination of Gaussian (70%) and Lorentzian (30%) profiles, denoted as GL(30) in CasaXPS. A standard Shirley-type baseline was employed to fit the spectra of transition metal peaks. This baseline featured variable offset levels at the high binding energy endpoint.

We adhered to post-operation disassembly guidelines as recommended,³⁷ disassembling cells inside a watertight container filled with DI water to maintain separator hydration. After unscrewing the stainless steel bolts, the components were carefully removed from the assembly. The electrodes were precisely cut and dried for post-mortem XPS analysis, following the ex situ XPS analysis protocol detailed in our previous work.⁹ Drying was conducted through repeated cycling between atmospheric pressure and low vacuum (>50 Torr) using a sorption pump to minimize contamination and limit surface exposure to air post-testing.

Ex situ ICP-MS measurements

Solution-mode ICP-MS was used to measure metal concentrations in KOH electrolytes during variable operation tests. Electrolyte samples (250 µL each) were collected from the reservoirs at specified intervals. A 10× dilution routine was applied, followed by matrix neutralization with 2 wt.% nitric acid, as outlined in our previous work.¹ This step was critical for enhancing instrument stability and optimizing plasma performance, given the high total dissolved solids in the KOH matrix. This approach ensured that detection limits remained in the low ppb range for all analytes. Measurements were conducted in an Agilent 7500ce ICP-MS equipped with a quadrupole mass analyzer and a collision/reaction cell. The complete

analytical procedure, experimental setup, quality control routines, and results from two previous analytical projects are detailed on this [website](#).

Supporting Figures, Tables, and Schemes

Simulated shutdown tests to study electrode discharge

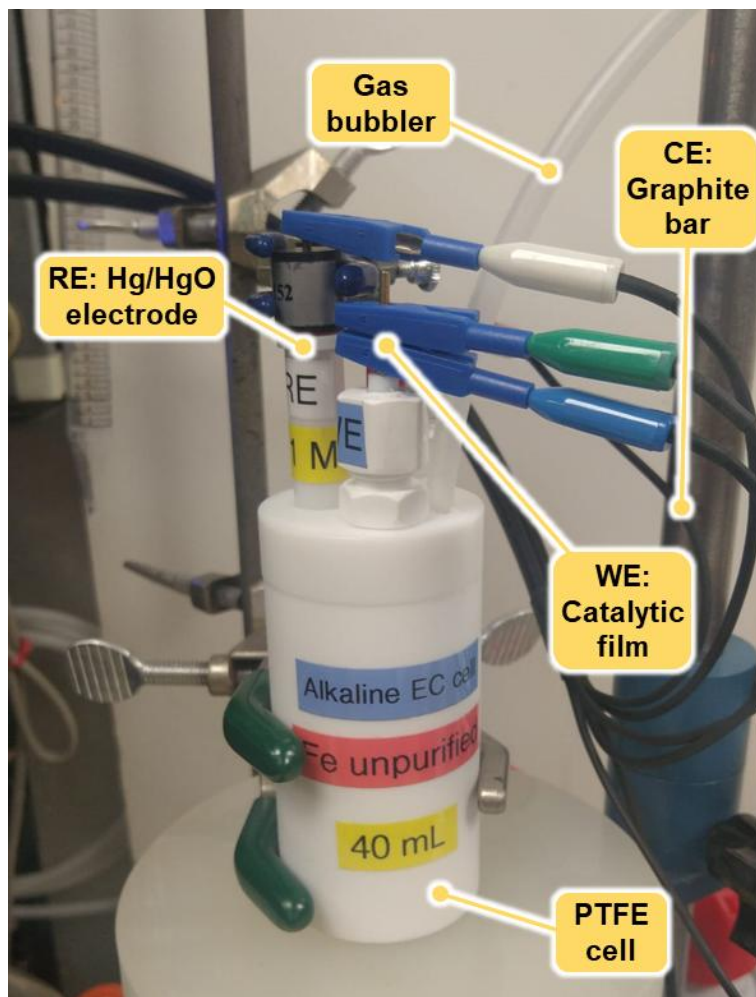


Figure S1. Three-electrode PTFE cell used to test simulated shutdowns and reverse currents in unpurified KOH electrolyte. The working electrode (WE) consisted of transition metal hydroxide films deposited on Ti foil substrates with a 1 cm^2 exposed area. The counter electrode (CE) was a graphite rod, while the reference electrode (RE) was an Hg/HgO electrode with a filling solution of 0.1 M, 1 M, or 7 M KOH, depending on the experiment's electrolyte concentration. The cell design ensures a fixed electrode spacing (nominally 2 cm) in all experiments.

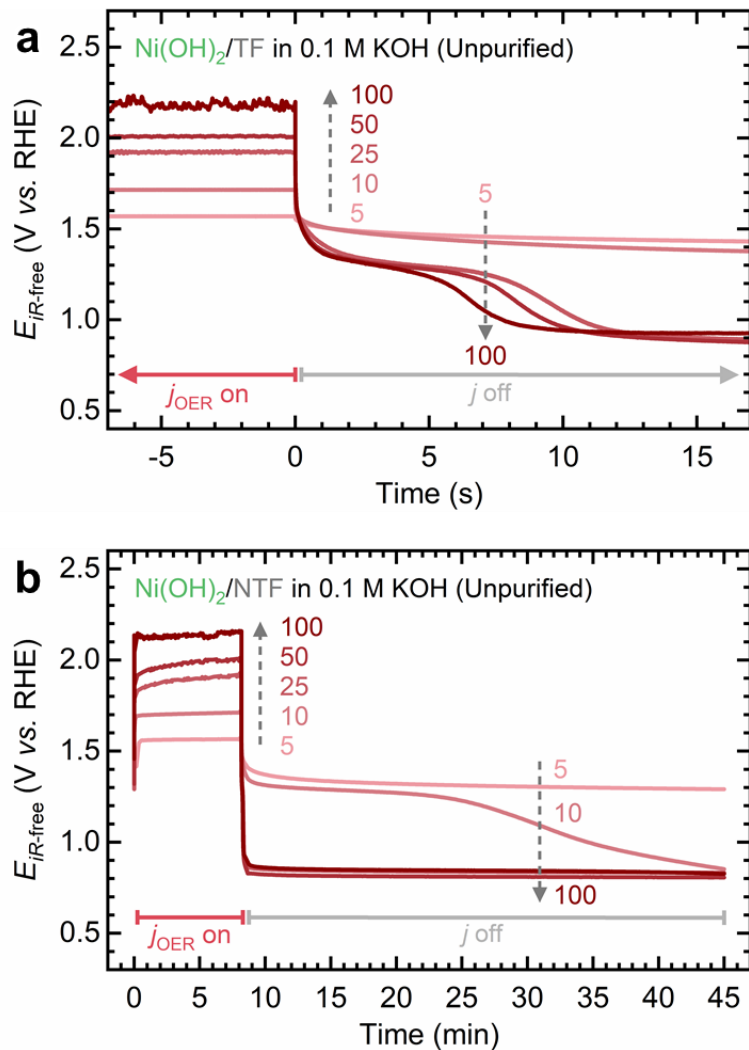


Figure S2. Open circuit potential decay transients for $\text{Ni(OH}_2\text{)/TF}$ electrodes following galvanostatic polarization at increasing anodic current densities. Profiles are presented on (a) short and (b) long timescales. Dashed arrows indicate the increase in anodic current density (5 to 100 $\text{mA}\cdot\text{cm}^{-2}$). Experiments were conducted in unpurified 0.1 M KOH electrolyte at 20 °C.

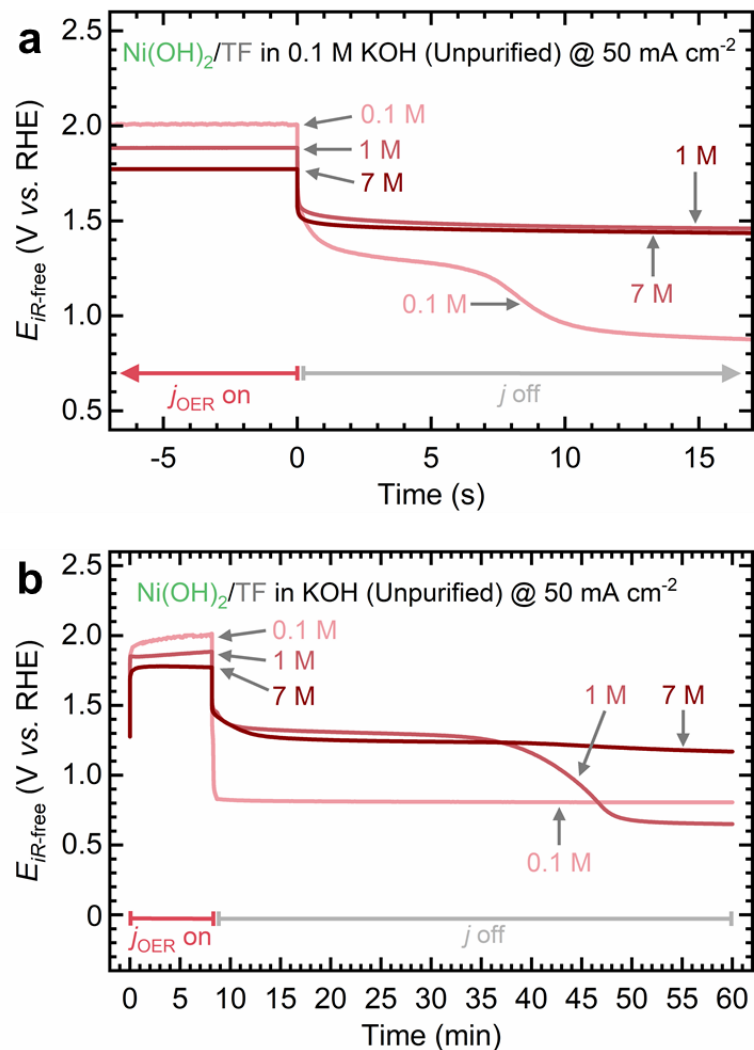


Figure S3. Open circuit potential decay transients for $\text{Ni(OH}_2\text{)/TF}$ electrodes following galvanostatic polarization at an anodic current density of $50 \text{ mA}\cdot\text{cm}^{-2}$. Experiments were conducted at increasing concentrations of unpurified KOH electrolyte at 20°C . Profiles are presented on (a) short and (b) long timescales.

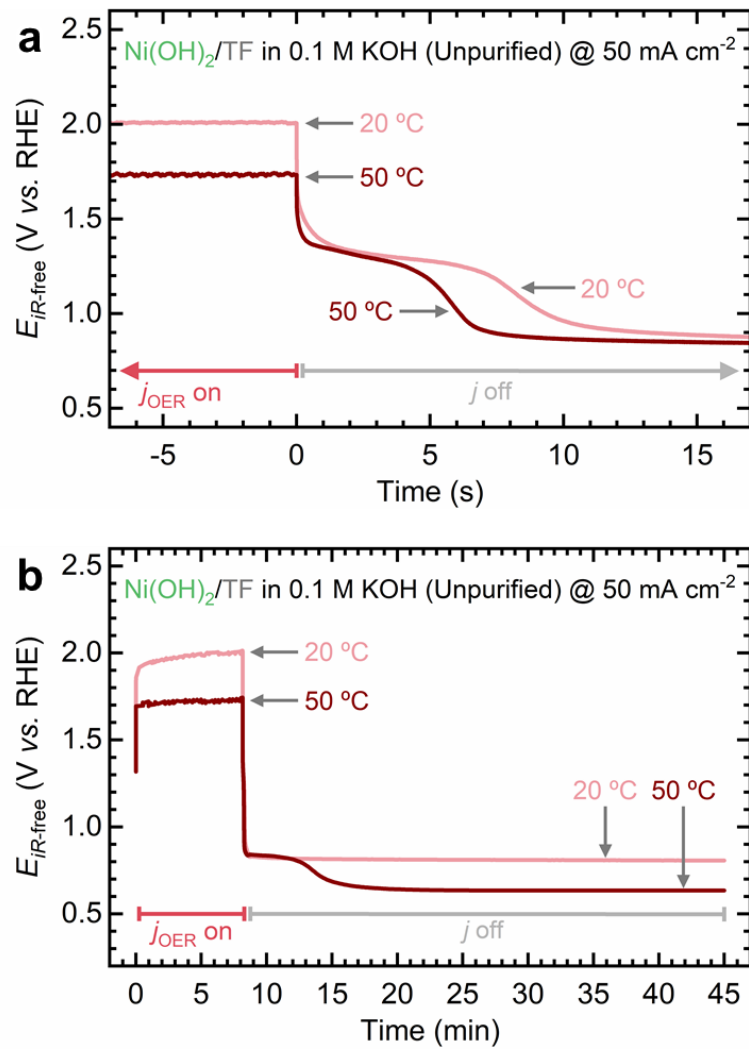


Figure S4. Open circuit potential decay transients for $\text{Ni(OH)}_2/\text{TF}$ electrodes following galvanostatic polarization at an anodic current density of $50 \text{ mA}\cdot\text{cm}^{-2}$. Experiments were conducted at two temperatures: 20 and 50°C . Profiles are presented on (a) short and (b) long timescales. Experiments were conducted in unpurified 0.1 M KOH electrolyte.

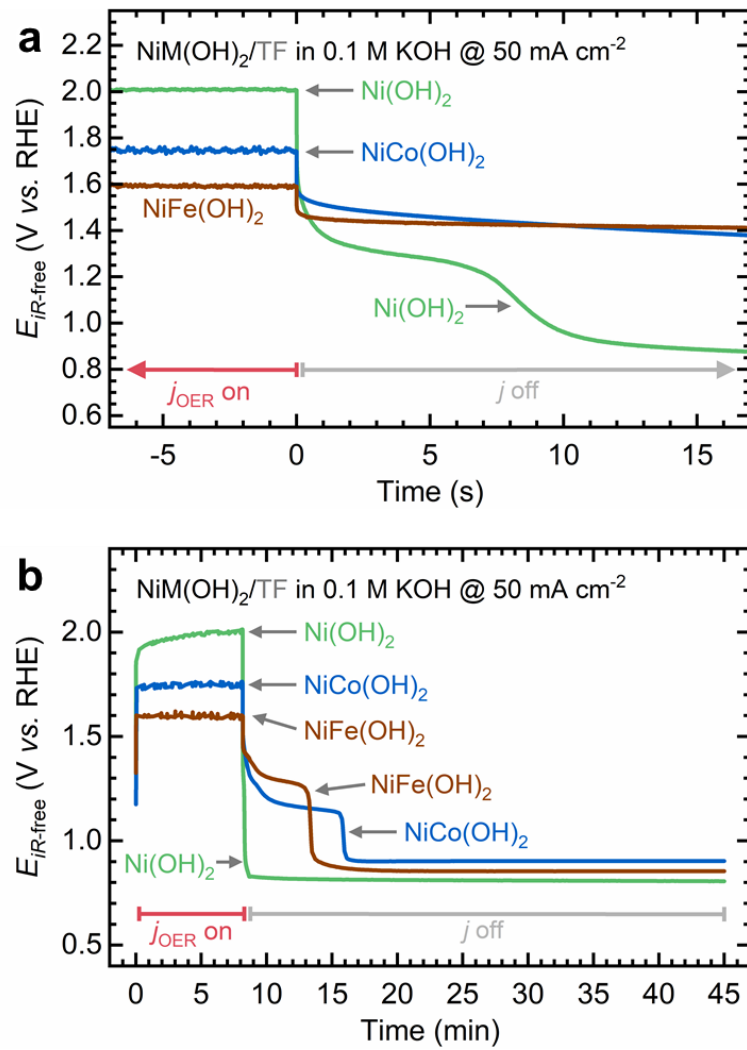


Figure S5. Open circuit potential decay transients for Ni(OH)₂/TF, NiCo(OH)₂/TF, and NiFe(OH)₂/TF electrodes following galvanostatic polarization at an anodic current density of 50 mA·cm⁻². Profiles are presented on (a) short and (b) long timescales. Experiments were conducted in unpurified 0.1 M KOH electrolyte at 20 °C.

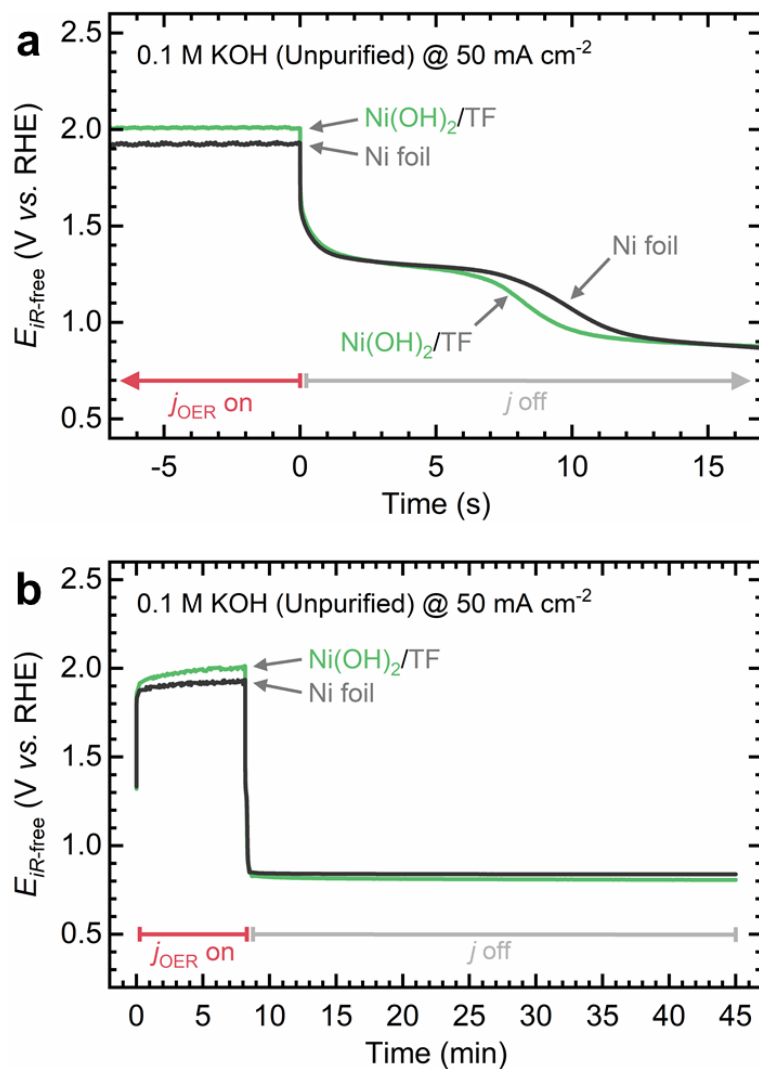


Figure S6. Open circuit potential decay transients for Ni(OH)₂/TF and Ni foil electrodes following galvanostatic polarization at an anodic current density of 50 mA·cm⁻². Profiles are presented on (a) short and (b) long timescales. Experiments were conducted in unpurified 0.1 M KOH electrolyte at 20 °C.

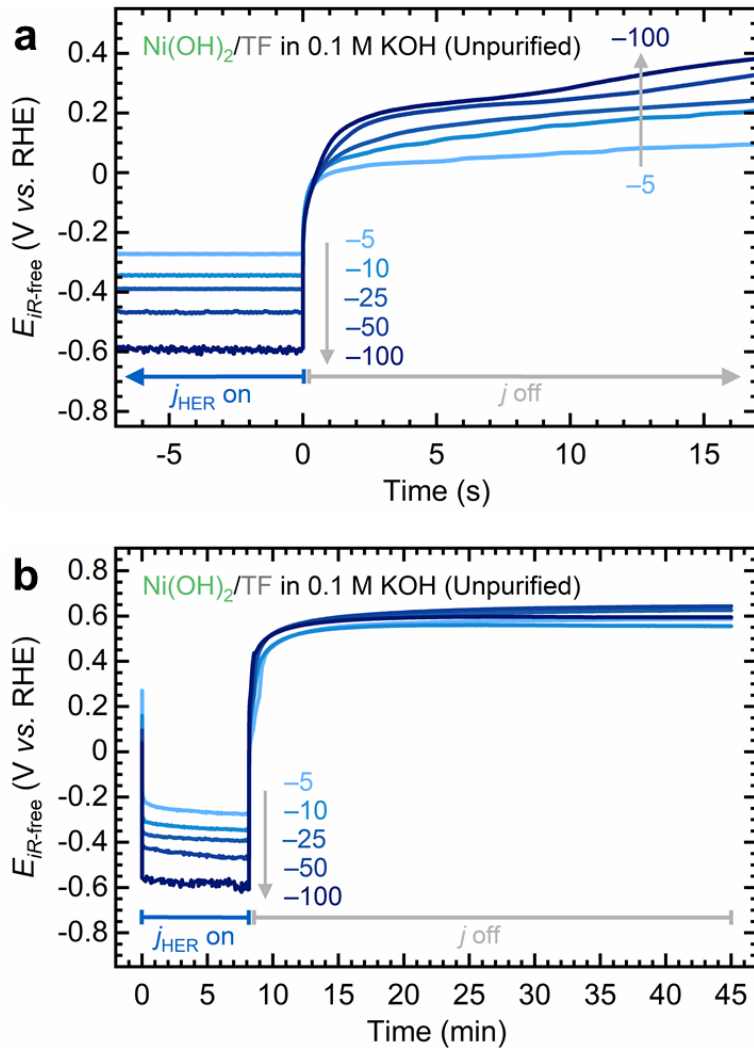


Figure S7. Open circuit potential decay transients for Ni(OH)₂/TF electrodes following galvanostatic polarization at increasing cathodic current densities. Profiles are presented on (a) short and (b) long timescales. Dashed arrows indicate the increase in cathodic current density (-5 to -100 mA·cm⁻²). Experiments were conducted in unpurified 0.1 M KOH electrolyte at 20 °C.

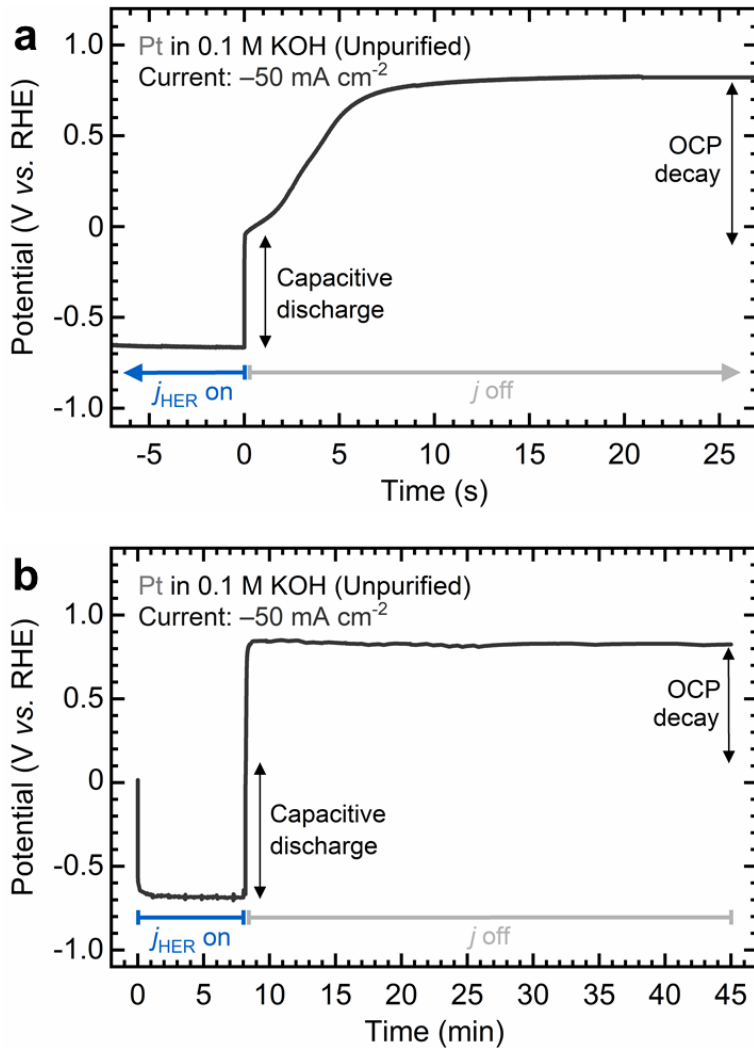


Figure S8. Open circuit potential decay transient for a Pt electrode following galvanostatic polarization at a cathodic current density of $-50 \text{ mA}\cdot\text{cm}^{-2}$. Profiles are presented on (a) short and (b) long timescales. The experiment was conducted in unpurified 0.1 M KOH electrolyte at 20°C .

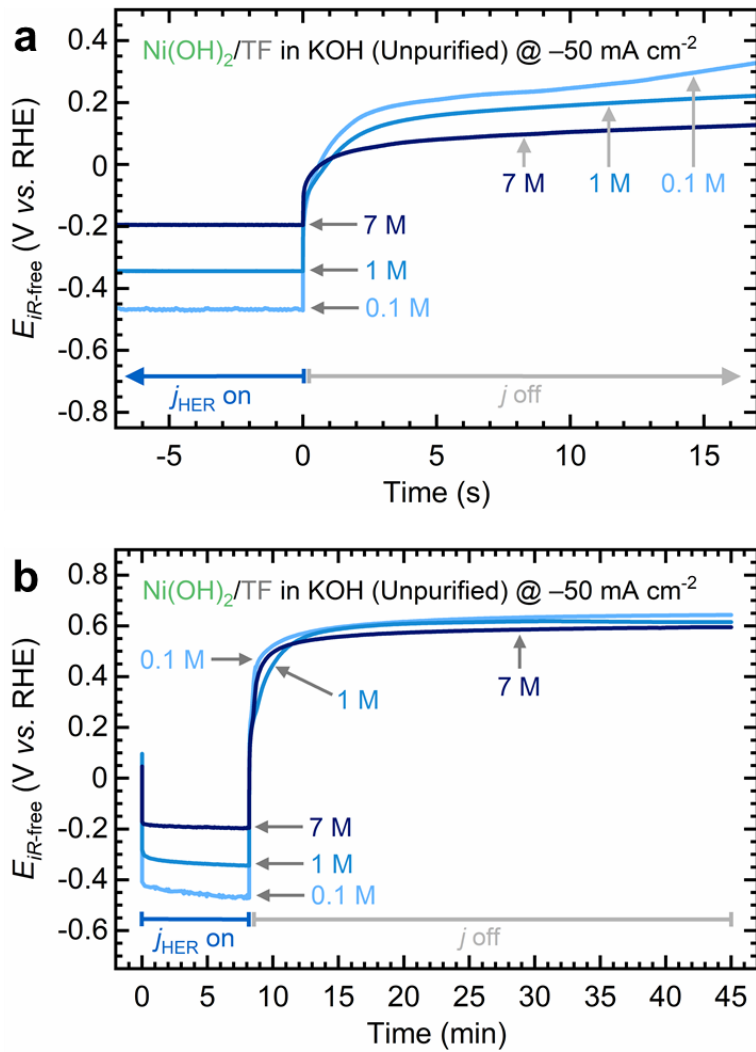


Figure S9. Open circuit potential decay transients for $\text{Ni(OH)}_2/\text{TF}$ electrodes following galvanostatic polarization at a cathodic current density of $-50 \text{ mA}\cdot\text{cm}^{-2}$. Experiments were conducted at increasing concentrations of unpurified KOH electrolyte at 20°C . Profiles are presented on (a) short and (b) long timescales.

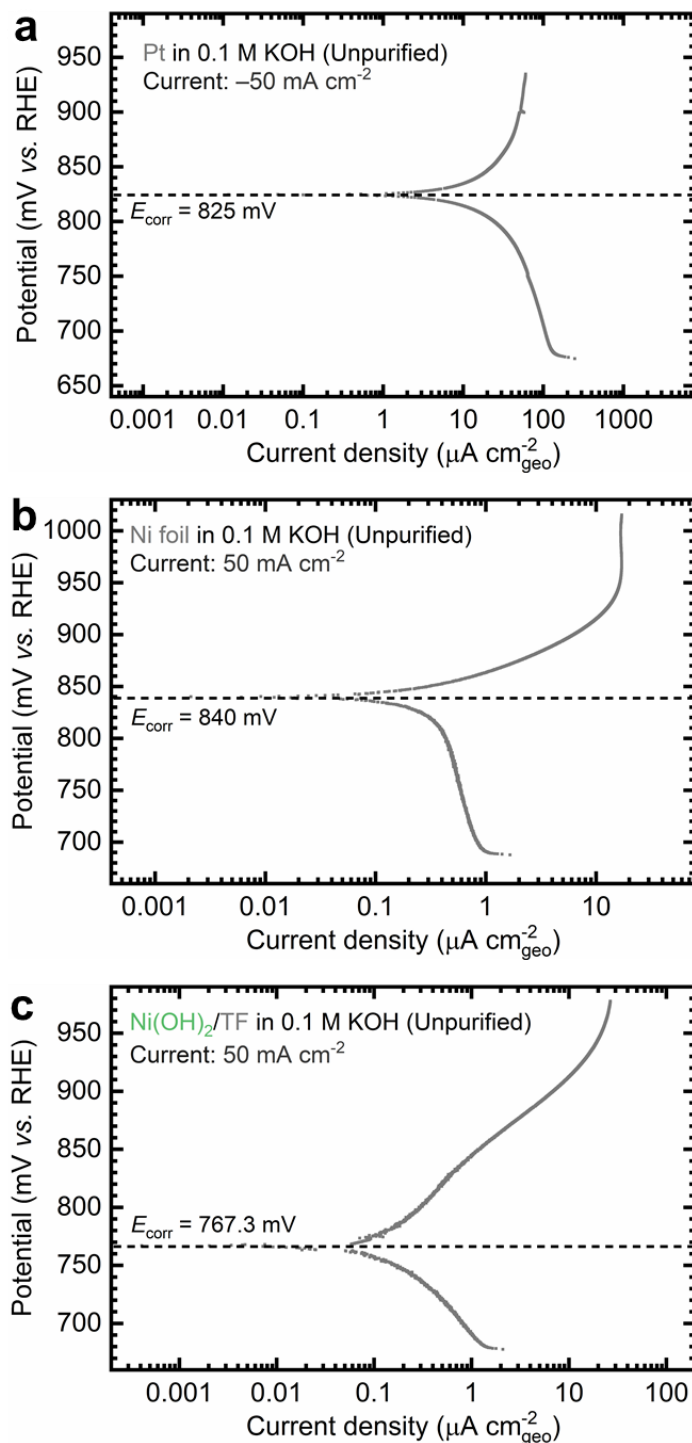


Figure S10. Potentiodynamic polarization plots of (a) Pt, (b) Ni foil, and (c) $\text{Ni(OH)}_2/\text{TF}$ electrodes. Potentiodynamic measurements were carried out following a simulated electrolyzer shutdown test, consisting of a galvanostatic polarization step at $\pm 50 \text{ mA}\cdot\text{cm}^{-2}$ followed by a one-hour electrode potential decay measurement under open circuit conditions. The dashed lines indicate the open circuit potential after one hour, where the total anodic and cathodic currents are equal, corresponding to the corrosion potential (E_{corr}). Experiments were conducted in unpurified 0.1 M KOH electrolyte at 20 °C.

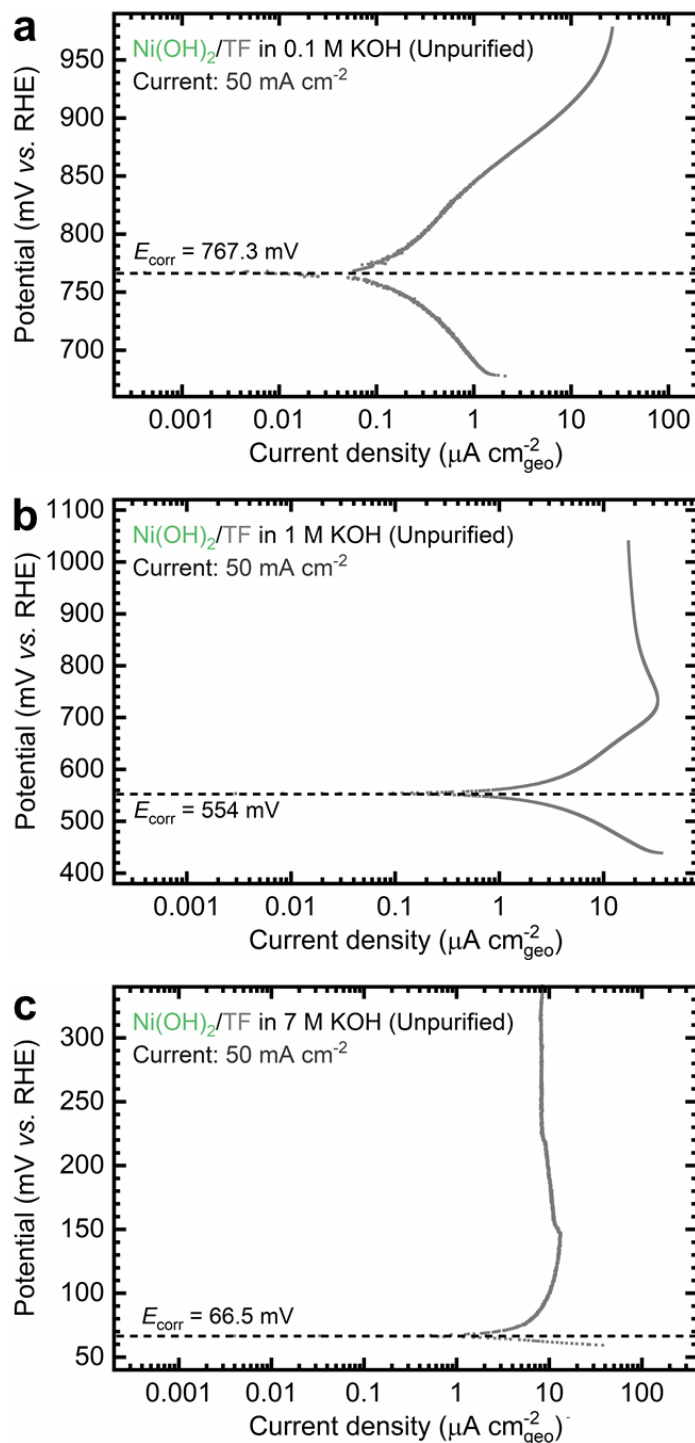


Figure S11. Potentiodynamic polarization plots of Ni(OH)₂/TF electrodes tested in unpurified (a) 0.1 M, (b) 1 M, and (c) 7 M KOH electrolytes. Potentiodynamic measurements were carried out following a simulated electrolyzer shutdown test, consisting of a galvanostatic polarization step at 50 mA·cm⁻² followed by a one-hour electrode potential decay measurement under open circuit conditions. The dashed lines indicate the open circuit potential after one hour, where the total anodic and cathodic currents are equal, corresponding to the corrosion potential (E_{corr}). Experiments were conducted at 20 °C.

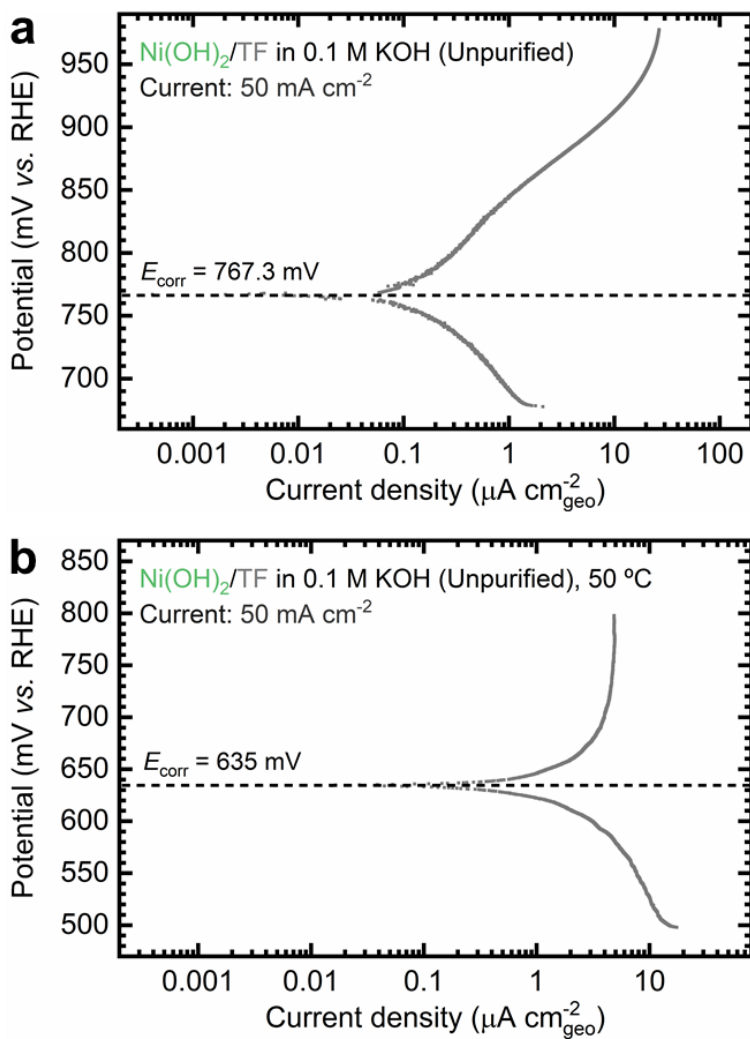


Figure S12. Potentiodynamic polarization plots of Ni(OH)₂/TF electrodes tested in unpurified 0.1 M KOH electrolytes at (a) 20 °C and (b) 50 °C. Potentiodynamic measurements were carried out following a simulated electrolyzer shutdown test, consisting of a galvanostatic polarization step at 50 mA·cm⁻² followed by a one-hour electrode potential decay measurement under open circuit conditions. The dashed lines indicate the open circuit potential after one hour, where the total anodic and cathodic currents are equal, corresponding to the corrosion potential (E_{corr}).

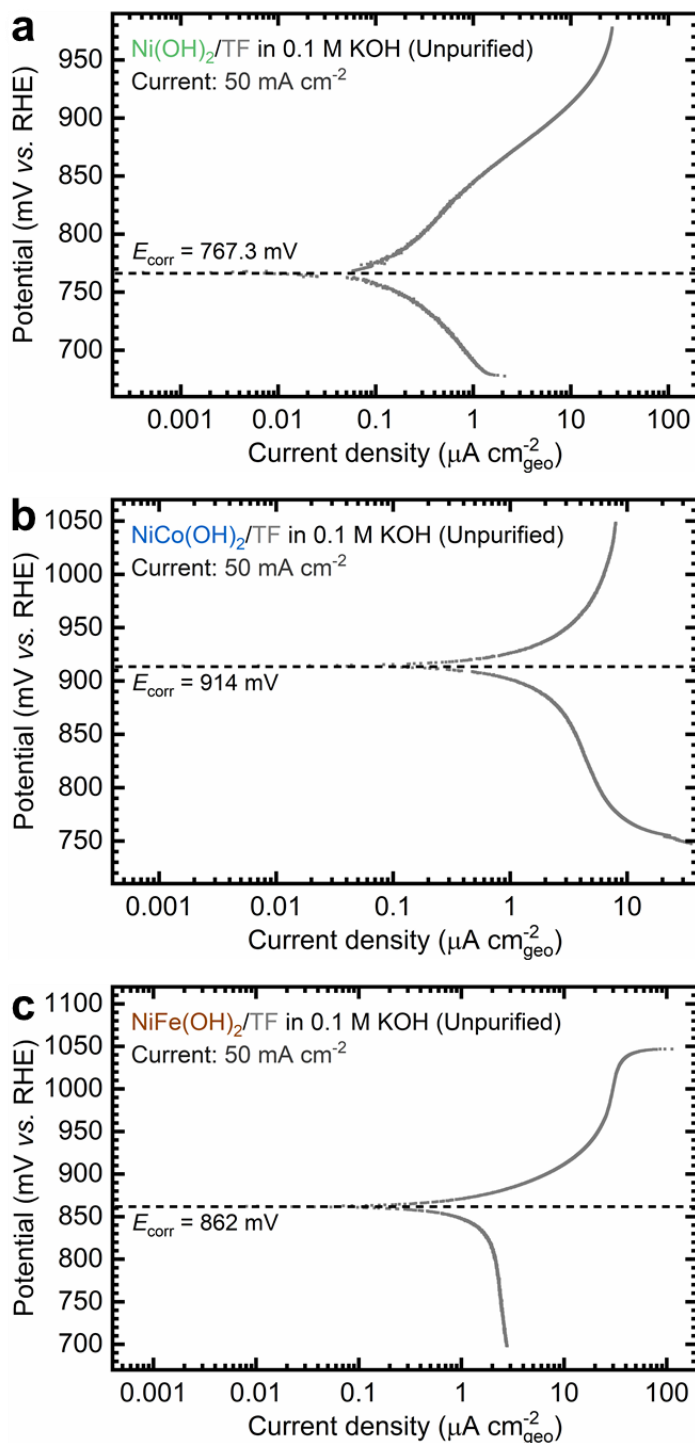


Figure S13. Potentiodynamic polarization plots of (a) Ni(OH)₂/TF, (b) NiCo(OH)₂/TF, and (c) NiFe(OH)₂/TF electrodes. Potentiodynamic measurements were carried out following a simulated electrolyzer shutdown test, consisting of a galvanostatic polarization step at 50 mA·cm⁻² followed by a one-hour electrode potential decay measurement under open circuit conditions. The dashed lines indicate the open circuit potential after one hour, where the total anodic and cathodic currents are equal, corresponding to the corrosion potential (E_{corr}). Experiments were conducted in unpurified 0.1 M KOH electrolyte at 20 °C.

Accelerated catalyst degradation tests in a three-electrode cell

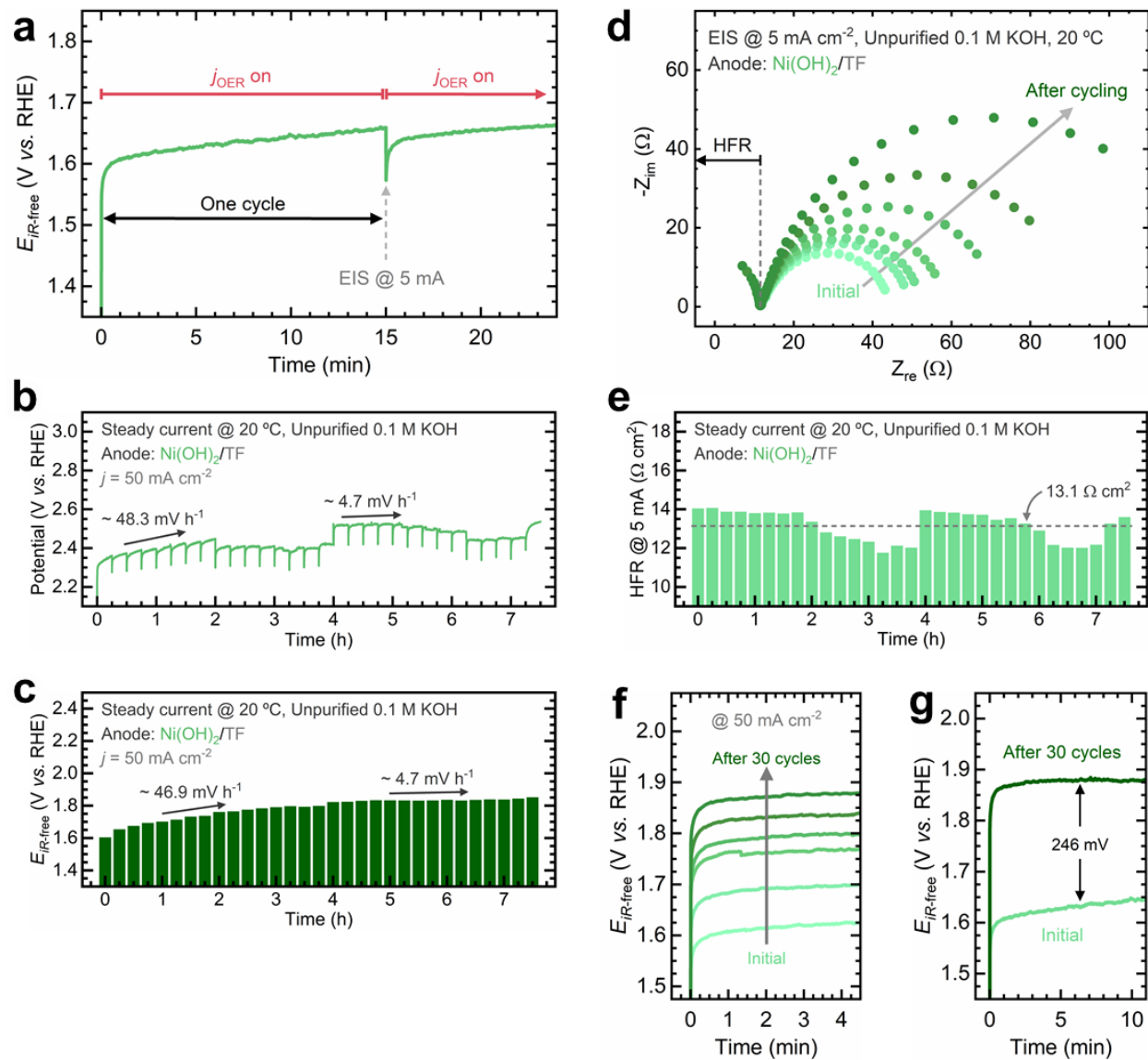


Figure S14. LAWE stability tests under steady-state operation on $\text{Ni(OH)}_2/\text{TF}$ O_2 electrodes: (a) Snapshot of a single cycle, showing the constant current step at 50 mA cm^{-2} followed by an EIS measurement. (b) Electrode potential progression over 30 cycles. (c) iR -corrected electrode potential throughout the stability test, with each bar representing the average potential per cycle. (d) Nyquist plots collected over the stability test. (e) High-frequency resistance (HFR) measured from Nyquist plots over the stability test. (f) Comparison of the iR -corrected electrode potential across cycles. (g) iR -corrected electrode potential curves at the initial and final constant current steps, highlighting their potential differences. The arrows in (b) and (c) indicate the potential increase rate during the highlighted intervals. Grey arrows in (d) and (f) reflect progression over the stability test. The dashed line in (d) represents the HFR value measured from the Nyquist plots. The dashed line in (e) represents the average HFR value and serves as a visual guide only. Experimental conditions: unpurified 0.1 M KOH electrolyte at 20 °C.

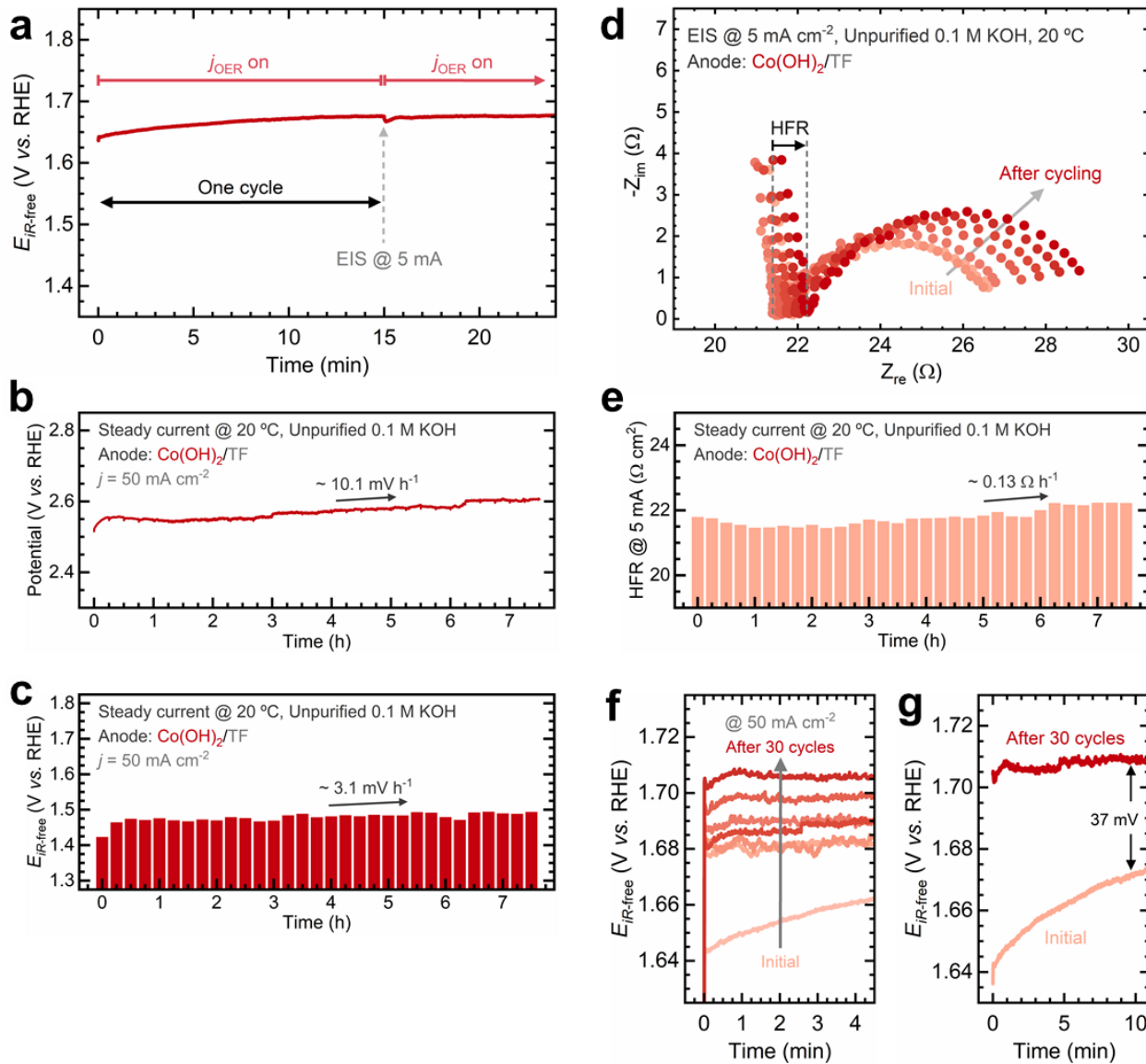


Figure S15. LAWE stability tests under steady-state operation on $\text{Co(OH)}_2/\text{TF}$ O_2 electrodes: (a) Snapshot of a single cycle, showing the constant current step at 50 mA cm^{-2} followed by an EIS measurement. (b) Electrode potential progression over 30 cycles. (c) iR -corrected electrode potential throughout the stability test, with each bar representing the average potential per cycle. (d) Nyquist plots collected over the stability test. (e) HFR measured from Nyquist plots over the stability test. (f) Comparison of the iR -corrected electrode potential across cycles. (g) iR -corrected electrode potential curves at the initial and final constant current steps, highlighting their potential differences. The arrows in (b) and (c) indicate the potential increase rate during the highlighted intervals. The dashed lines and black arrow in (d) indicate the progression of the HFR values during cycling, while the grey arrow represents the evolution of the semicircle throughout the stability test. The arrow in (e) indicates the HFR increase rate during the highlighted interval. Experimental conditions: unpurified 0.1 M KOH electrolyte at 20 °C.

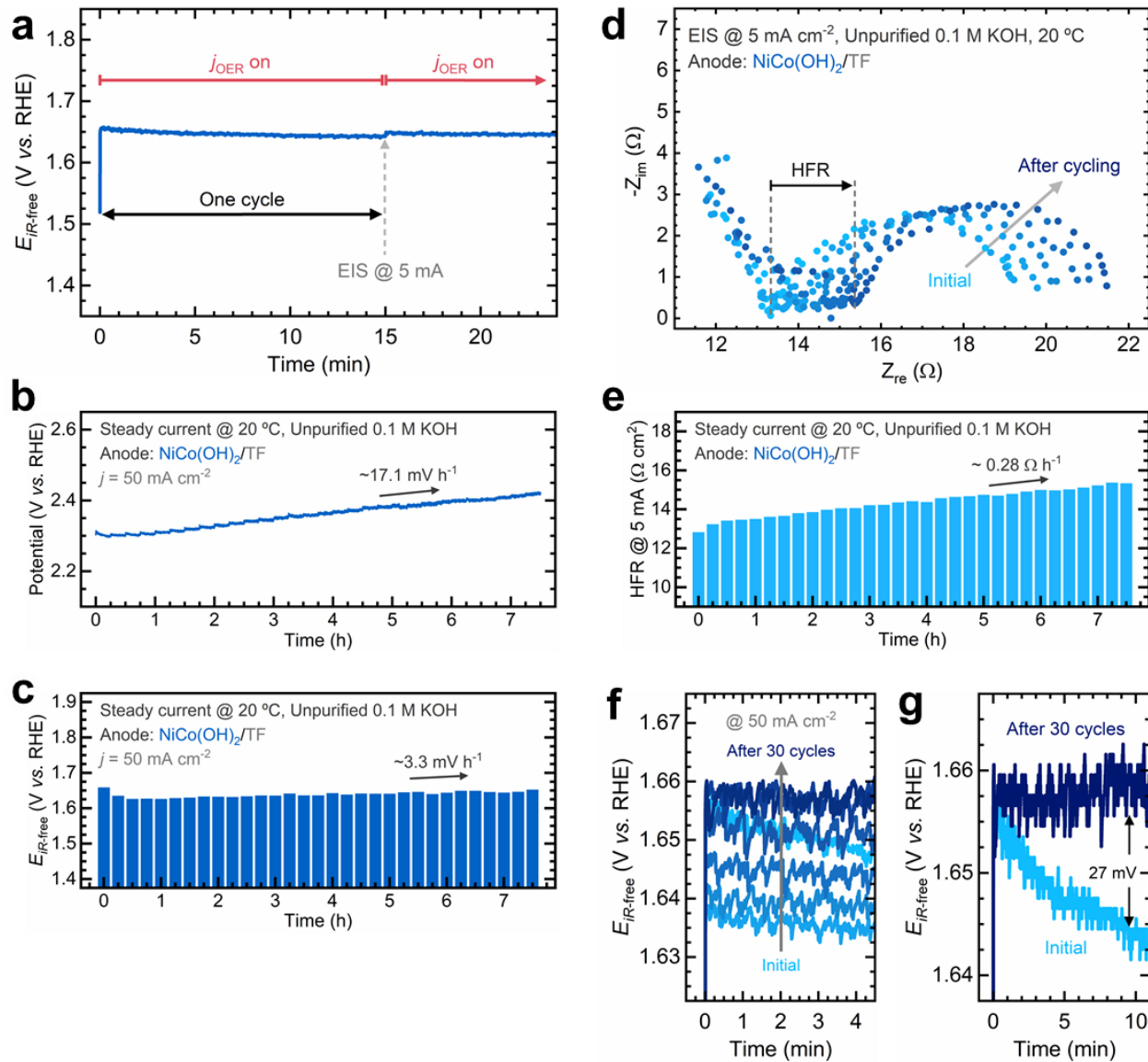


Figure S16. LAWE stability tests under steady-state operation on $\text{NiCo}(\text{OH})_2/\text{TF}$ O_2 electrodes: (a) Snapshot of a single cycle, showing the constant current step at 50 mA cm^{-2} followed by an EIS measurement. (b) Electrode potential progression over 30 cycles. (c) iR -corrected electrode potential throughout the stability test, with each bar representing the average potential per cycle. (d) Nyquist plots collected over the stability test. (e) HFR measured from Nyquist plots over the stability test. (f) Comparison of the iR -corrected electrode potential across cycles. (g) iR -corrected electrode potential curves at the initial and final constant current steps, highlighting their potential differences. The arrows in (b) and (c) indicate the potential increase rate during the highlighted intervals. The dashed lines and black arrow in (d) indicate the progression of the HFR values during cycling, while the grey arrow represents the evolution of the semicircle throughout the stability test. The arrow in (e) indicates the HFR increase rate during the highlighted interval. Experimental conditions: unpurified 0.1 M KOH electrolyte at 20°C .

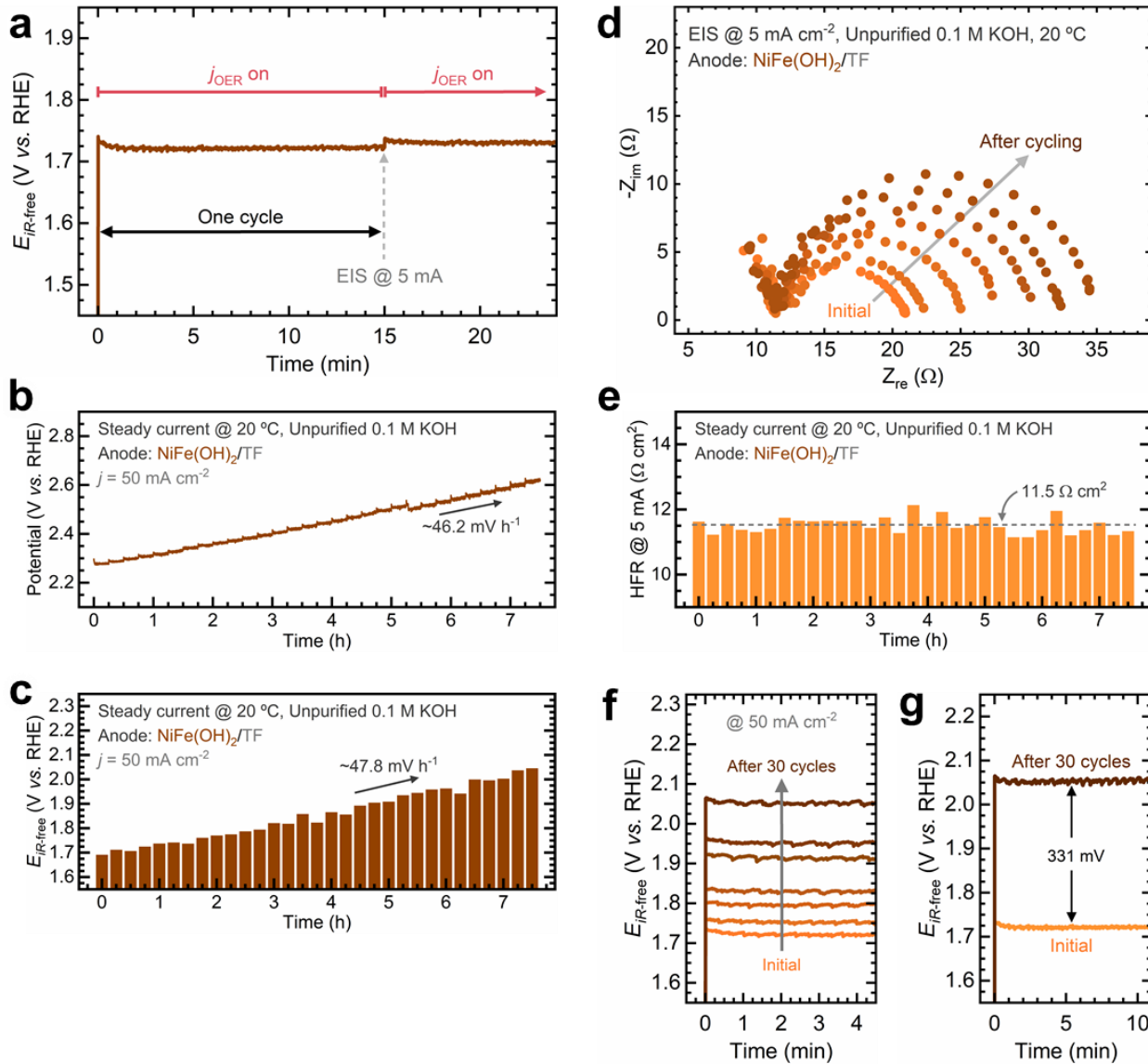


Figure S17. LAWE stability tests under steady-state operation on $\text{NiFe}(\text{OH})_2/\text{TF}$ O_2 electrodes: (a) Snapshot of a single cycle, showing the constant current step at $50 \text{ mA}\cdot\text{cm}^{-2}$ followed by an EIS measurement. (b) Electrode potential progression over 30 cycles. (c) iR -corrected electrode potential throughout the stability test, with each bar representing the average potential per cycle. (d) Nyquist plots collected over the stability test. (e) HFR measured from Nyquist plots over the stability test. (f) Comparison of the iR -corrected electrode potential across cycles. (g) iR -corrected electrode potential curves at the initial and final constant current steps, highlighting their potential differences. The arrows in (b) and (c) indicate the potential increase rate during the highlighted intervals. The grey arrow in (d) represents the evolution of the semicircle throughout the stability test. The dashed line in (e) represents the average HFR value and serves as a visual guide only. Experimental conditions: unpurified 0.1 M KOH electrolyte at 20 °C.

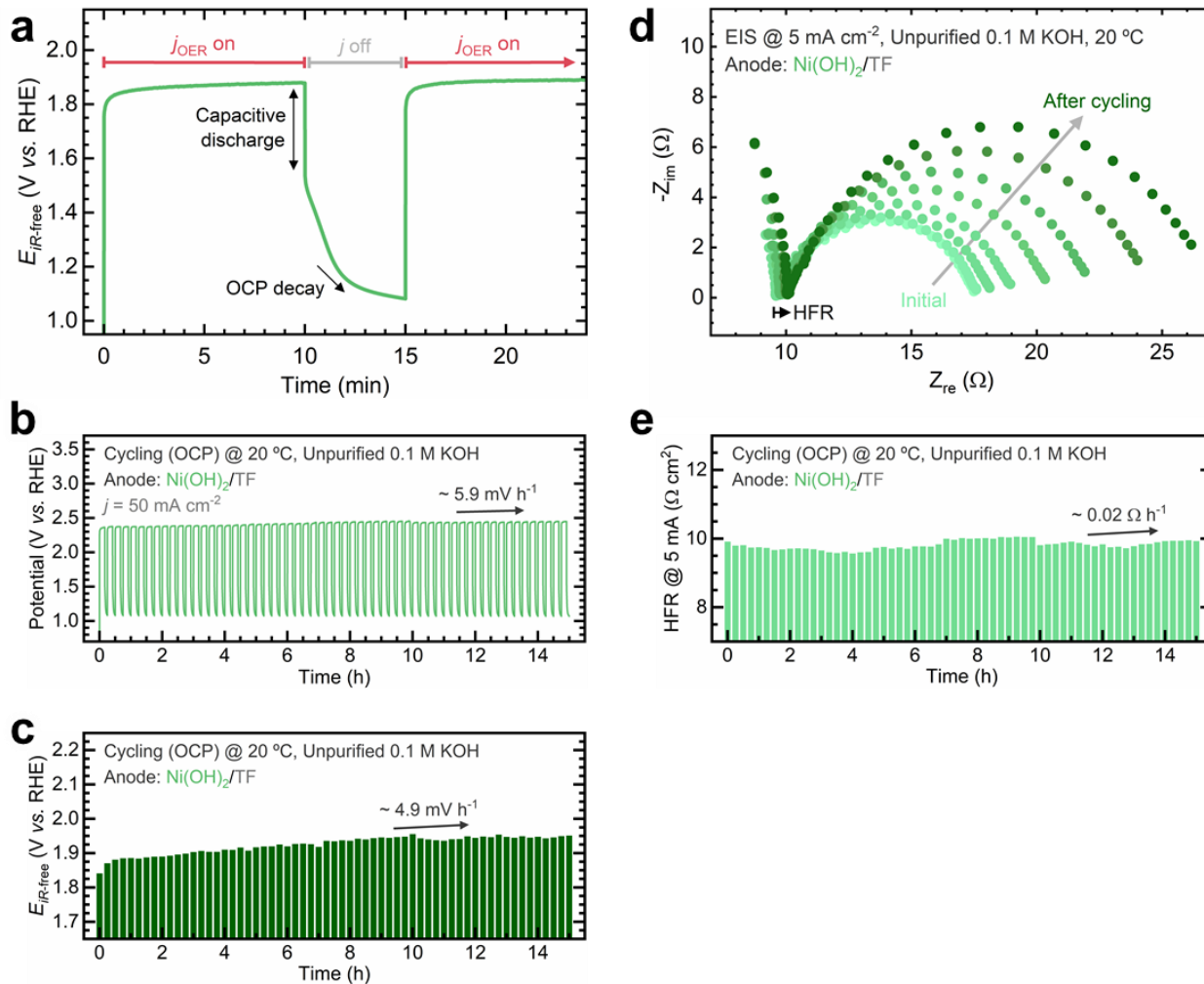


Figure S18. LAWE stability tests under variable operation with an OCP step on $\text{Ni(OH)}_2/\text{TF}$ O_2 electrodes: (a) Snapshot of a single cycle, showing the constant current step at 50 mA cm^{-2} followed by an OCP step to simulate shutdown. (b) Electrode potential progression over 60 cycles. (c) iR -corrected electrode potential throughout the stability test, with each bar representing the average potential during the constant current step per cycle. (d) Nyquist plots collected over the stability test. (e) HFR measured from Nyquist plots over the stability test. The arrows in (b) and (c) indicate the potential increase rate during the highlighted intervals. The black arrow in (d) indicates the progression of the HFR values during cycling, while the grey arrow represents the evolution of the semicircle throughout the stability test. The arrow in (e) indicates the HFR increase rate during the highlighted interval. Experimental conditions: unpurified 0.1 M KOH electrolyte at 20 °C.

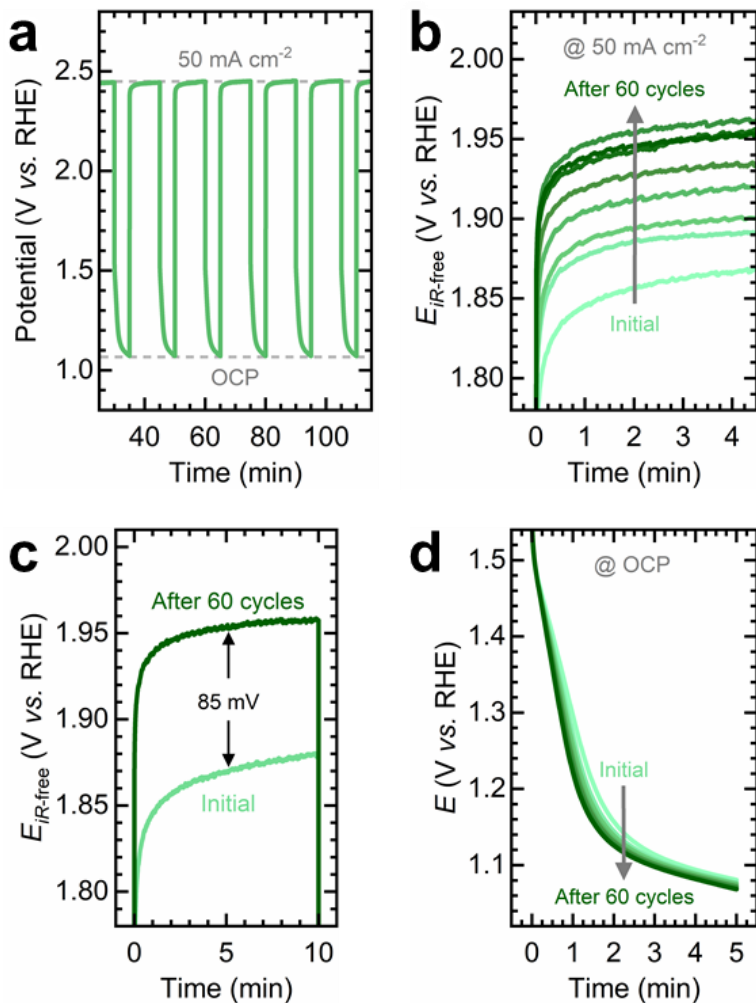


Figure S19. LAWE stability tests under variable operation with an OCP step on $\text{Ni}(\text{OH})_2/\text{TF}$ O_2 electrodes: (a) Snapshot of the electrode potential profile under variable operation, highlighting the potential thresholds reached during the constant current and OCP steps. (b) Comparison of the $i\text{R}$ -corrected electrode potential across cycles. (c) $i\text{R}$ -corrected electrode potential curves at the initial and final constant current steps, highlighting their potential differences. (d) Comparison of OCP decay profiles across cycles. The arrows in (b) and (d) indicate the progression of potential profiles during cycling.

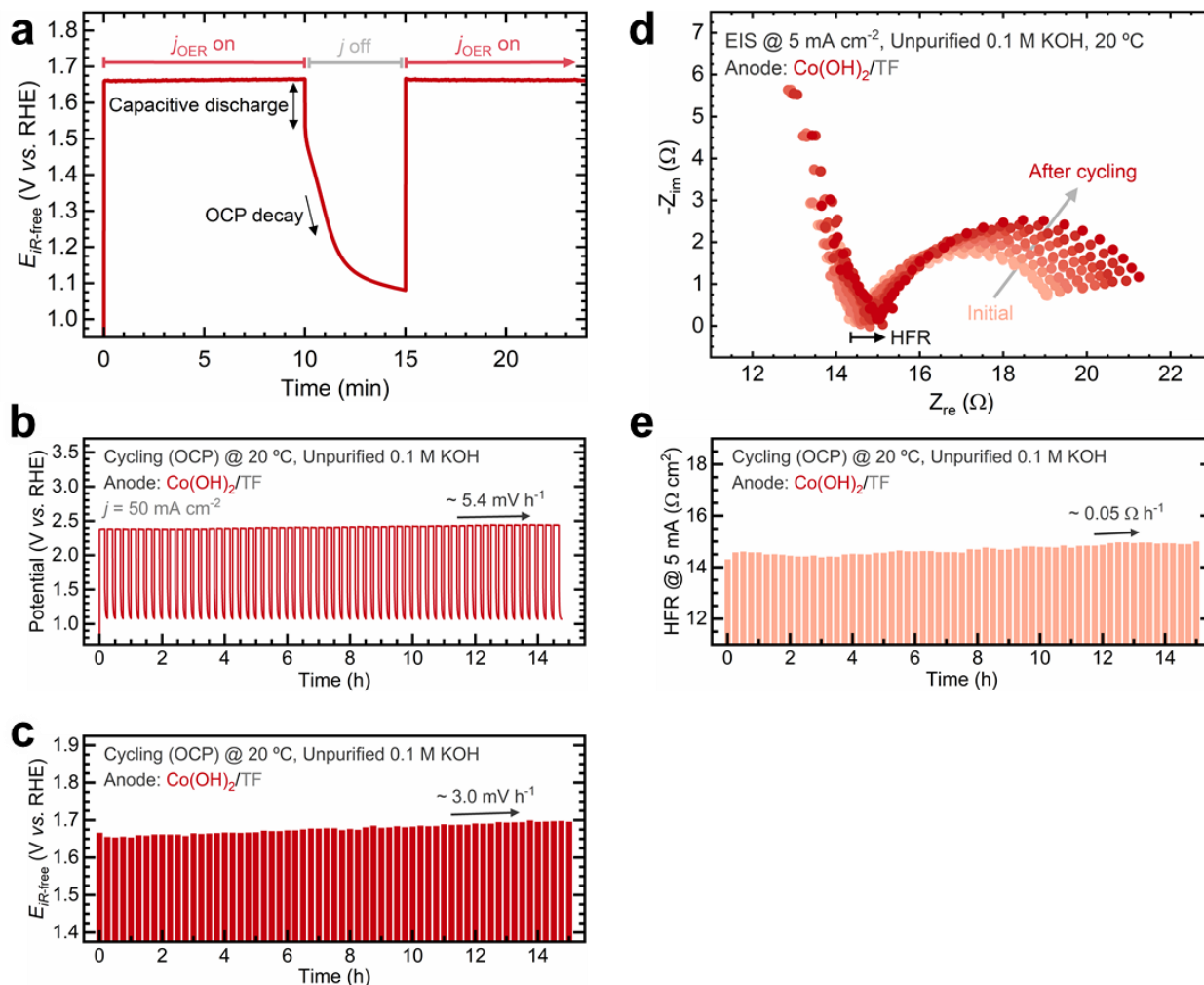


Figure S20. LAWE stability tests under variable operation with an OCP step on $\text{Co(OH)}_2/\text{TF}$ O_2 electrodes: (a) Snapshot of a single cycle, showing the constant current step at $50 \text{ mA}\cdot\text{cm}^{-2}$ followed by an OCP step to simulate shutdown. (b) Electrode potential progression over 60 cycles. (c) iR -corrected electrode potential throughout the stability test, with each bar representing the average potential during the constant current step per cycle. (d) Nyquist plots collected over the stability test. (e) HFR measured from Nyquist plots over the stability test. The arrows in (b) and (c) indicate the potential increase rate during the highlighted intervals. The black arrow in (d) indicates the progression of the HFR values during cycling, while the grey arrow represents the evolution of the semicircle throughout the stability test. The arrow in (e) indicates the HFR increase rate during the highlighted interval. Experimental conditions: unpurified 0.1 M KOH electrolyte at 20°C .

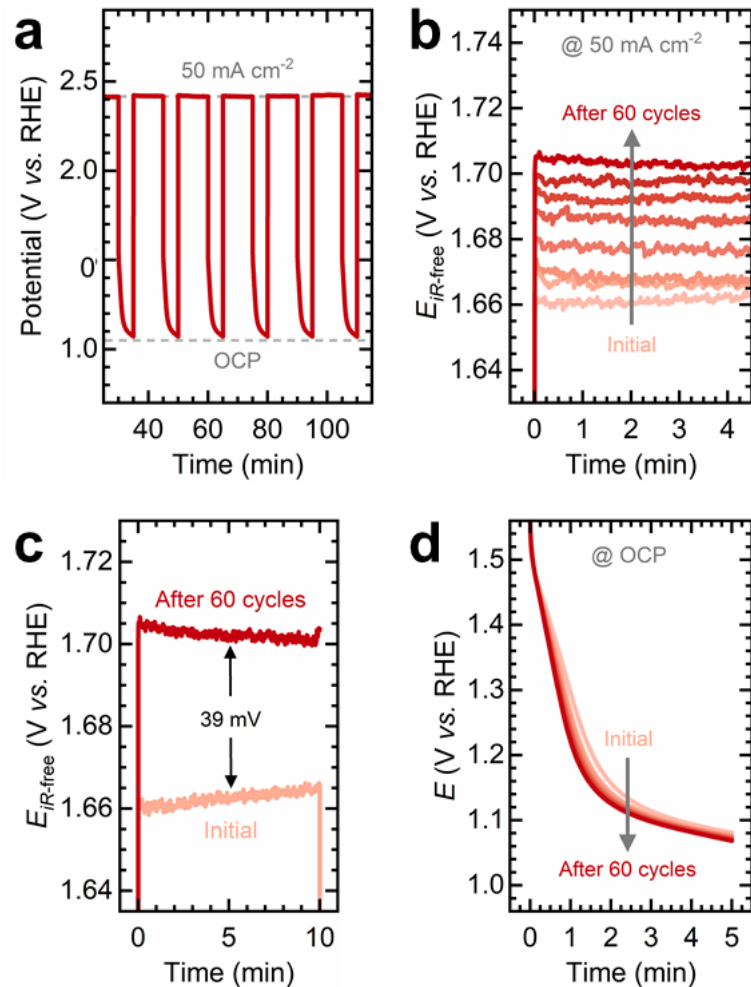


Figure S21. LAWE stability tests under variable operation with an OCP step on $\text{Co}(\text{OH})_2/\text{TF}$ O_2 electrodes: (a) Snapshot of the electrode potential profile under variable operation, highlighting the potential thresholds reached during the constant current and OCP steps. (b) Comparison of the $i\text{R}$ -corrected electrode potential across cycles. (c) $i\text{R}$ -corrected electrode potential curves at the initial and final constant current steps, highlighting their potential differences. (d) Comparison of OCP decay profiles across cycles. The arrows in (b) and (d) indicate the progression of potential profiles during cycling.

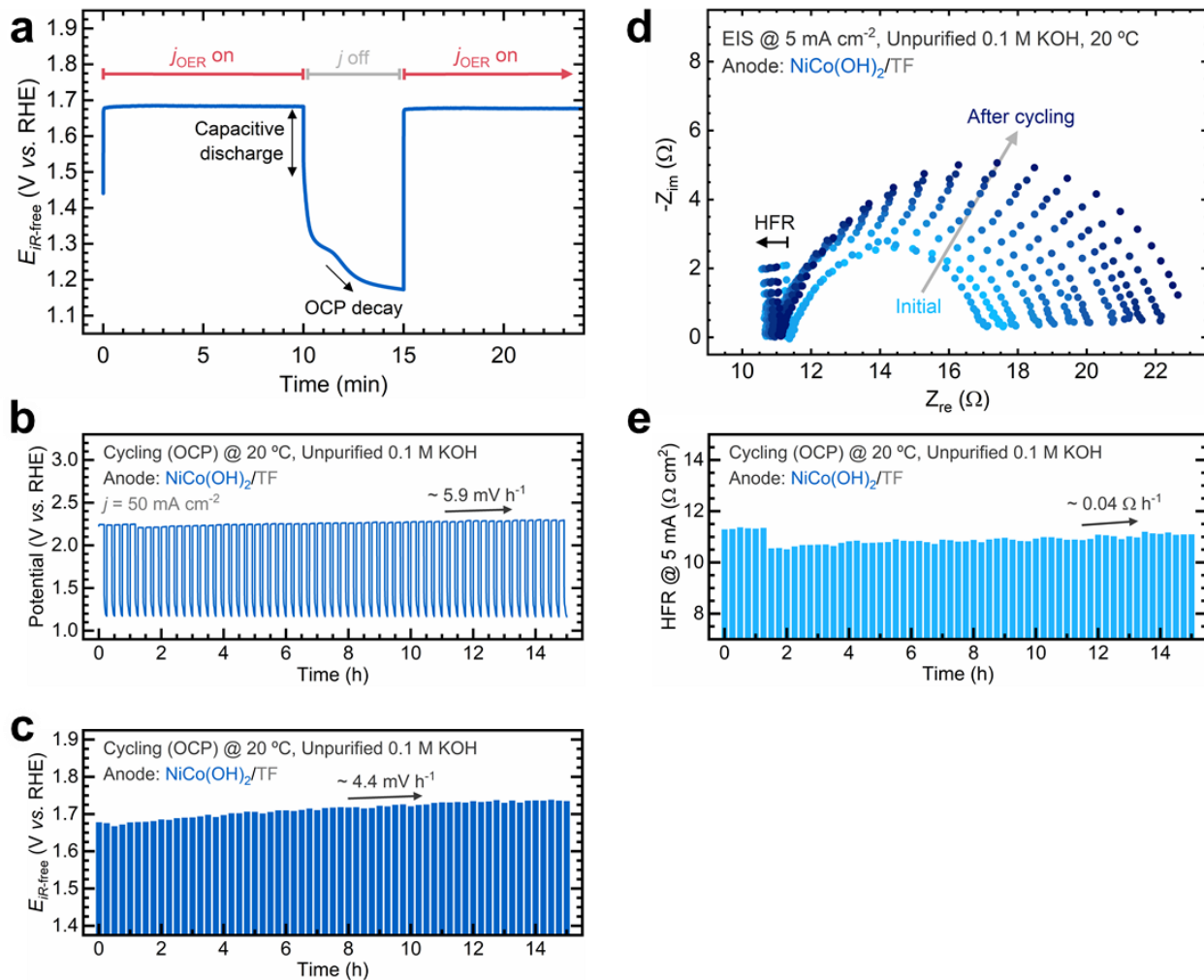


Figure S22. LAWE stability tests under variable operation with an OCP step on $\text{NiCo}(\text{OH})_2/\text{TF}$ O_2 electrodes: (a) Snapshot of a single cycle, showing the constant current step at 50 mA cm^{-2} followed by an OCP step to simulate shutdown. (b) Electrode potential progression over 60 cycles. (c) iR -corrected electrode potential throughout the stability test, with each bar representing the average potential during the constant current step per cycle. (d) Nyquist plots collected over the stability test. (e) HFR measured from Nyquist plots over the stability test. The arrows in (b) and (c) indicate the potential increase rate during the highlighted intervals. The black arrow in (d) indicates the progression of the HFR values during cycling, while the grey arrow represents the evolution of the semicircle throughout the stability test. The arrow in (e) indicates the HFR increase rate during the highlighted interval. Experimental conditions: unpurified 0.1 M KOH electrolyte at 20 °C.

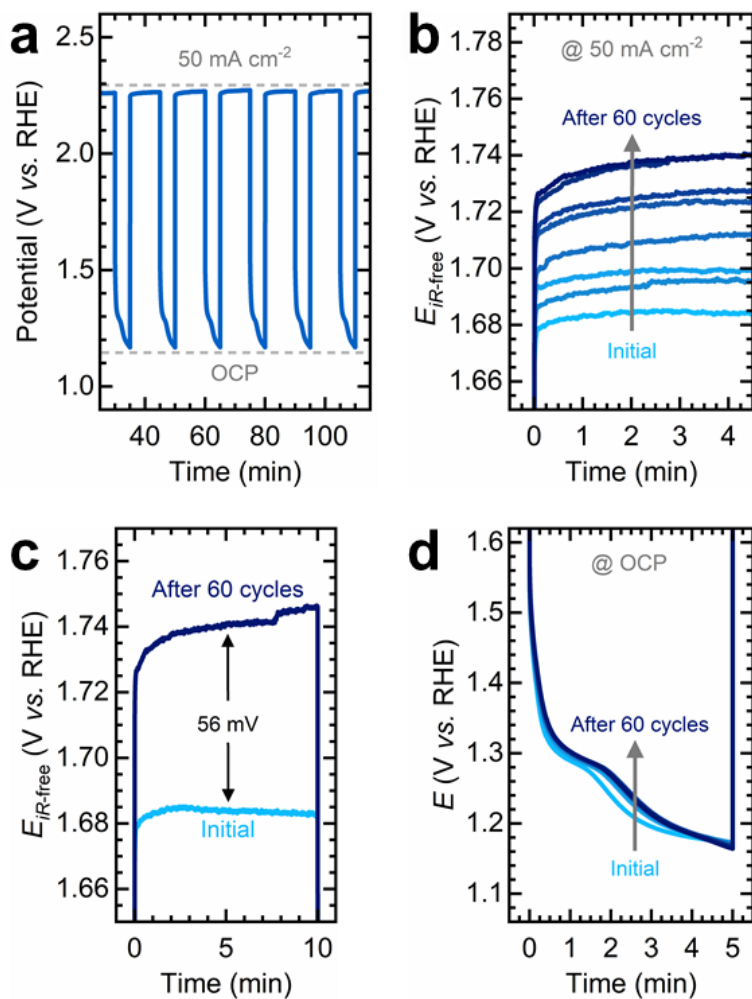


Figure S23. LAWE stability tests under variable operation with an OCP step on $\text{NiCo}(\text{OH})_2/\text{TF}$ O_2 electrodes: (a) Snapshot of the electrode potential profile under variable operation, highlighting the potential thresholds reached during the constant current and OCP steps. (b) Comparison of the $i\text{R}$ -corrected electrode potential across cycles. (c) $i\text{R}$ -corrected electrode potential curves at the initial and final constant current steps, highlighting their potential differences. (d) Comparison of OCP decay profiles across cycles. The arrows in (b) and (d) indicate the progression of potential profiles during cycling.

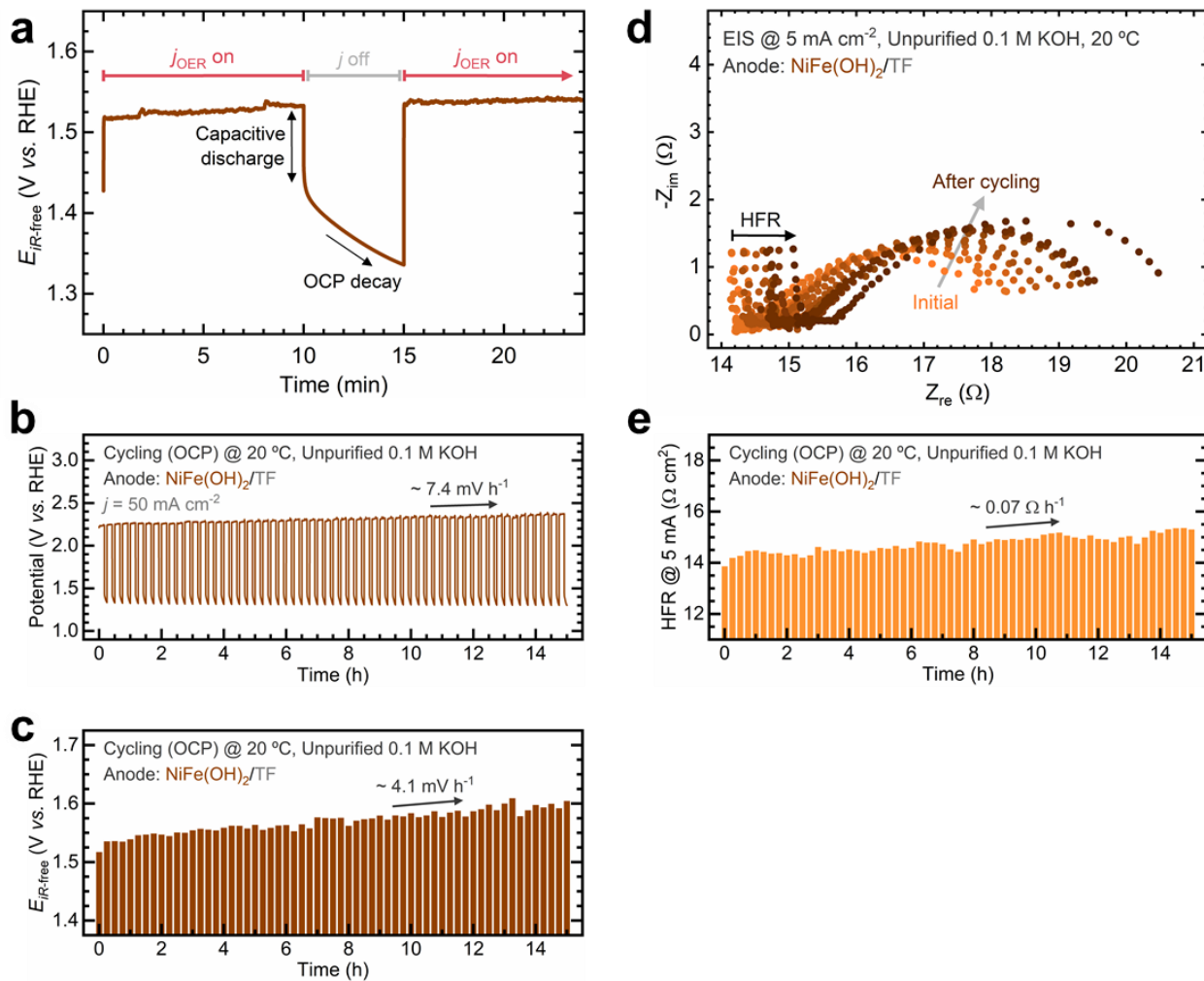


Figure S24. LAWE stability tests under variable operation with an OCP step on $\text{NiFe}(\text{OH})_2/\text{TF}$ O_2 electrodes: (a) Snapshot of a single cycle, showing the constant current step at 50 mA cm^{-2} followed by an OCP step to simulate shutdown. (b) Electrode potential progression over 60 cycles. (c) iR -corrected electrode potential throughout the stability test, with each bar representing the average potential during the constant current step per cycle. (d) Nyquist plots collected over the stability test. (e) HFR measured from Nyquist plots over the stability test. The arrows in (b) and (c) indicate the potential increase rate during the highlighted intervals. The black arrow in (d) indicates the progression of the HFR values during cycling, while the grey arrow represents the evolution of the semicircle throughout the stability test. The arrow in (e) indicates the HFR increase rate during the highlighted interval. Experimental conditions: unpurified 0.1 M KOH electrolyte at 20 °C.

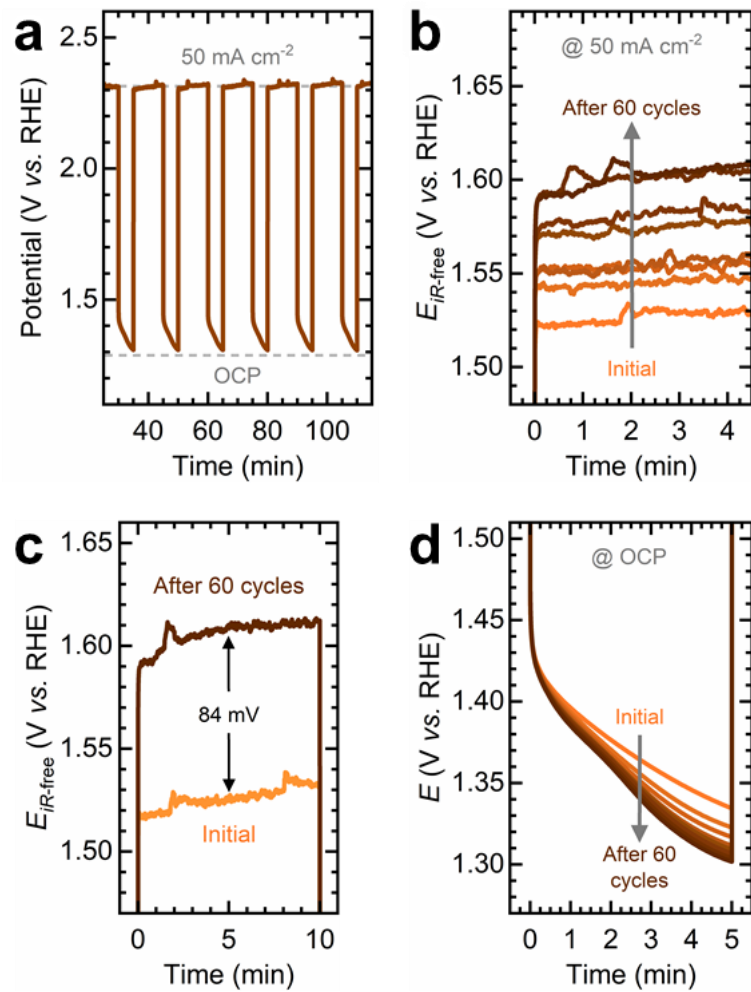


Figure S25. LAWE stability tests under variable operation with an OCP step on NiFe(OH)₂/TF O₂ electrodes: (a) Snapshot of the electrode potential profile under variable operation, highlighting the potential thresholds reached during the constant current and OCP steps. (b) Comparison of the *iR*-corrected electrode potential across cycles. (c) *iR*-corrected electrode potential curves at the initial and final constant current steps, highlighting their potential differences. (d) Comparison of OCP decay profiles across cycles. The arrows in (b) and (d) indicate the progression of potential profiles during cycling.

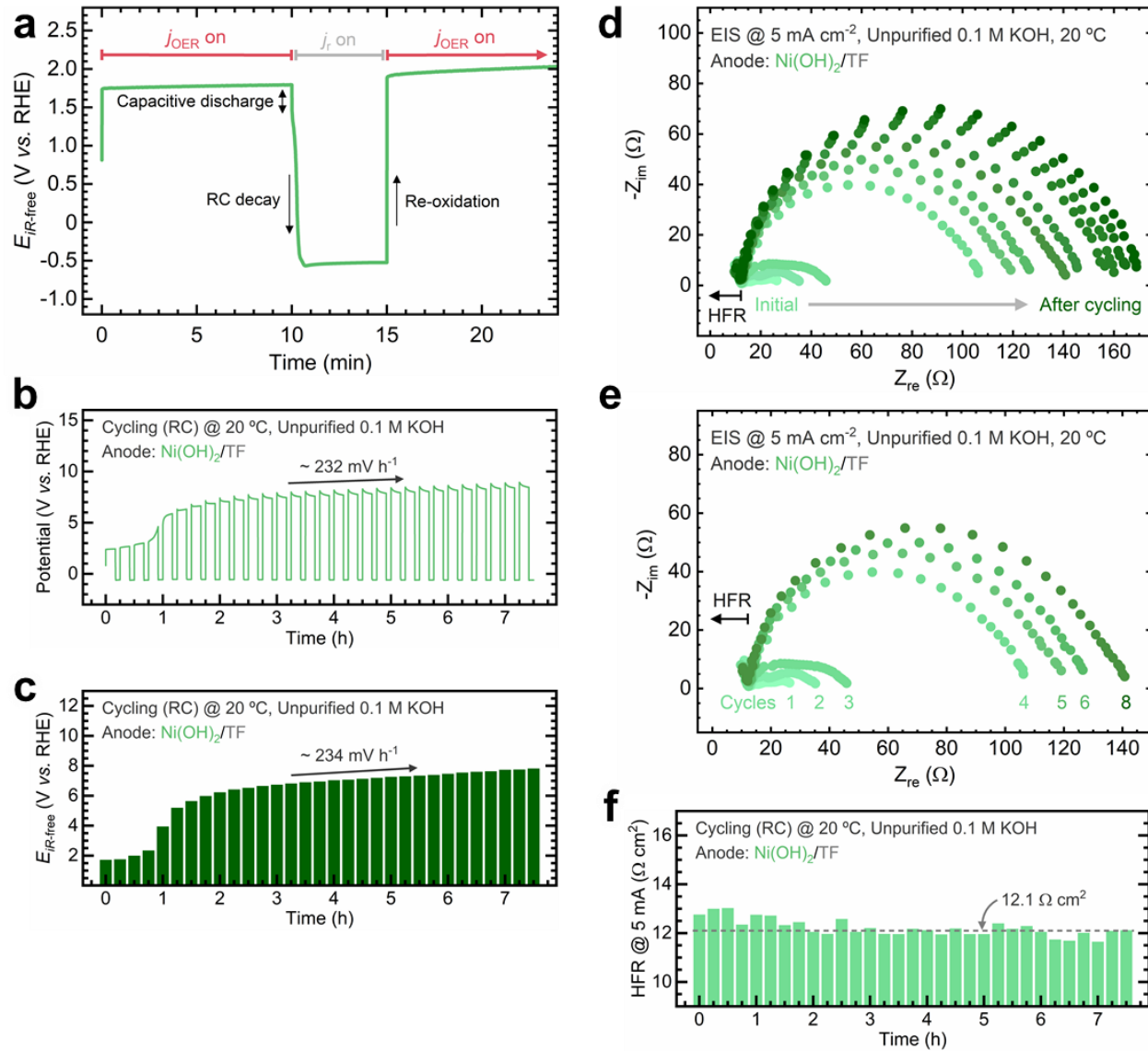


Figure S26. LAWE stability tests under variable operation with a reverse current (RC) step on $\text{Ni(OH)}_2/\text{TF}$ O_2 electrodes: (a) Snapshot of a single cycle, showing the constant current step at $50 \text{ mA}\cdot\text{cm}^{-2}$ followed by a reverse current step of $-5 \text{ mA}\cdot\text{cm}^{-2}$ to simulate shutdown. (b) Electrode potential progression over 30 cycles. (c) iR -corrected electrode potential throughout the stability test, with each bar representing the average potential during the constant current step per cycle. (d) Nyquist plots collected over the stability test. (e) Magnified view of Nyquist plots from the initial cycles. (f) HFR measured from Nyquist plots over the stability test. The arrows in (b) and (c) indicate the potential increase rate during the highlighted intervals. The black arrows in (d) and (e) indicate the progression of the HFR values during cycling, while the grey arrow represents the evolution of the semicircle throughout the stability test. The dashed line in (f) represents the average HFR value and serves as a visual guide only. Experimental conditions: unpurified 0.1 M KOH electrolyte at 20 °C.

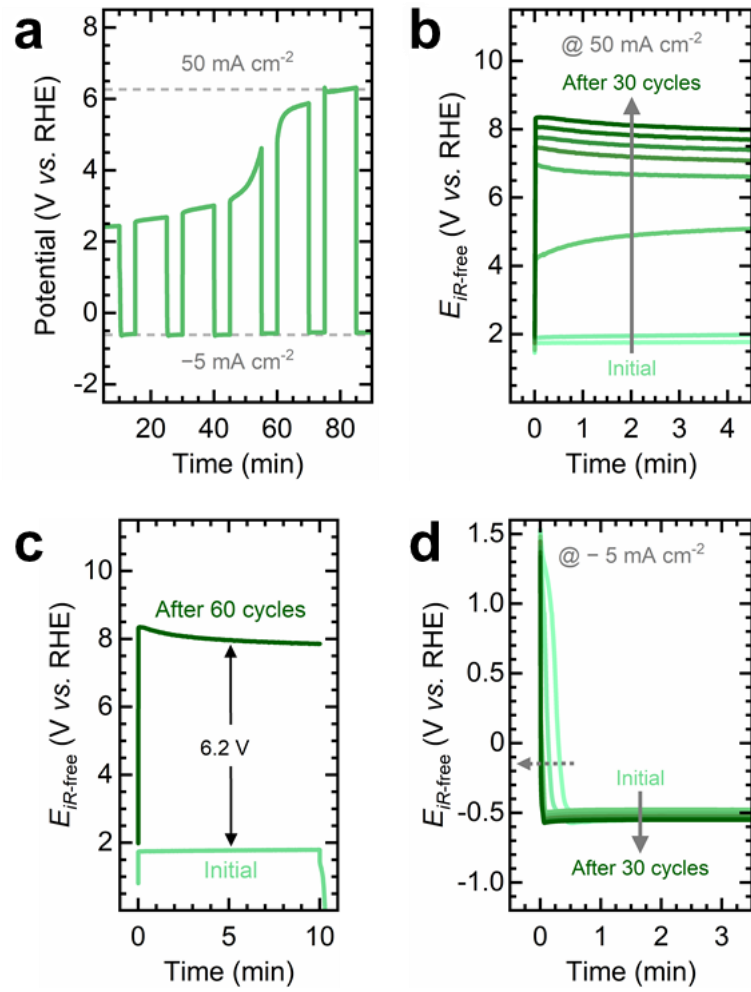


Figure S27. LAWE stability tests under variable operation with a reverse current (RC) step on Ni(OH)₂/TF O₂ electrodes: (a) Snapshot of the electrode potential profile under variable operation, highlighting the potential thresholds reached during the constant current and reverse current steps. (b) Comparison of the *iR*-corrected electrode potential across cycles. (c) *iR*-corrected electrode potential curves at the initial and final constant current steps, highlighting their potential differences. (d) Comparison of the *iR*-corrected electrode potential during the reverse current step across cycles. The arrows in (b) and (d) indicate the progression of potential profiles during cycling.

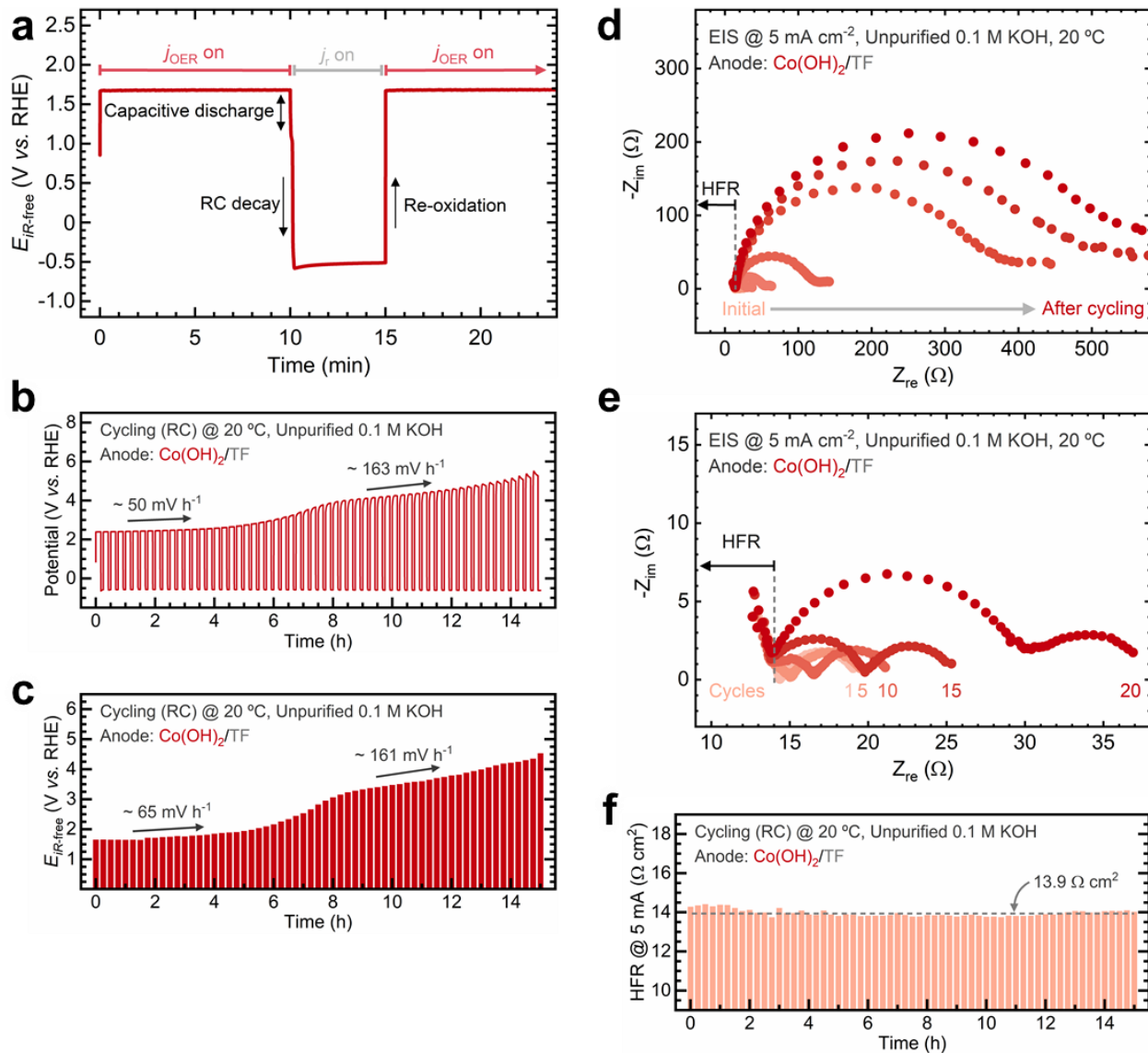


Figure S28. LAWE stability tests under variable operation with a reverse current step on $\text{Co(OH)}_2/\text{TF}$ O_2 electrodes: (a) Snapshot of a single cycle, showing the constant current step at $50 \text{ mA}\cdot\text{cm}^{-2}$ followed by a reverse current step of $-5 \text{ mA}\cdot\text{cm}^{-2}$ to simulate shutdown. (b) Electrode potential progression over 30 cycles. (c) iR -corrected electrode potential throughout the stability test, with each bar representing the average potential during the constant current step per cycle. (d) Nyquist plots collected over the stability test. (e) Magnified view of Nyquist plots from the initial cycles. (f) HFR measured from Nyquist plots over the stability test. The arrows in (b) and (c) indicate the potential increase rate during the highlighted intervals. The black arrows in (d) and (e) indicate the HFR values during cycling, while the grey arrow represents the evolution of the semicircle throughout the stability test. The dashed line in (f) represents the average HFR value and serves as a visual guide only. Experimental conditions: unpurified 0.1 M KOH electrolyte at 20 °C.

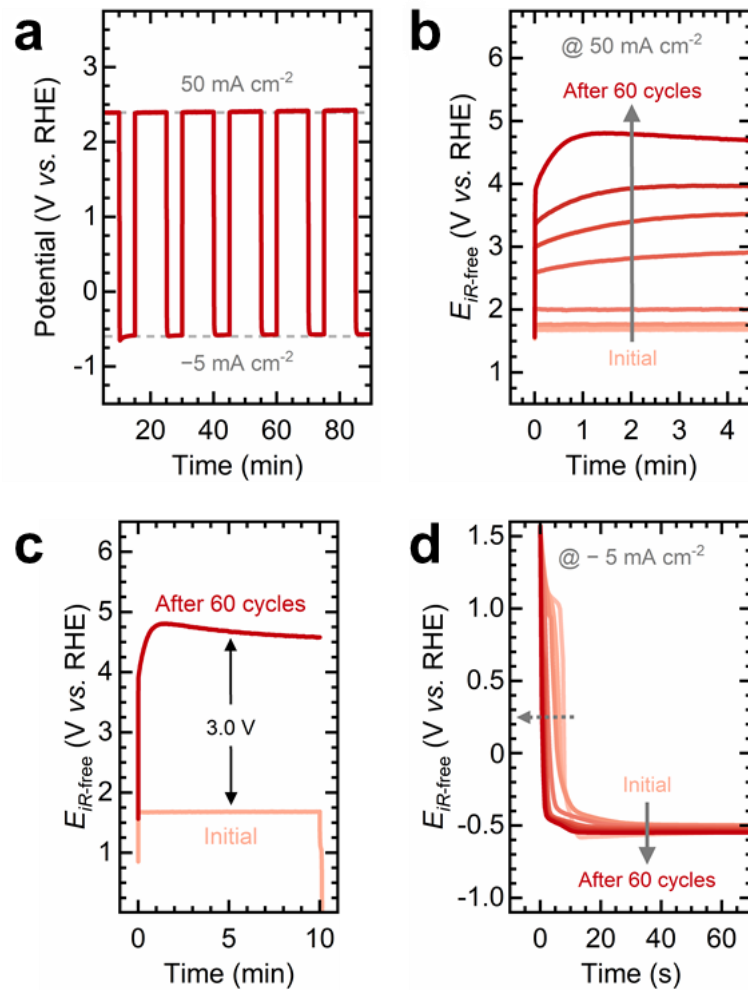


Figure S29. LAWE stability tests under variable operation with a reverse current step on $\text{Co}(\text{OH})_2/\text{TF O}_2$ electrodes: (a) Snapshot of the electrode potential profile under variable operation, highlighting the potential thresholds reached during the constant current and reverse current steps. (b) Comparison of the $i\text{R}$ -corrected electrode potential across cycles. (c) $i\text{R}$ -corrected electrode potential curves at the initial and final constant current steps, highlighting their potential differences. (d) Comparison of the $i\text{R}$ -corrected electrode potential during the reverse current step across cycles. The arrows in (b) and (d) indicate the progression of potential profiles during cycling.

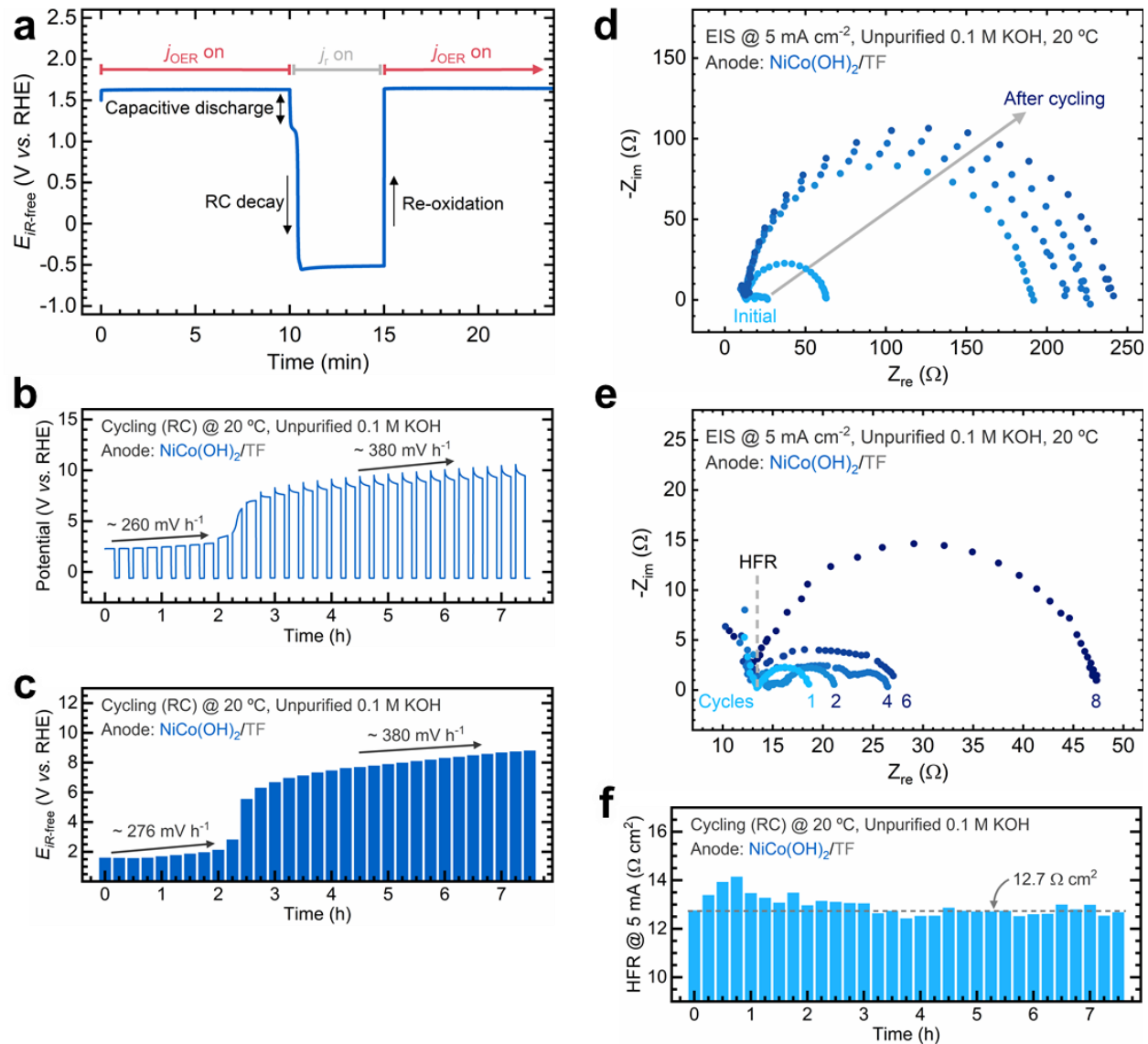


Figure S30. LAWE stability tests under variable operation with a reverse current step on $\text{NiCo}(\text{OH})_2/\text{TF}$ O_2 electrodes: (a) Snapshot of a single cycle, showing the constant current step at $50 \text{ mA}\cdot\text{cm}^{-2}$ followed by a reverse current step of $-5 \text{ mA}\cdot\text{cm}^{-2}$ to simulate shutdown. (b) Electrode potential progression over 30 cycles. (c) iR -corrected electrode potential throughout the stability test, with each bar representing the average potential during the constant current step per cycle. (d) Nyquist plots collected over the stability test. (e) Magnified view of Nyquist plots from the initial cycles. (f) HFR measured from Nyquist plots over the stability test. The arrows in (b) and (c) indicate the potential increase rate during the highlighted intervals. The grey arrow in (d) represents the evolution of the semicircle throughout the stability test, while the dashed line in (e) indicates the HFR value during cycling. The dashed line in (f) represents the average HFR value and serves as a visual guide only. Experimental conditions: unpurified 0.1 M KOH electrolyte at 20 °C.

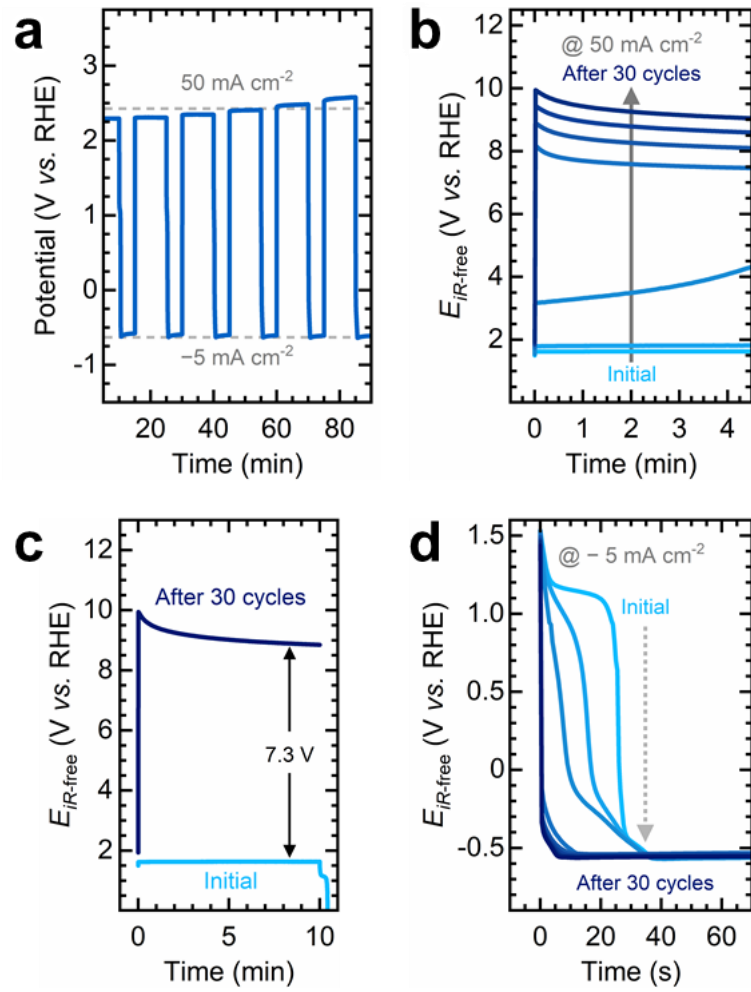


Figure S31. LAWE stability tests under variable operation with a reverse current step on $\text{NiCo}(\text{OH})_2/\text{TF O}_2$ electrodes: (a) Snapshot of the electrode potential profile under variable operation, highlighting the potential thresholds reached during the constant current and reverse current steps. (b) Comparison of the $i\text{R}$ -corrected electrode potential across cycles. (c) $i\text{R}$ -corrected electrode potential curves at the initial and final constant current steps, highlighting their potential differences. (d) Comparison of the $i\text{R}$ -corrected electrode potential during the reverse current step across cycles. The arrows in (b) and (d) indicate the progression of potential profiles during cycling.

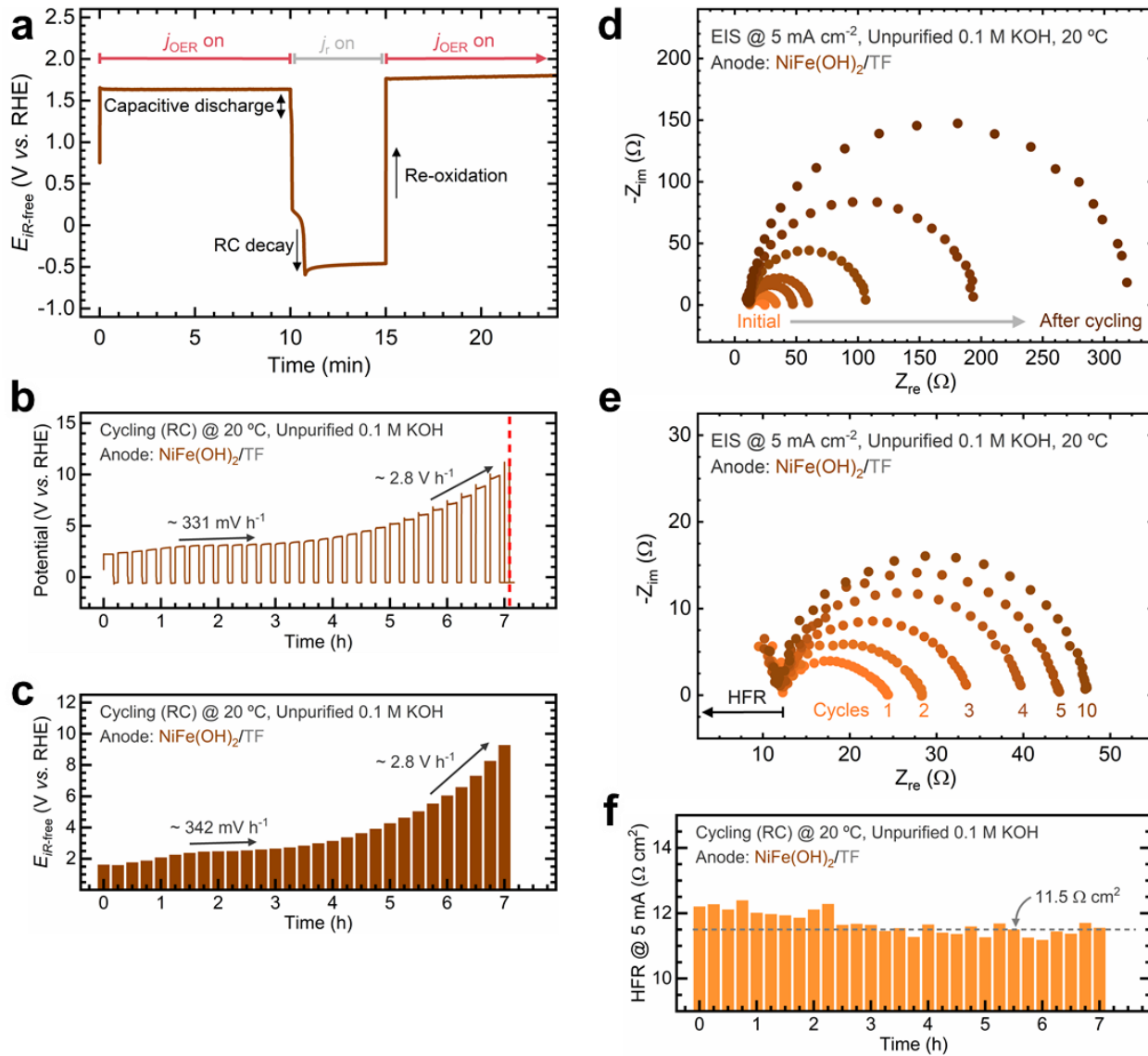


Figure S32. LAWE stability tests under variable operation with a reverse current step on $\text{NiFe(OH)}_2/\text{TF}$ O_2 electrodes: (a) Snapshot of a single cycle, showing the constant current step at $50 \text{ mA}\cdot\text{cm}^{-2}$ followed by a reverse current step of $-5 \text{ mA}\cdot\text{cm}^{-2}$ to simulate shutdown. (b) Electrode potential progression over 30 cycles. (c) iR -corrected electrode potential throughout the stability test, with each bar representing the average potential during the constant current step per cycle. (d) Nyquist plots collected over the stability test. (e) Magnified view of Nyquist plots from the initial cycles. (f) HFR measured from Nyquist plots over the stability test. The arrows in (b) and (c) indicate the potential increase rate during the highlighted intervals. The grey arrow in (d) represents the evolution of the semicircle throughout the stability test, while the black arrow in (e) indicates the HFR value during cycling. The dashed line in (f) represents the average HFR value and serves as a visual guide only. Experimental conditions: unpurified 0.1 M KOH electrolyte at 20 °C.

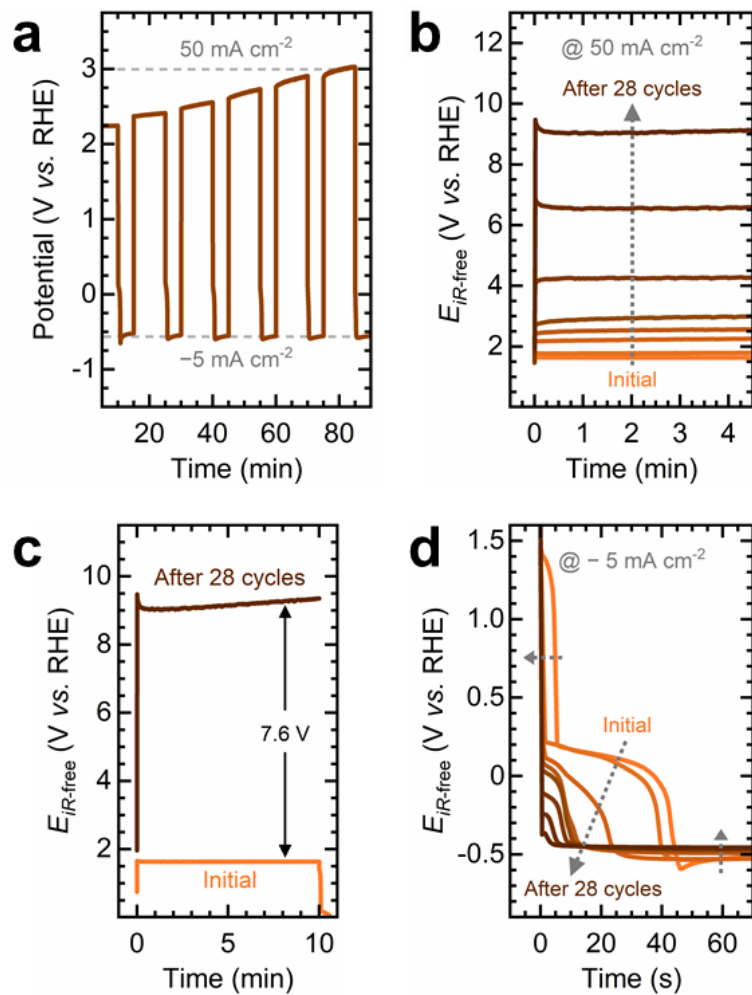


Figure S33. LAWE stability tests under variable operation with a reverse current step on $\text{NiFe}(\text{OH})_2/\text{TF}$ O_2 electrodes: (a) Snapshot of the electrode potential profile under variable operation, highlighting the potential thresholds reached during the constant current and reverse current steps. (b) Comparison of the $i\text{R}$ -corrected electrode potential across cycles. (c) $i\text{R}$ -corrected electrode potential curves at the initial and final constant current steps, highlighting their potential differences. (d) Comparison of the $i\text{R}$ -corrected electrode potential during the reverse current step across cycles. The arrows in (b) and (d) indicate the progression of potential profiles during cycling.

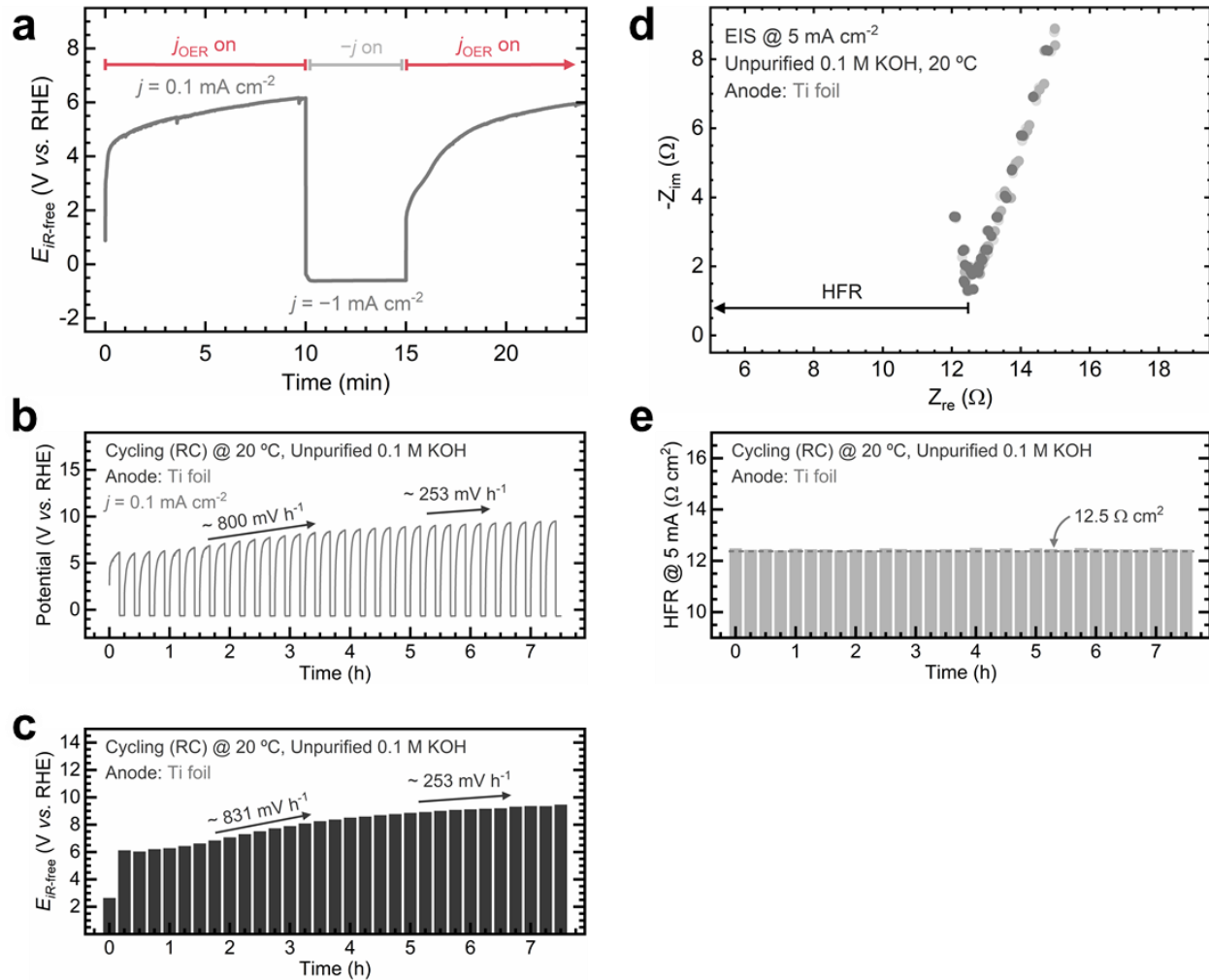


Figure S34. LAWE stability tests under variable operation with a reverse current step on Ti foil acting as an O₂ electrode: (a) Snapshot of a single cycle, showing the constant current step at 0.1 mA·cm⁻² followed by a reverse current step of -1 mA·cm⁻² to simulate shutdown. (b) Electrode potential progression over 30 cycles. (c) *iR*-corrected electrode potential throughout the stability test, with each bar representing the average potential during the constant current step per cycle. (d) Nyquist plots collected over the stability test. (e) HFR measured from Nyquist plots over the stability test. The arrows in (b) and (c) indicate the potential increase rate during the highlighted intervals. The black arrow in (d) indicates the HFR value during cycling. The dashed line in (e) represents the average HFR value and serves as a visual guide only. Experimental conditions: unpurified 0.1 M KOH electrolyte at 20 °C.

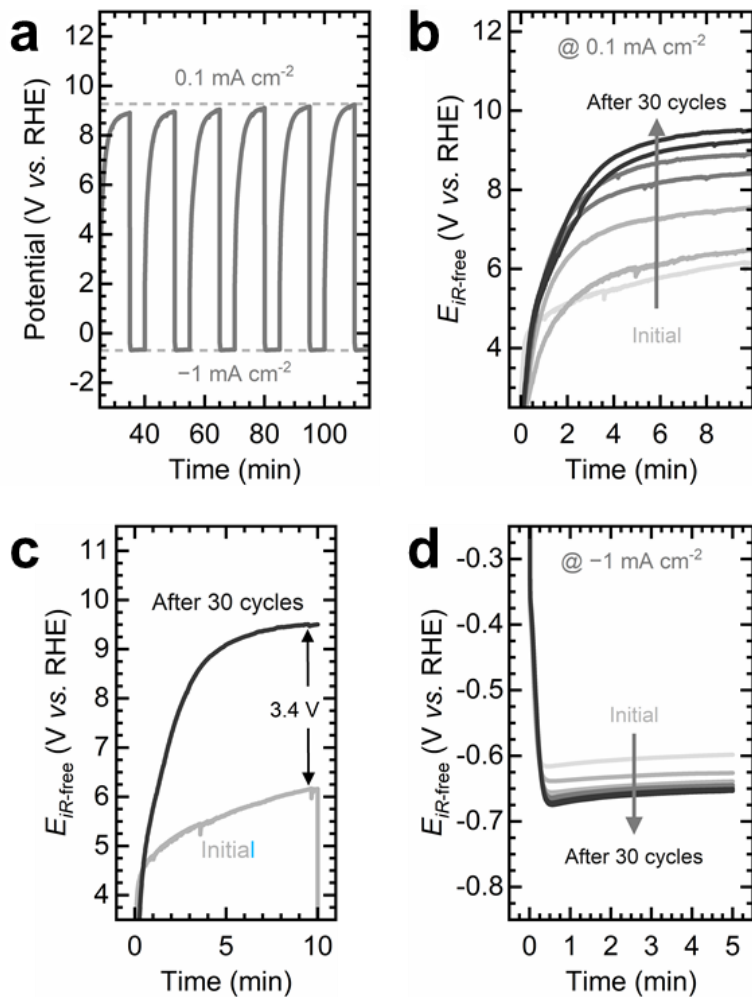


Figure S35. LAWE stability tests under variable operation with a reverse current step on Ti foil acting as an O₂ electrode: (a) Snapshot of the electrode potential profile under variable operation, highlighting the potential thresholds reached during the constant current and reverse current steps. (b) Comparison of the *iR*-corrected electrode potential across cycles. (c) *iR*-corrected electrode potential curves at the initial and final constant current steps, highlighting their potential differences. (d) Comparison of the *iR*-corrected electrode potential during the reverse current step across cycles. The arrows in (b) and (d) indicate the progression of potential profiles during cycling.

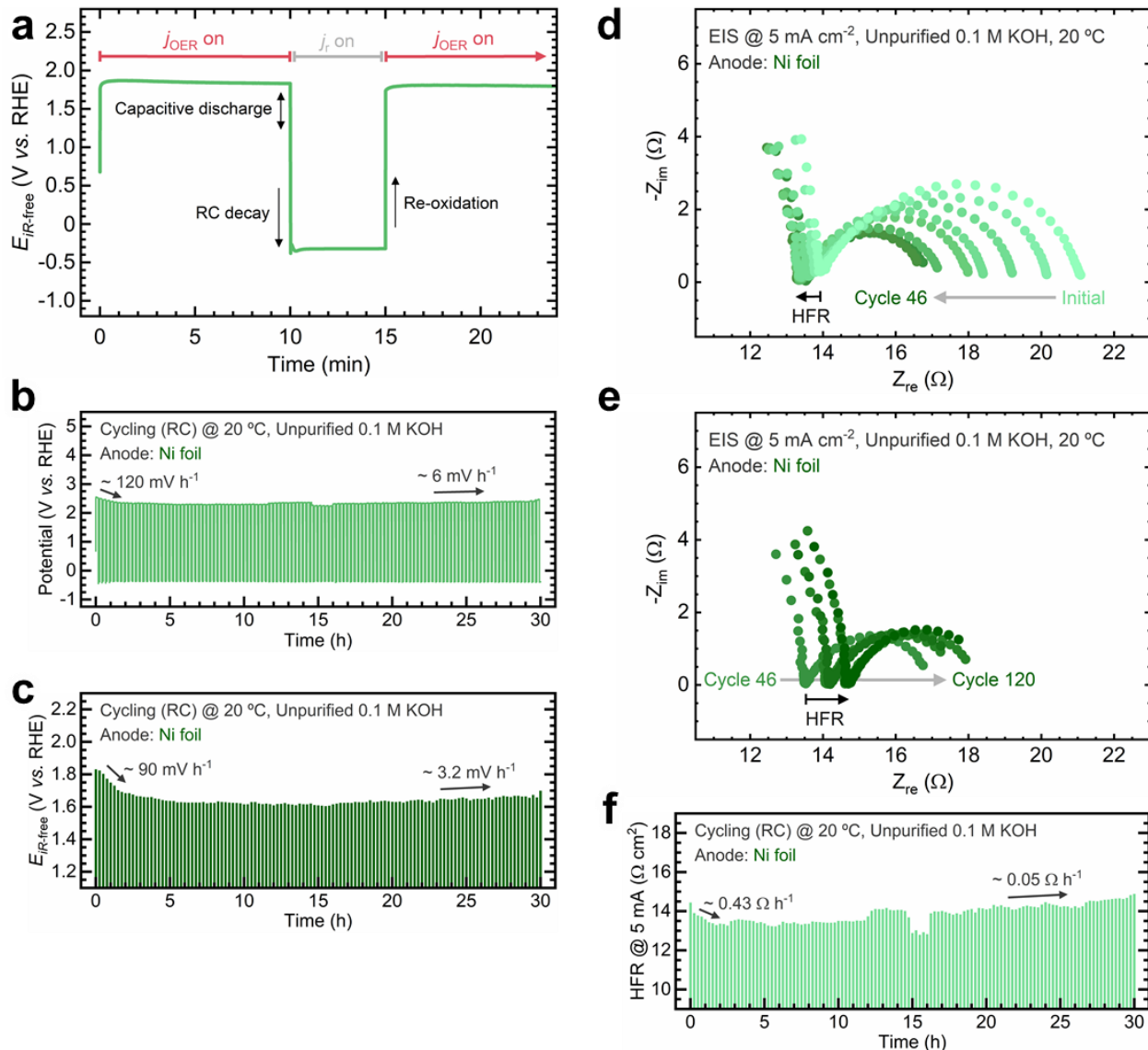


Figure S36. LAWE stability tests under variable operation with a reverse current step on Ni foil acting as an O₂ electrode: (a) Snapshot of a single cycle, showing the constant current step at 50 mA·cm⁻² followed by a reverse current step of -5 mA·cm⁻² to simulate shutdown. (b) Electrode potential progression over 120 cycles. (c) *iR*-corrected electrode potential throughout the stability test, with each bar representing the average potential during the constant current step per cycle. (d) Nyquist plots collected during the initial stabilization period. (e) Nyquist plots collected during the rest of the stability test. (f) HFR measured from Nyquist plots over the stability test. The arrows in (b) and (c) indicate the potential decrease (downwards) or increase (upwards) rate during the highlighted intervals. The grey arrows in (d) and (e) represent the evolution of the semicircle throughout the stability test, while the black arrows indicate the progression of the HFR values during cycling. The arrows in (f) indicate the HFR change rate during the highlighted intervals. Experimental conditions: unpurified 0.1 M KOH electrolyte at 20 °C.

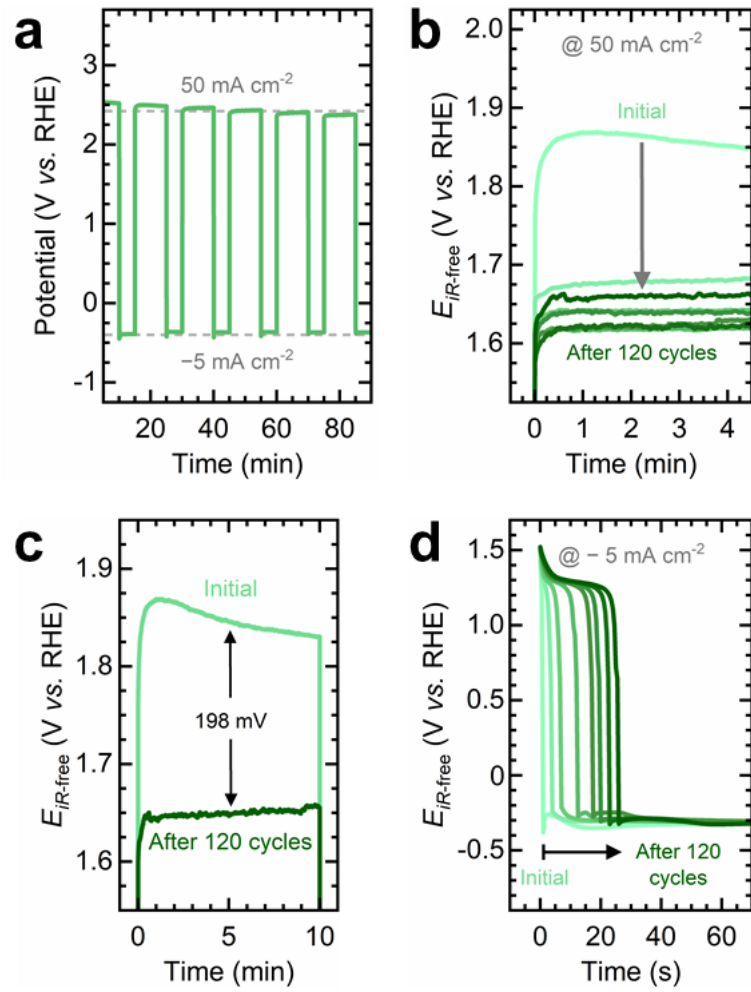


Figure S37. LAWE stability tests under variable operation with a reverse current step on Ni foil acting as an O₂ electrode: (a) Snapshot of the electrode potential profile under variable operation, highlighting the potential thresholds reached during the constant current and reverse current steps. (b) Comparison of the *iR*-corrected electrode potential across cycles. (c) *iR*-corrected electrode potential curves at the initial and final constant current steps, highlighting their potential differences. (d) Comparison of the *iR*-corrected electrode potential during the reverse current step across cycles. The arrows in (b) and (d) indicate the progression of potential profiles during cycling.

Measurement of reverse current effects using in situ SERS

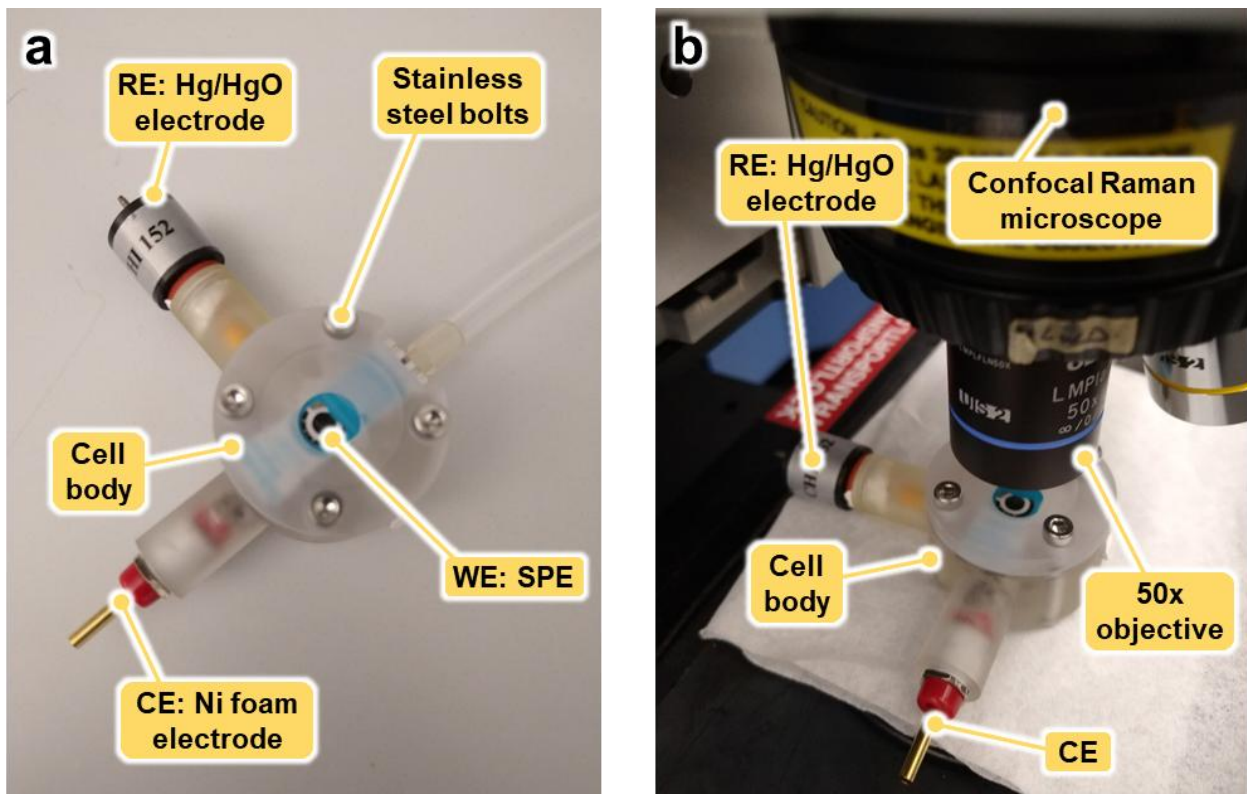


Figure S38. Experimental setup for characterizing electrode discharge during simulated reverse currents using in situ SERS: (a) Photo of the custom electrochemical cell depicting the reference electrode (RE), counter electrode (CE), and the screen-printed electrode (SPE) as the working electrode (WE). (b) View of the experimental configuration showing the electrochemical cell placed below the microscope objective.

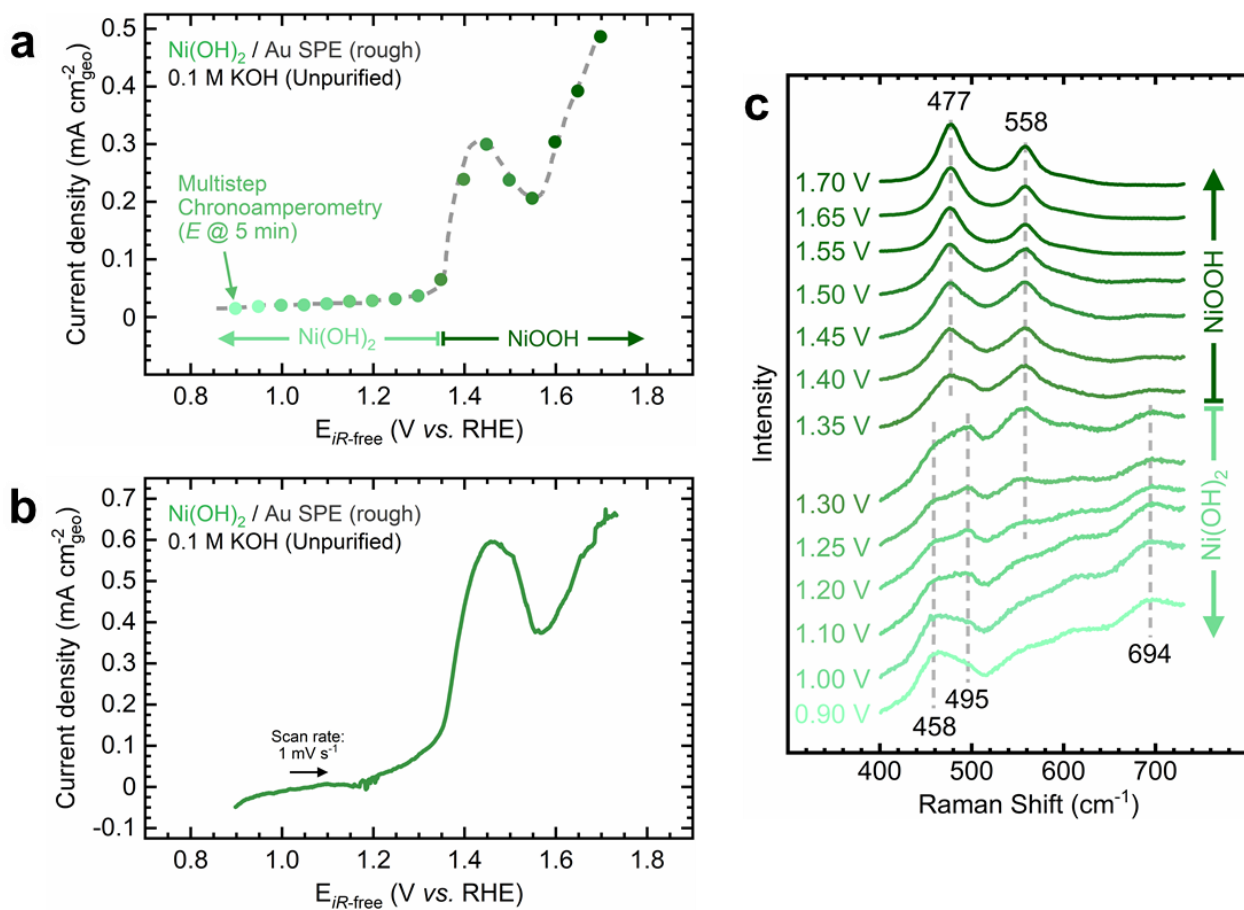


Figure S39. In situ SERS measurements of a Ni(OH)₂ film deposited on a rough Au screen-printed electrode (SPE): (a) Current densities recorded during chronoamperometry (CA) steps at increasing potentials, with each dot representing a 5-min CA test at the corresponding potential. (b) Linear sweep voltammogram at a slow scan rate, demonstrating the relevance of the multistep CA approach for identifying the Ni(OH)₂ to NiOOH transition. (c) Raman spectra collected at each CA step shown in (a). The dashed gray line in (a) serves as a visual guide for the multistep CA tests. Dashed grey lines in (c) serve as visual guides for peak positions of notable Raman bands. Experiments were conducted in unpurified 0.1 M KOH electrolyte at 20 °C.

Supporting note: Multistep chronopotentiometry approximates a steady-state response and captures the hydroxide-to-oxyhydroxide transition. The slow-scan LSV in **Figure S39b** confirms the steady-state condition, as the peak positions closely align. As shown in **Figure S39c**, the characteristic bands of the hydroxide phase evolve into those of the oxyhydroxide phase at 1.35 V vs. RHE, coinciding with the appearance of the M^{2+/3+} redox peak in **Figure S39a**.

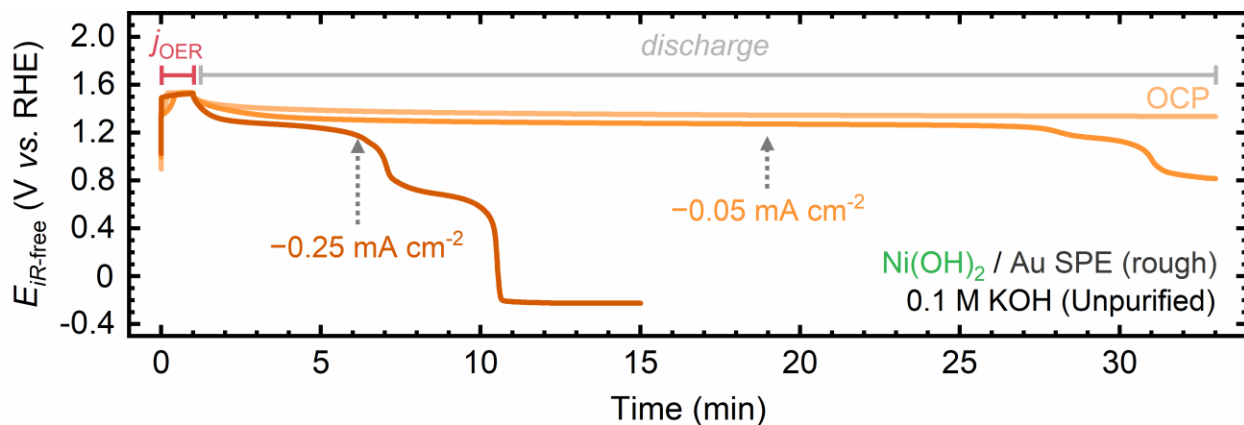


Figure S40. Electrode discharge profiles of $\text{Ni}(\text{OH})_2$ films deposited on rough Au SPEs during simulated shutdown tests under three conditions: open circuit potential and reverse currents of -0.05 and $-0.25 \text{ mA}\cdot\text{cm}^{-2}$. The discharge step was carried out following a constant anodic potential step of 1.5 V vs. RHE. Experiments were conducted in unpurified 0.1 M KOH electrolyte at 20°C .

Supporting note: These supplementary experiments also highlight how the magnitude of the reverse current influences the duration of electrode discharge. More negative current densities accelerate discharge, causing the O_2 electrode to reach more negative potentials quickly. More importantly, faster electrode discharge leads to varying degrees of electrode transformation, as confirmed by our in situ SERS measurements (See Figs. 3, S41, S43, S45-S50). This behavior also depends on factors such as temperature, redox-active site density, surface area, morphology, and electrolyte concentration (see main manuscript for details and references). Importantly, these observations are specific to our experimental conditions and may vary in other setups. Therefore, optimizing discharge parameters and evaluating how different factors influence electrode discharge is essential for each specific case.

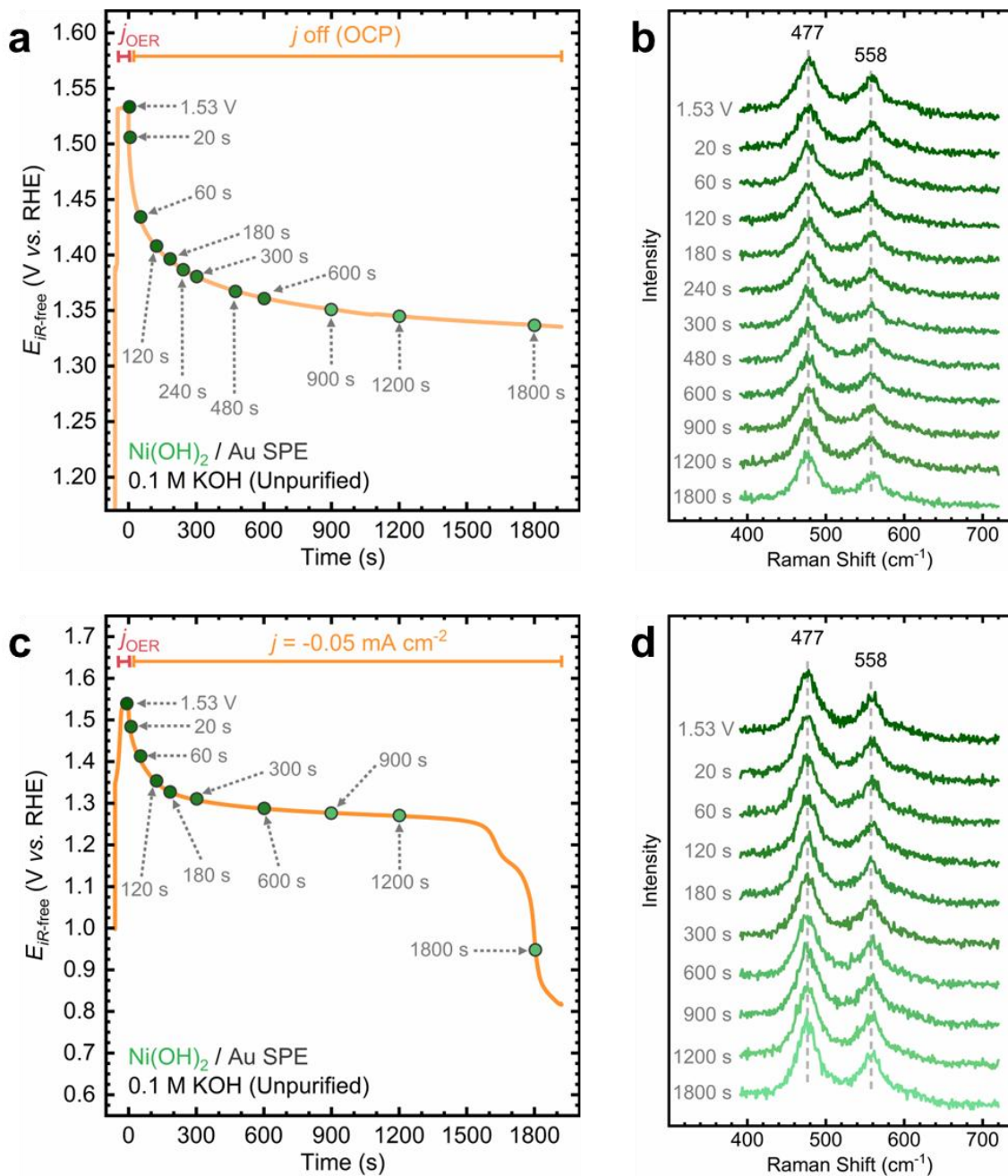


Figure S41. In situ SERS measurements during electrode discharge of $Ni(OH)_2$ films deposited on rough Au SPEs: (a) electrode discharge profile under open circuit condition and (b) corresponding Raman spectra collected at different time points displayed in (a). (c) electrode discharge profile under a reverse current of $-0.05 \text{ mA}\cdot\text{cm}^{-2}$ and (d) corresponding Raman spectra collected at different time points displayed in (c). Dashed grey lines in (b) and (d) serve as visual guides for peak positions of notable Raman bands. Experiments were conducted in unpurified 0.1 M KOH electrolyte at 20°C .

Supporting note: Note that **Fig. S41** demonstrates that open circuit conditions represent relatively "safe" regions for the electrode, as no phase transformations are observed.

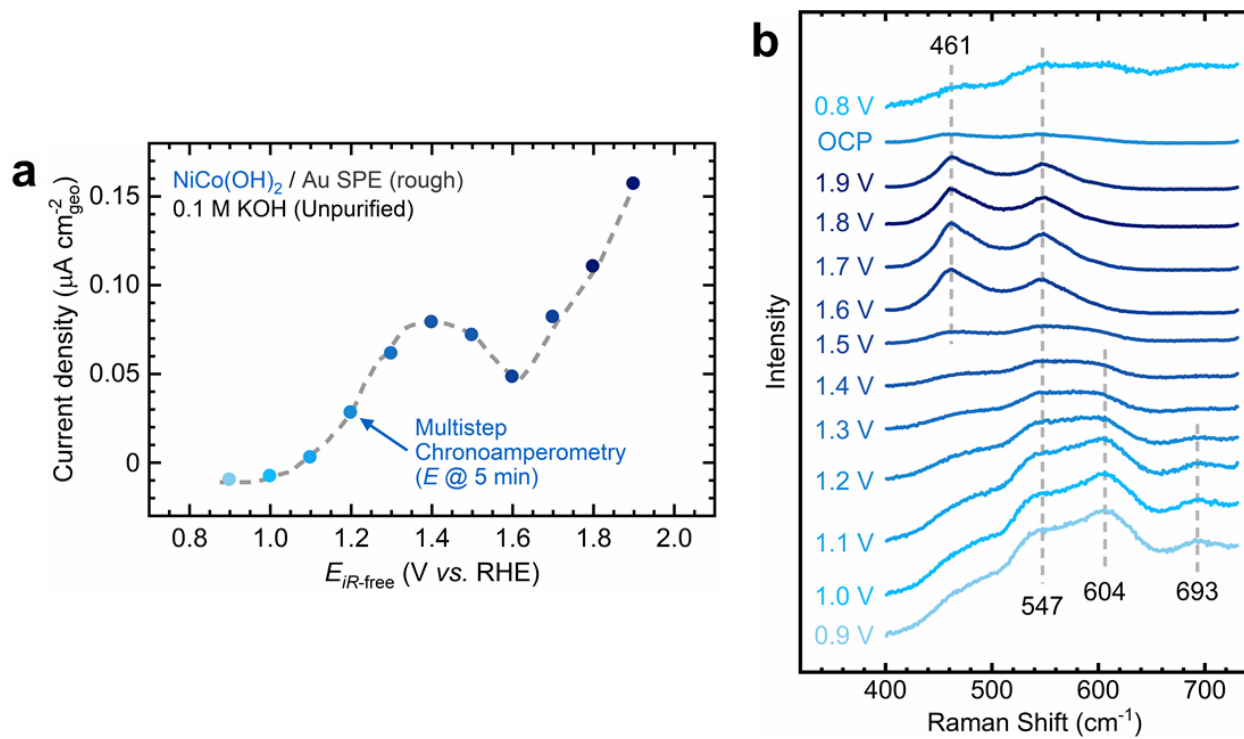


Figure S42. In situ SERS measurements of a NiCo(OH)₂ film deposited on a rough Au SPE: (a) Current densities recorded during chronoamperometry (CA) steps at increasing potentials, with each dot representing a 5-min CA test at the corresponding potential. (b) Corresponding Raman spectra collected at each CA step shown in (a). Dashed grey lines in (b) serve as visual guides for peak positions of notable Raman bands. Experiments were conducted in unpurified 0.1 M KOH electrolyte at 20 °C.

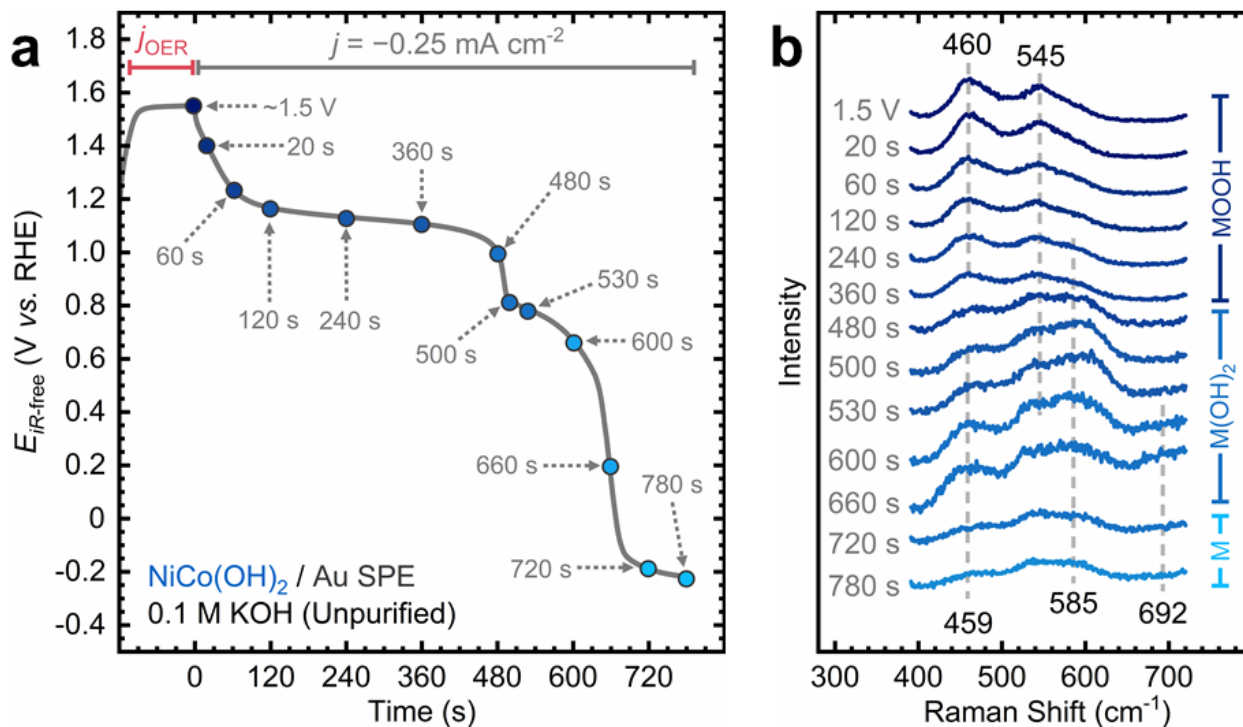


Figure S43. In situ SERS measurements during electrode discharge of a NiCo(OH)₂ film deposited on a rough Au SPE: (a) electrode discharge profile under a reverse current of $-0.25 \text{ mA}\cdot\text{cm}^{-2}$ and (b) corresponding Raman spectra collected at different time points displayed in (a). The discharge step was carried out following a constant anodic potential step of 1.5 V vs. RHE. Dashed grey lines in (b) serve as visual guides for peak positions of notable Raman bands. The corresponding species of the electrode are shown in (b). Experiments were conducted in unpurified 0.1 M KOH electrolyte at 20°C .

Supporting note: Variations in the discharge duration for different catalytic film compositions are attributed to differences in mass loading.

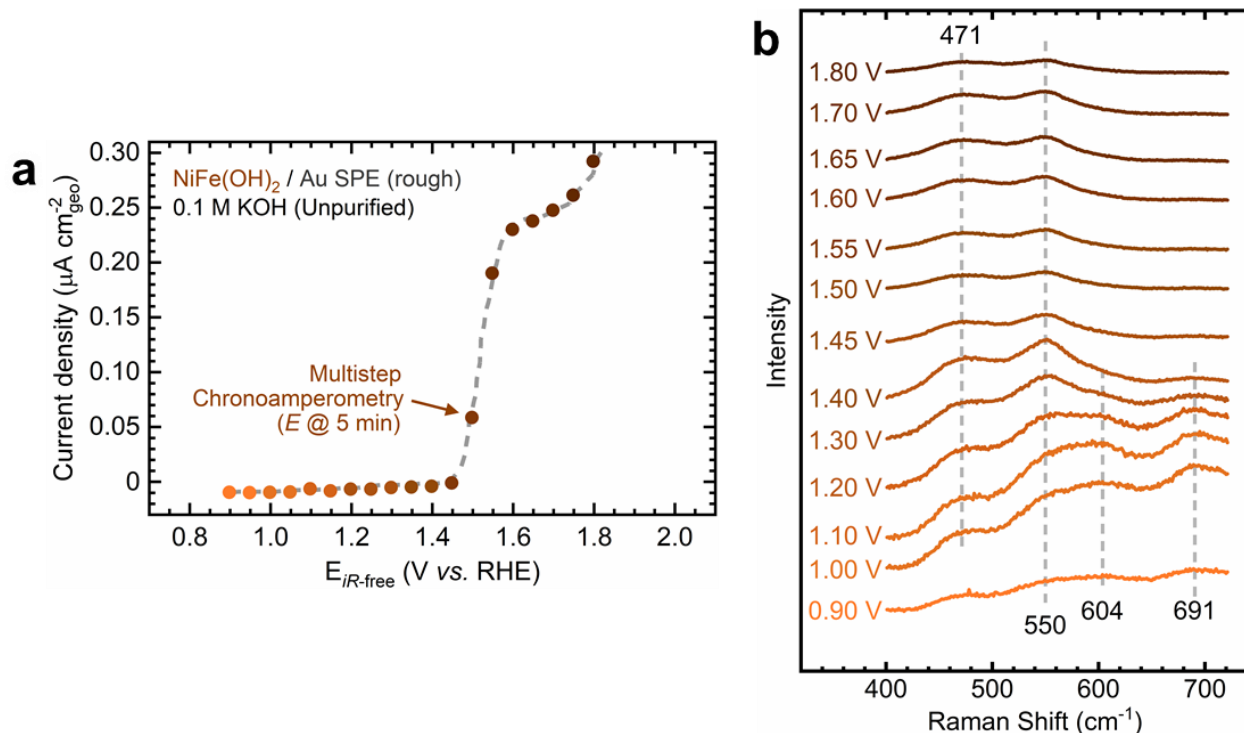


Figure S44. In situ SERS measurements of a NiFe(OH)₂ film deposited on a rough Au SPE: (a) Current densities recorded during chronoamperometry (CA) steps at increasing potentials, with each dot representing a 5-min CA test at the corresponding potential. (b) Corresponding Raman spectra collected at each CA step shown in (a). Dashed grey lines in (b) serve as visual guides for peak positions of notable Raman bands. Experiments were conducted in unpurified 0.1 M KOH electrolyte at 20 °C.

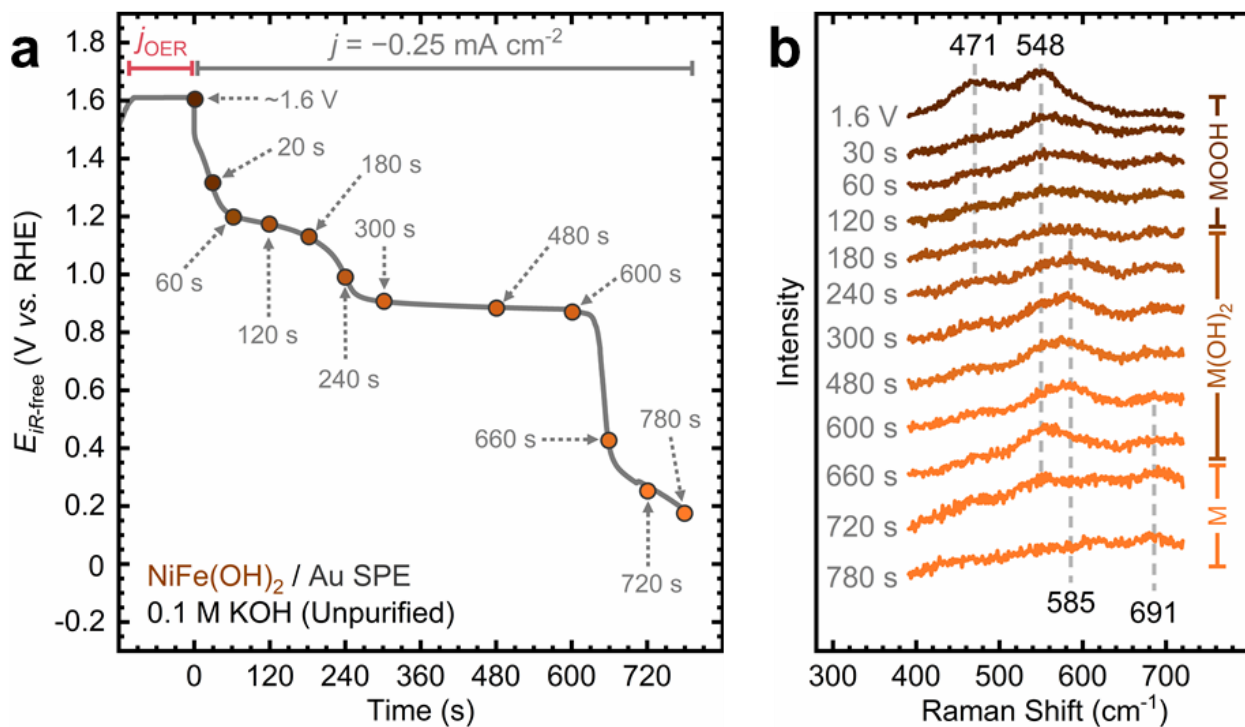


Figure S45. In situ SERS measurements during electrode discharge of a $\text{NiFe}(\text{OH})_2$ film deposited on a rough Au SPE: (a) electrode discharge profile under a reverse current of $-0.25 \text{ mA}\cdot\text{cm}^{-2}$ and (b) corresponding Raman spectra collected at different time points displayed in (a). The discharge step was carried out following a constant anodic potential step of 1.6 V vs. RHE. Dashed grey lines in (b) serve as visual guides for peak positions of notable Raman bands. The corresponding species of the electrode are shown in (b). Experiments were conducted in unpurified 0.1 M KOH electrolyte at 20°C .

Supporting note: Variations in the discharge duration for different catalytic film compositions are attributed to differences in mass loading.

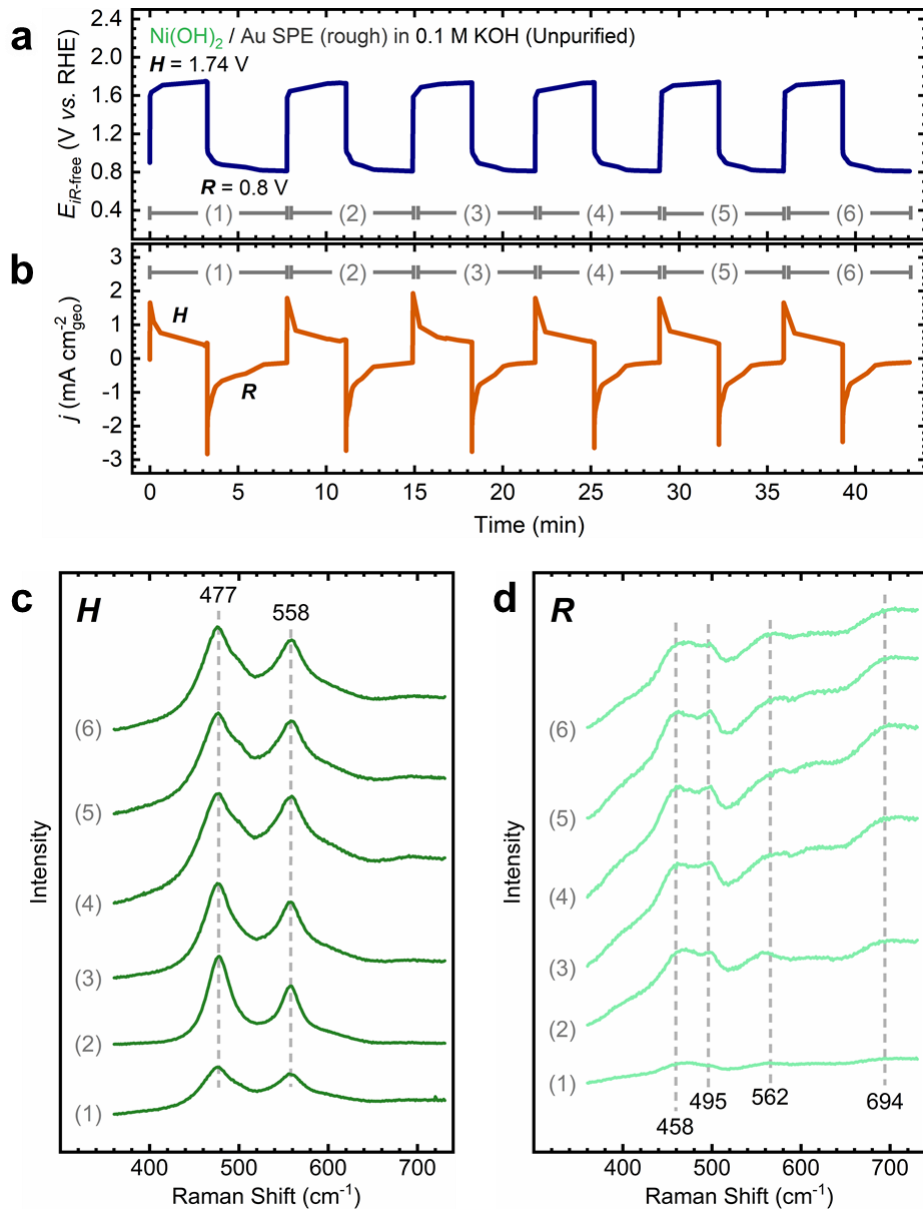


Figure S46. In situ SERS measurements during variable operation of a Ni(OH)_2 film deposited on a rough Au SPE: (a) Electrode potential and (b) current density profiles during cycling, where H represents the anodic hold step at a constant potential of 1.74 V vs. RHE, and R denotes the reverse step at 0.8 V vs. RHE. The numbered segments indicate the cycle count, each consisting of one H and one R step. Corresponding Raman spectra collected at each cycle for the (c) potential hold H step and (d) reverse R step. Dashed grey lines in (c) and (d) serve as visual guides for notable Raman band positions. Experiments were conducted in unpurified 0.1 M KOH at 20 °C.

Supporting Note: In situ SERS measurements during variable operation were conducted under potentiostatic control for both the H and R steps. The potential in **Fig. S46a** fluctuates due to iR compensation (**Eq. 3**) as current changes during discharge. Potentiostatic control was chosen to ensure that electrode discharge remained within OCP limits.

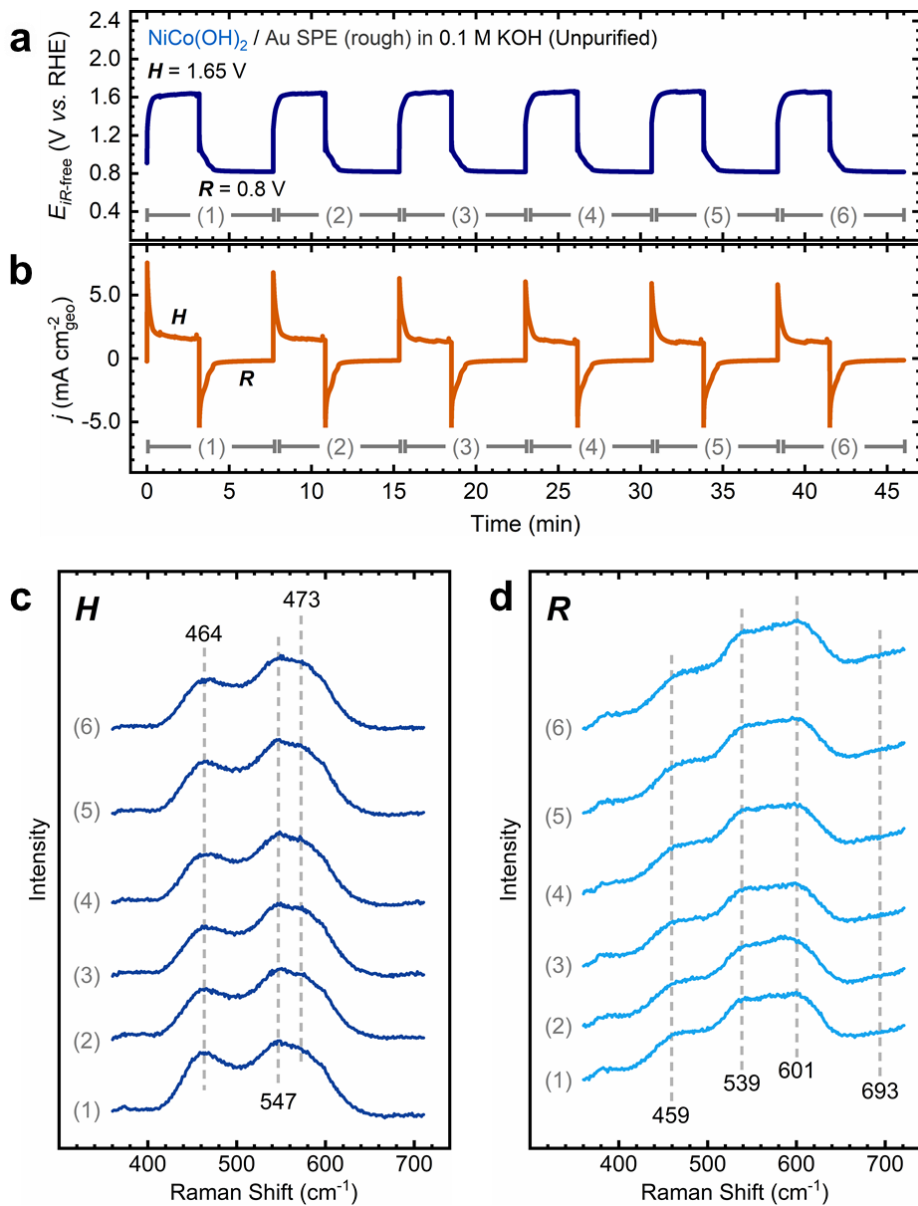


Figure S47. In situ SERS measurements during variable operation of a $\text{NiCo}(\text{OH})_2$ film deposited on a rough Au SPE: (a) Electrode potential and (b) current density profiles during cycling, where H represents the anodic hold step at a constant potential of 1.65 V vs. RHE, and R denotes the reverse step at 0.8 V vs. RHE. The numbered segments indicate the cycle count, each consisting of one H and one R step. Corresponding Raman spectra collected at each cycle for the (c) potential hold H step and (d) reverse R step. Dashed grey lines in (c) and (d) serve as visual guides for notable Raman band positions. Experiments were conducted in unpurified 0.1 M KOH at 20 °C.

Supporting Note: In situ SERS tests during variable operation were conducted under potentiostatic control to remain within OCP limits. The electrode potential fluctuates due to iR compensation as current varies during discharge. The anodic potential differs slightly from that observed for $\text{Ni}(\text{OH})_2$ (Fig. S46) because $\text{NiCo}(\text{OH})_2$ exhibits higher OER activity.

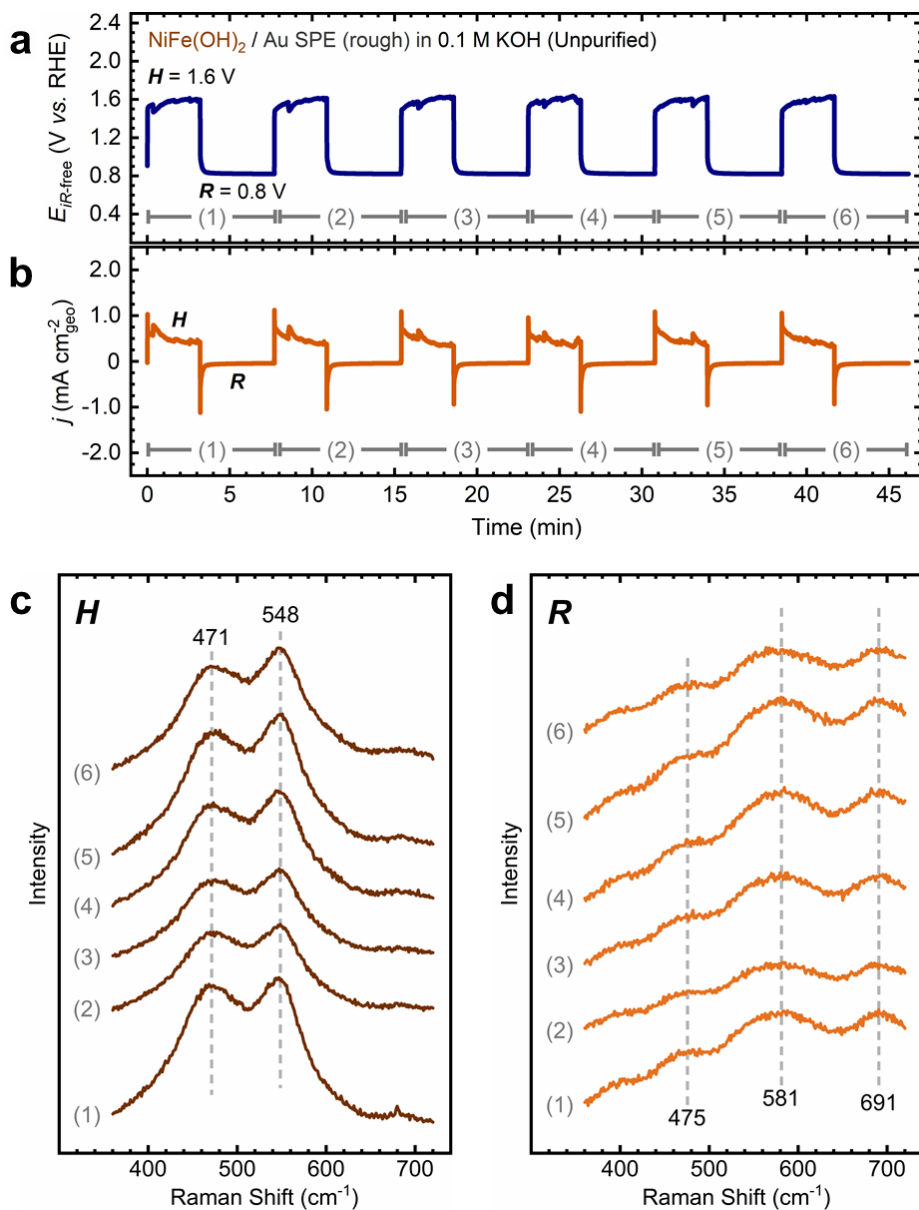


Figure S48. In situ SERS measurements during variable operation of a NiFe(OH)_2 film deposited on a rough Au SPE: (a) Electrode potential and (b) current density profiles during cycling, where H represents the anodic hold step at a constant potential of 1.6 V vs. RHE, and R denotes the reverse step at 0.8 V vs. RHE. The numbered segments indicate the cycle count, each consisting of one H and one R step. Corresponding Raman spectra collected at each cycle for the (c) potential hold H step and (d) reverse R step. Dashed grey lines in (c) and (d) serve as visual guides for notable Raman band positions. Experiments were conducted in unpurified 0.1 M KOH at 20 °C.

Supporting Note: In situ SERS tests during variable operation were conducted under potentiostatic control to remain within OCP limits. The electrode potential fluctuates due to iR compensation as current varies during discharge. The anodic potential differs slightly from that observed for Ni(OH)_2 (Fig. S46) because NiFe(OH)_2 exhibits higher OER activity.

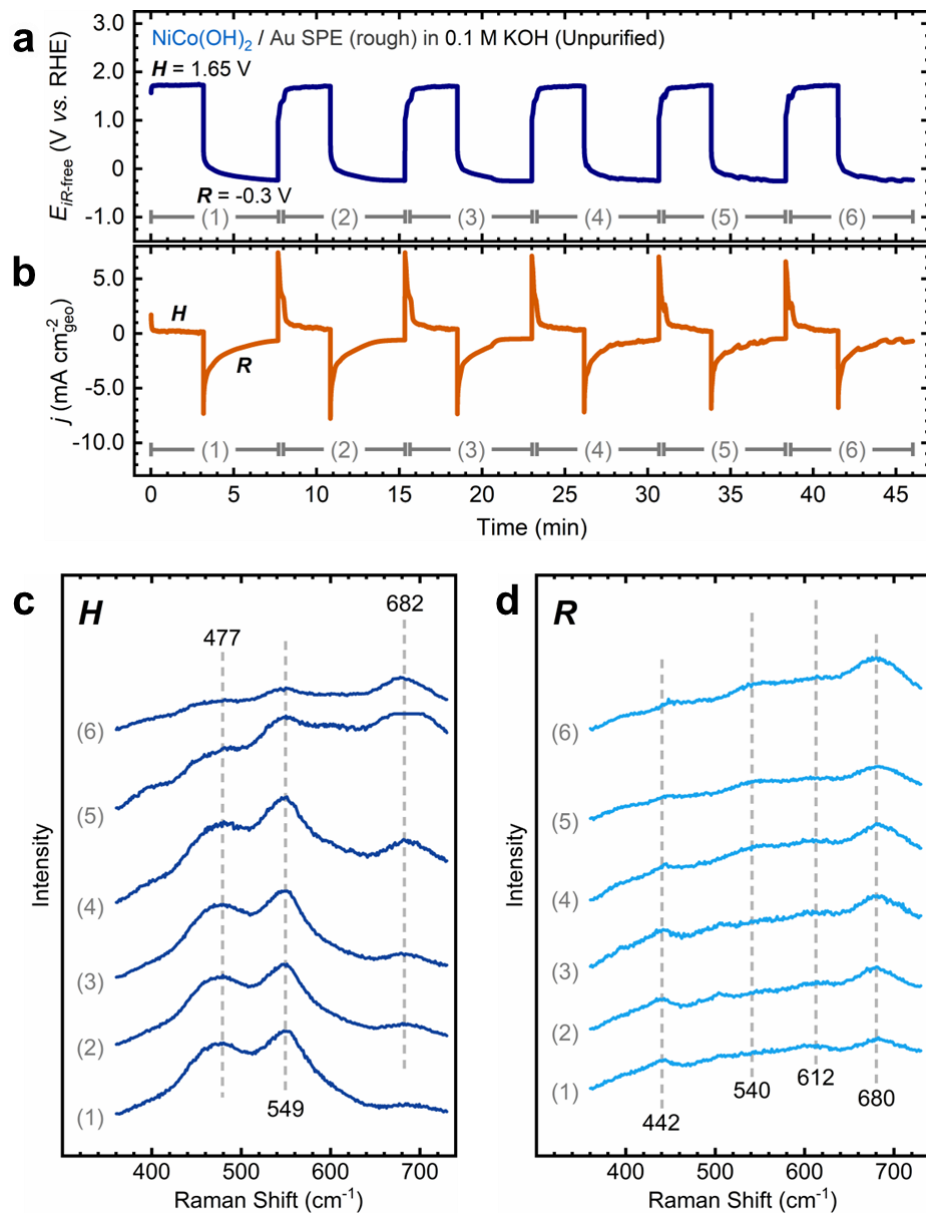


Figure S49. In situ SERS measurements during variable operation of a $\text{NiCo}(\text{OH})_2$ film deposited on a rough Au SPE: (a) Electrode potential and (b) current density profiles during cycling, where H represents the anodic hold step at a constant potential of 1.65 V vs. RHE, and R denotes the reverse step at -0.3 V vs. RHE. The numbered segments indicate the cycle count, each consisting of one H and one R step. Corresponding Raman spectra collected at each cycle for the (c) potential hold H step and (d) reverse R step. Dashed grey lines in (c) and (d) serve as visual guides for notable Raman band positions. Experiments were conducted in unpurified 0.1 M KOH at 20 °C.

Supporting Note: In situ SERS tests during variable operation were conducted under potentiostatic control to achieve a similar cathodic potential during the reverse step. The electrode potential fluctuates due to iR compensation as current varies during discharge.

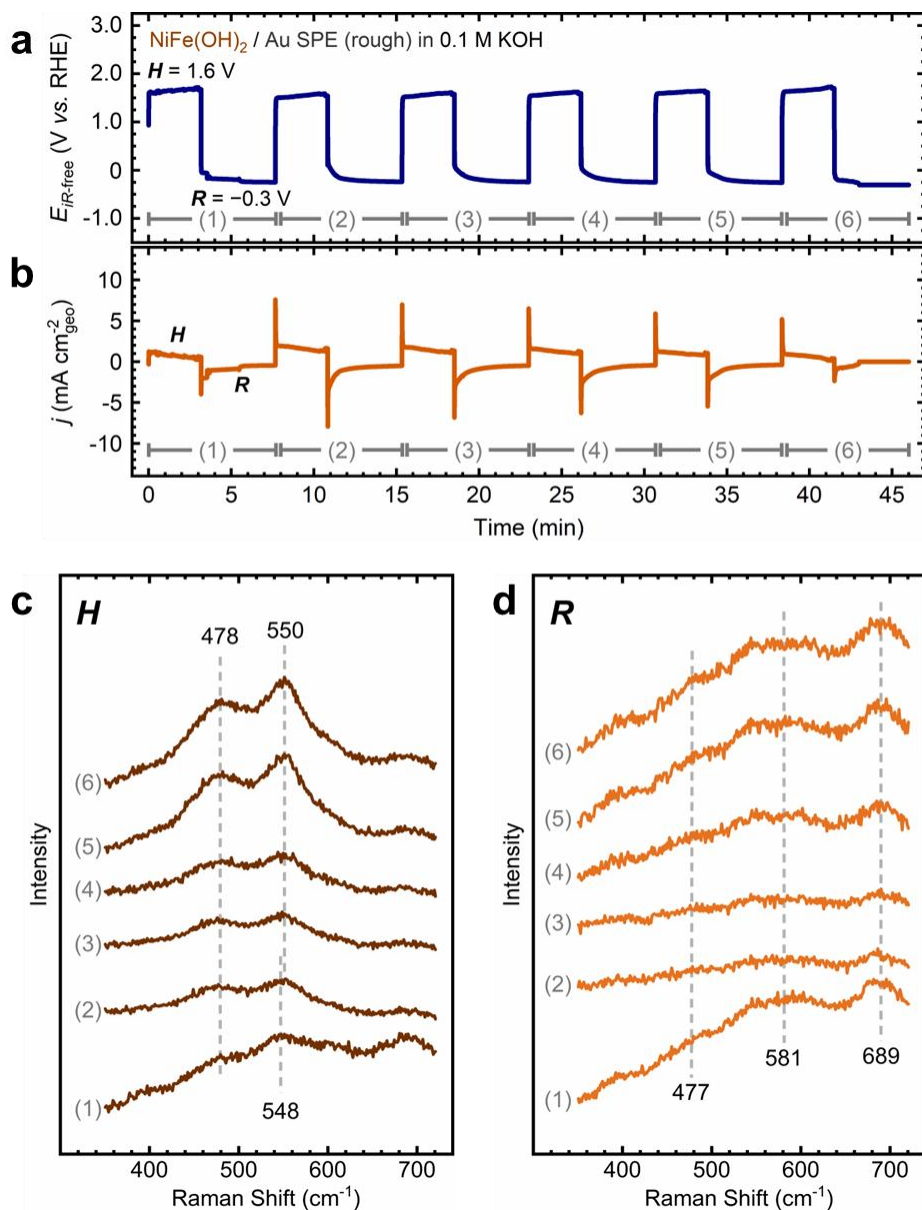


Figure S50. In situ SERS measurements during variable operation of a NiFe(OH)_2 film deposited on a rough Au SPE: (a) Electrode potential and (b) current density profiles during cycling, where H represents the anodic hold step at a constant potential of 1.6 V vs. RHE, and R denotes the reverse step at -0.3 V vs. RHE. The numbered segments indicate the cycle count, each consisting of one H and one R step. Corresponding Raman spectra collected at each cycle for the (c) potential hold H step and (d) reverse R step. Dashed grey lines in (c) and (d) serve as visual guides for notable Raman band positions. Experiments were conducted in unpurified 0.1 M KOH at 20 °C.

Supporting Note: In situ SERS tests during variable operation were conducted under potentiostatic control to achieve a similar cathodic potential during the reverse step. The electrode potential fluctuates due to iR compensation as current varies during discharge.

Chemical composition analysis via ToF-SIMS

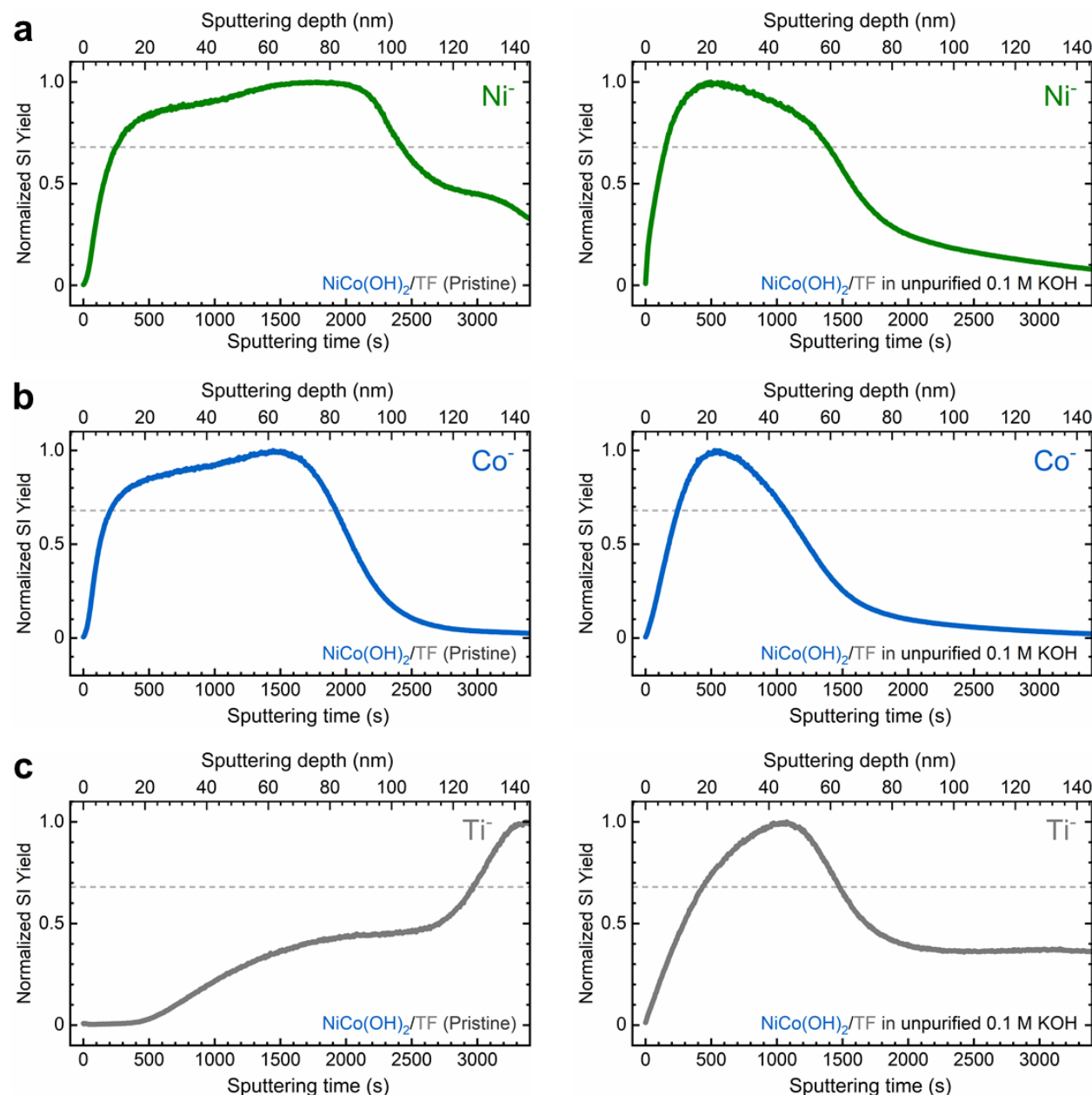


Figure S51. TOF-SIMS secondary-ion yield normalized to the maximum for (a) Ni⁻, (b) Co⁻, and (c) Ti⁻ fragments before (left) and after (right) variable operation tests of NiCo(OH)₂/TF electrodes. Data were collected in negative ion mode. Dashed grey lines indicate the 68.27% confidence interval ($\mu \pm 1\sigma$) for a normal distribution. Variable operation experiments were conducted in unpurified 0.1 M KOH at 20 °C. The electrochemical responses of these experiments are shown in Fig. S30.

Supporting Note: The dashed line in Fig. S51 establishes a range where nominally 68.27% of the secondary ion fragment's total concentration is found within the depth profile.

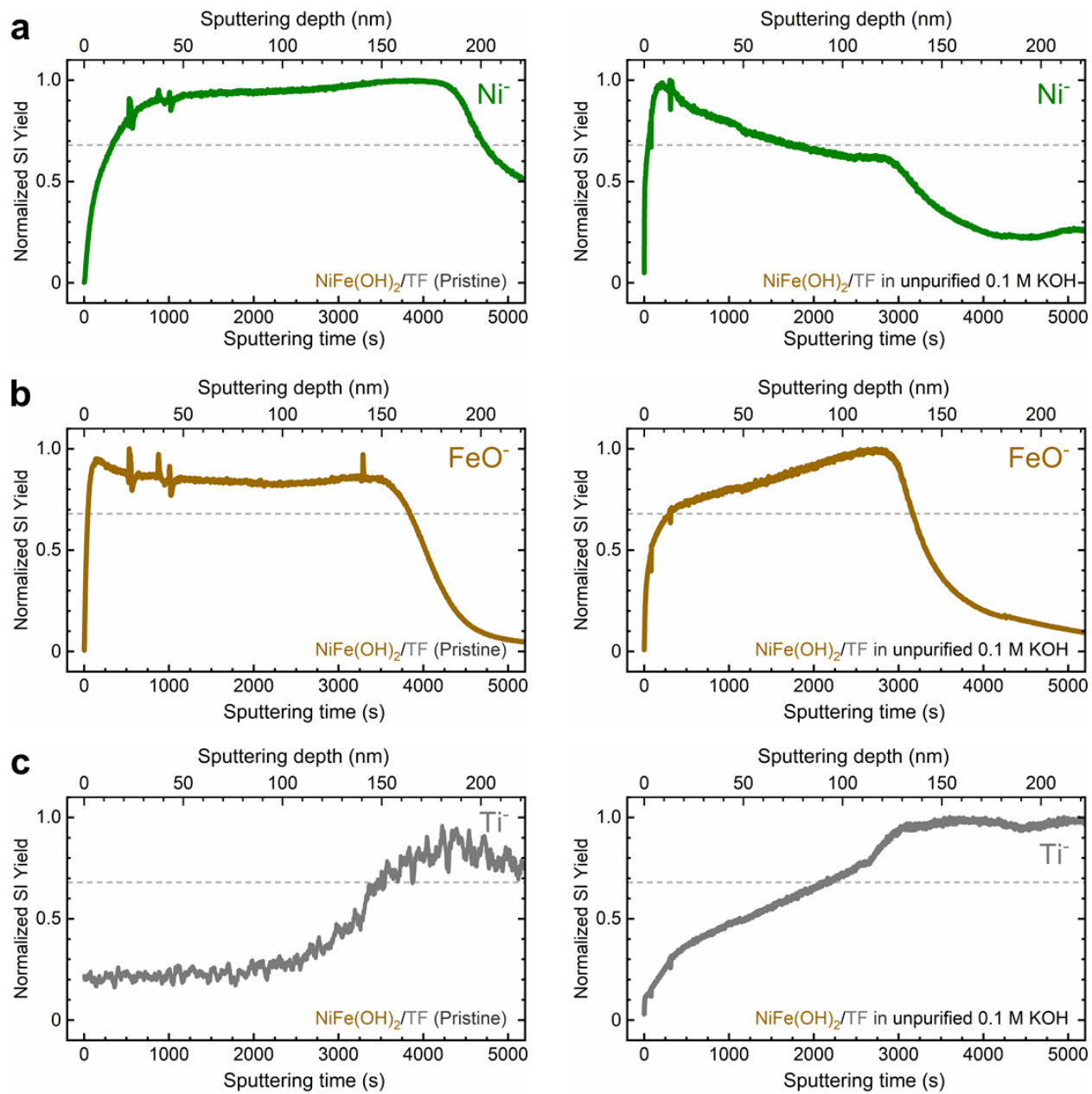


Figure S52. TOF-SIMS secondary-ion yield normalized to the maximum for (a) Ni⁻, (b) FeO⁻, and (c) Ti⁻ fragments before (left) and after (right) variable operation tests of NiFe(OH)₂/TF electrodes. Data were collected in negative ion mode. Dashed grey lines indicate the 68.27% confidence interval ($\mu \pm 1\sigma$) for a normal distribution. Variable operation experiments were conducted in unpurified 0.1 M KOH at 20 °C. The electrochemical responses of these experiments are shown in Fig. S32.

Supporting Note: The dashed line in Fig. S52 establishes a range where nominally 68.27% of the secondary ion fragment's total concentration is found within the depth profile.

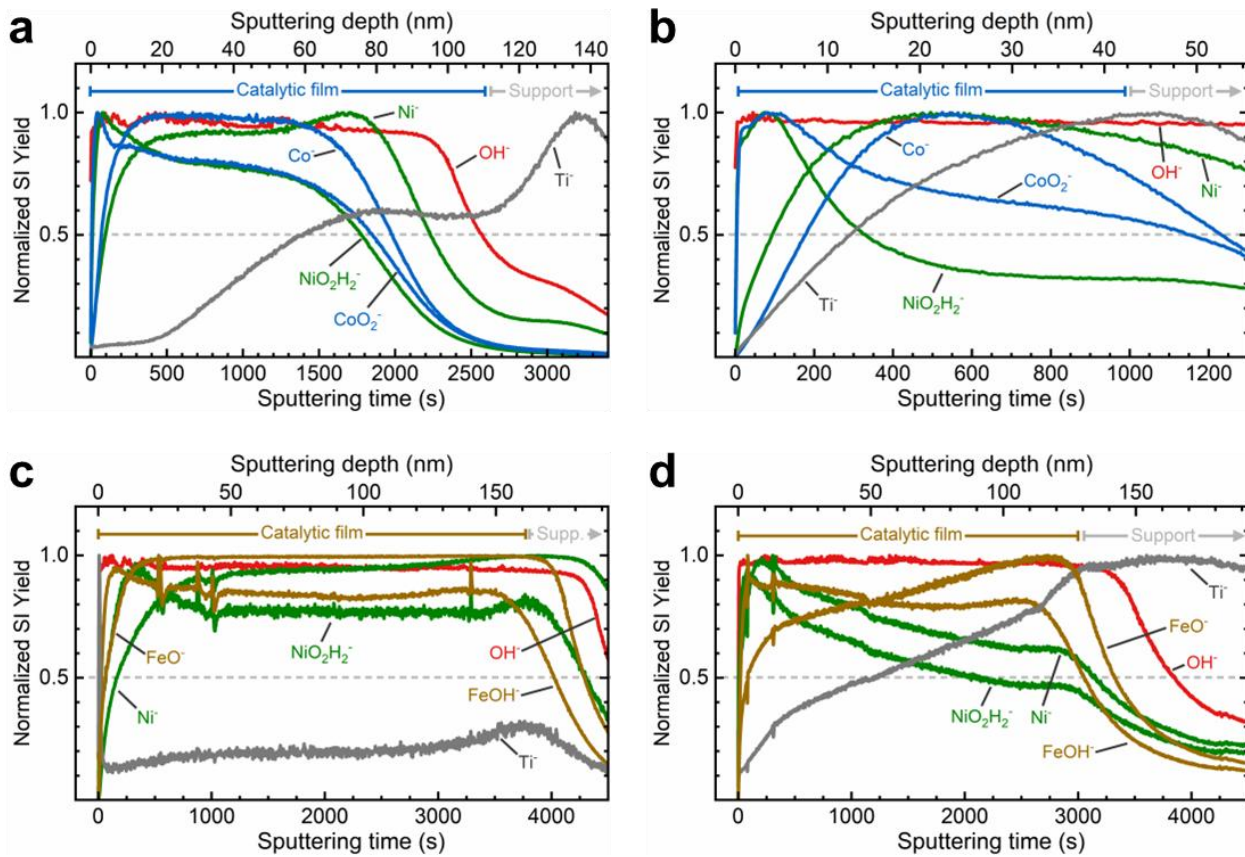


Figure S53. TOF-SIMS depth profiles of various secondary ion fragments for NiCo(OH)₂/TF electrodes (a) before and (b) after variable operation tests. Depth profiles of NiFe(OH)₂/TF electrodes (c) before and (d) after tests. The apparent distribution of the catalytic films and the Ti support are shown as reference. Depth profiles were obtained in negative ion mode and are normalized to maximum. Dashed grey lines at 0.5 serve as visual guides only. Variable operation experiments were conducted in unpurified 0.1 M KOH at 20 °C. The electrochemical responses of these experiments are shown in **Fig. S30** for NiCo(OH)₂/TF and **Fig. S32** for NiFe(OH)₂/TF.

Supporting Note: The sputtering depths in **Figs. S51-S53** were calculated based on the sputtering rate of $0.043 \pm 0.01 \text{ nm}\cdot\text{s}^{-1}$, determined under negative polarity. All calculations for statistical analysis were conducted using the sputtering time only. The displayed sputtering depth serves merely as a point of reference.

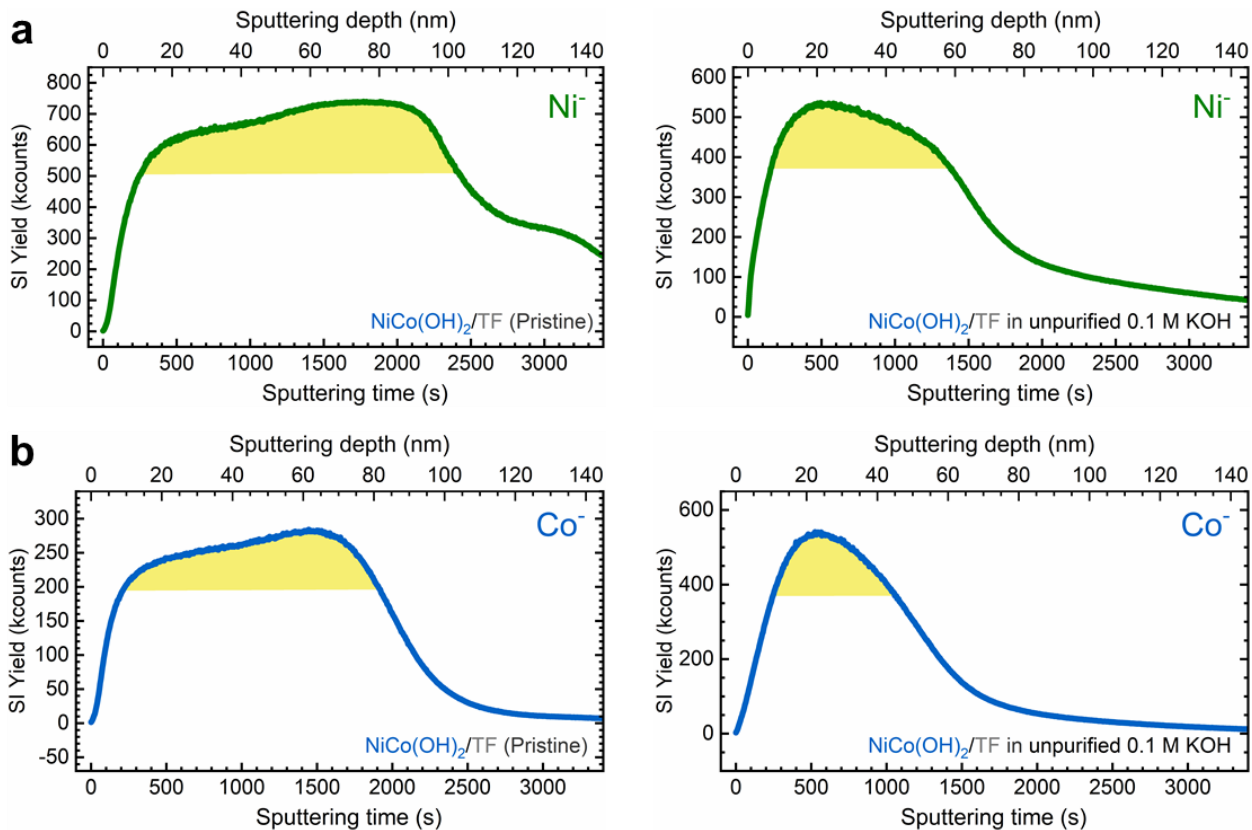


Figure S54. TOF-SIMS secondary-ion yields for (a) Ni^- and (b) Co^- fragments before (left) and after (right) variable operation tests of $\text{NiCo(OH)}_2/\text{TF}$ electrodes. Data were collected in negative ion mode. The yellow area represents the integrated yield within the 68.27% confidence interval ($\mu \pm 1\sigma$) for a normal distribution. Variable operation experiments were conducted in unpurified 0.1 M KOH at 20 °C. The electrochemical responses of these experiments are shown in **Fig. S30**.

Supporting Note: The yellow area in **Fig. S54** represents the depth range containing approximately 68.27% of the total secondary ion fragment concentration. This region is used as a reference to compare mass loss after variable operation tests.

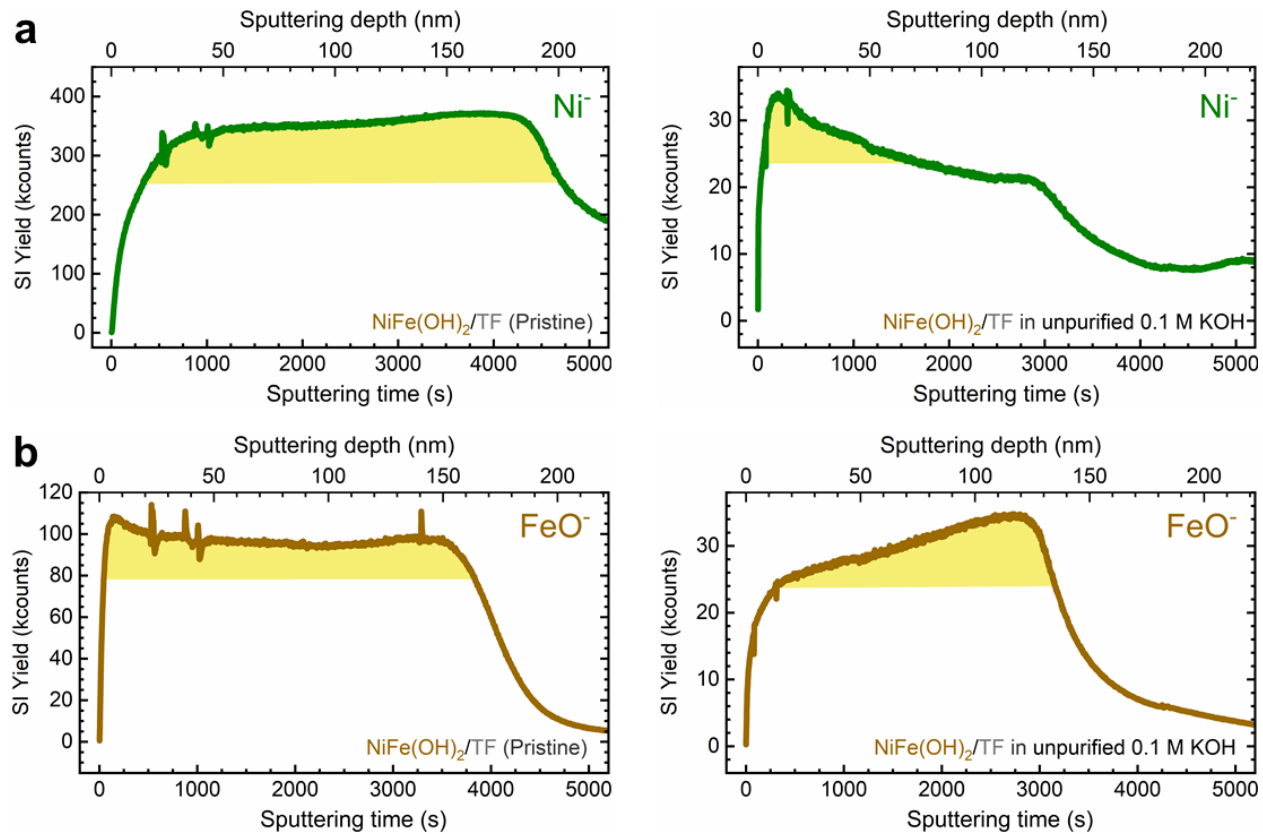


Figure S55. TOF-SIMS secondary-ion yields for (a) Ni^- and (b) FeO^- fragments before (left) and after (right) variable operation tests of $\text{NiFe(OH)}_2/\text{TF}$ electrodes. Data were collected in negative ion mode. The yellow area represents the integrated yield within the 68.27% confidence interval ($\mu \pm 1\sigma$) for a normal distribution. Variable operation experiments were conducted in unpurified 0.1 M KOH at 20 °C. The electrochemical responses of these experiments are shown in **Fig. S32**.

Supporting Note: The yellow area in **Fig. S55** represents the depth range containing approximately 68.27% of the total secondary ion fragment concentration. This region is used as a reference to compare mass loss after variable operation tests.

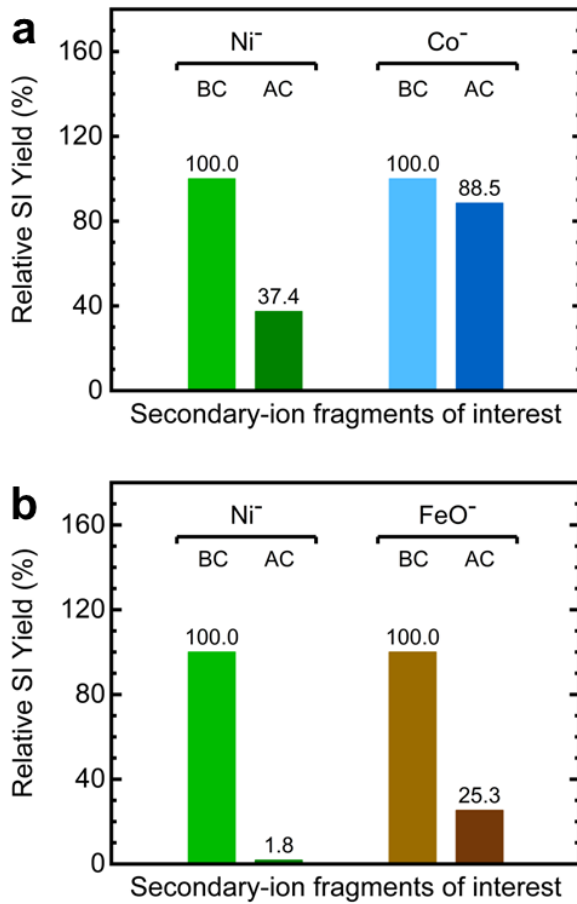


Figure S56. Relative secondary-ion yields for selected fragments from TOF-SIMS measurements of (a) $\text{NiCo}(\text{OH})_2/\text{TF}$ and (b) $\text{NiFe}(\text{OH})_2/\text{TF}$ electrodes before (BC) and after (AC) variable operation tests. The bars represent the integrated yields within the 68.27% confidence interval ($\mu \pm 1\sigma$) shown in Figs. S54 and S55.

Supporting Note: In Fig. S56, the values above each bar indicate the relative percentage of the yield, with the total integrated yield for the pristine (BC) electrode defined as 100%. Thus, the percentages for the electrodes after variable operation testing (AC) represent the mass fraction of each fragment that remains within the defined confidence interval. For example, for the $\text{NiCo}(\text{OH})_2/\text{TF}$ electrode, 37.4% of the initial yield of Ni remains after testing, indicating a loss of 62.6%.

Although the TOF-SIMS integrated secondary-ion yield analysis involves different electrode samples, which may vary in mass loading, the substantial decrease in integrated yields for Ni, Co, and Fe offers an initial estimate of mass loss due to variable operation. We highlight that the extent of loss differs between metals within the same film and between NiCo and NiFe electrodes, indicating that mass loss is not uniform across samples.

In-plane conductivity measurements using IDA electrodes

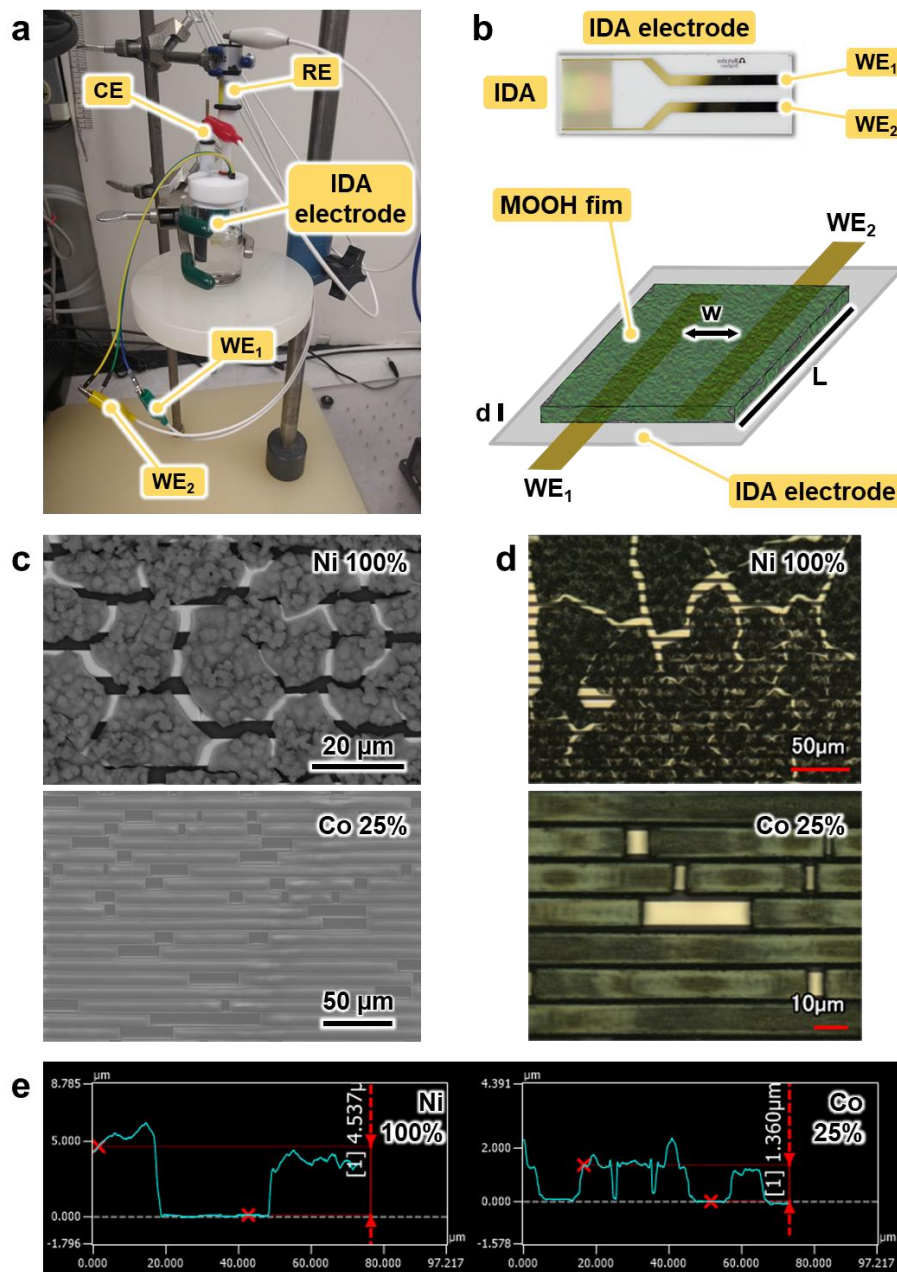


Figure S57. Characterization of interdigitated array (IDA) electrodes for in situ electrical conductivity measurements: (a) Photo of the electrochemical setup, (b) schematic of the IDA electrodes with an expanded view of the deposited MOOH film bridging two working electrodes, where w is the gap spacing (4 μm), d is the film thickness, and L is the electrode length (6.6 mm). (c) SEM and (d) non-contact profilometry (NCP) images of MOOH films on IDA electrodes. (e) MOOH film thickness measurements via NCP (in μm).

Supporting Note: Despite cracking, continuous regions of the film span the gap spaces and allow for measurement of the in-plane effective conductivity, as reported previously.^{2,4}

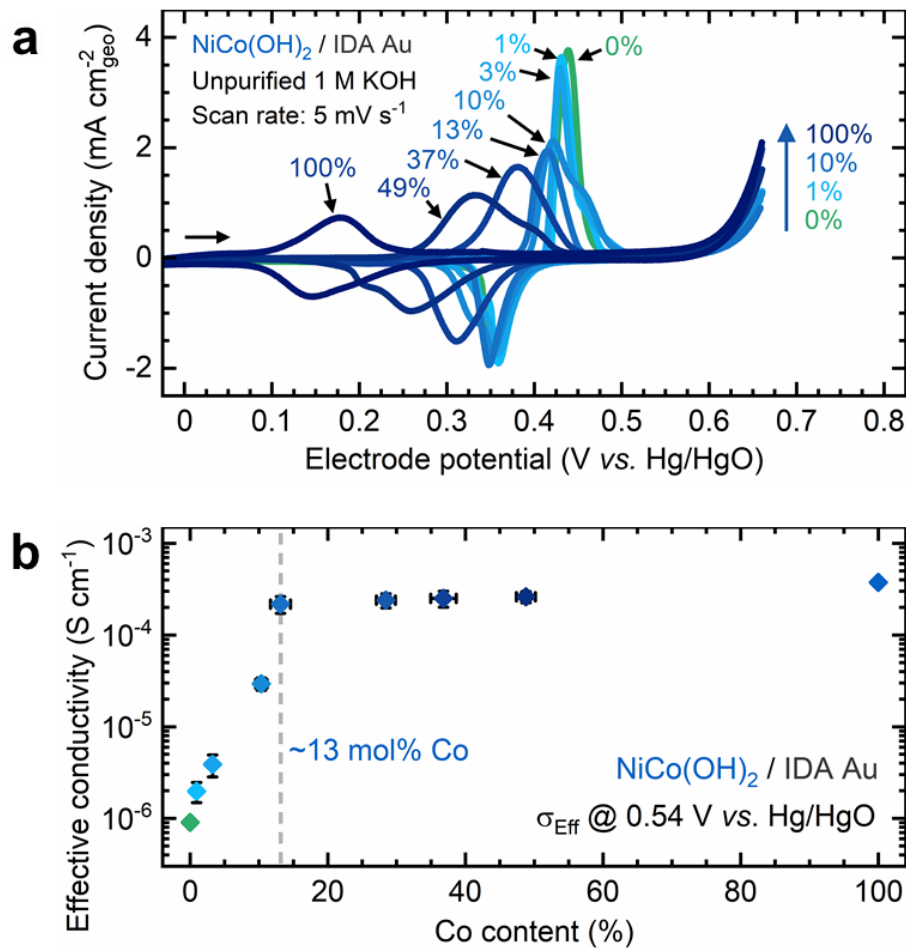


Figure S58. In situ electrical conductivity of NiCo(OH)₂ films as a function of Co content: (a) Cyclic voltammetry scans of NiCo(OH)₂ films deposited on IDA electrodes at increasing Co contents. Electrode potentials are not corrected for series resistance, and current densities are not normalized for differences in film thickness. (b) In-plane effective conductivity (measured at 0.54 V vs. Hg/HgO) as a function of Co content (in mol%). The vertical dashed line indicates the Co content (13%) at which the effective conductivity plateaus. Uncertainty bars represent the standard deviation from three replicate measurements. Experiments were carried out in unpurified 1 M KOH electrolyte at 20 °C.

Metal dissolution analysis via ICP-MS

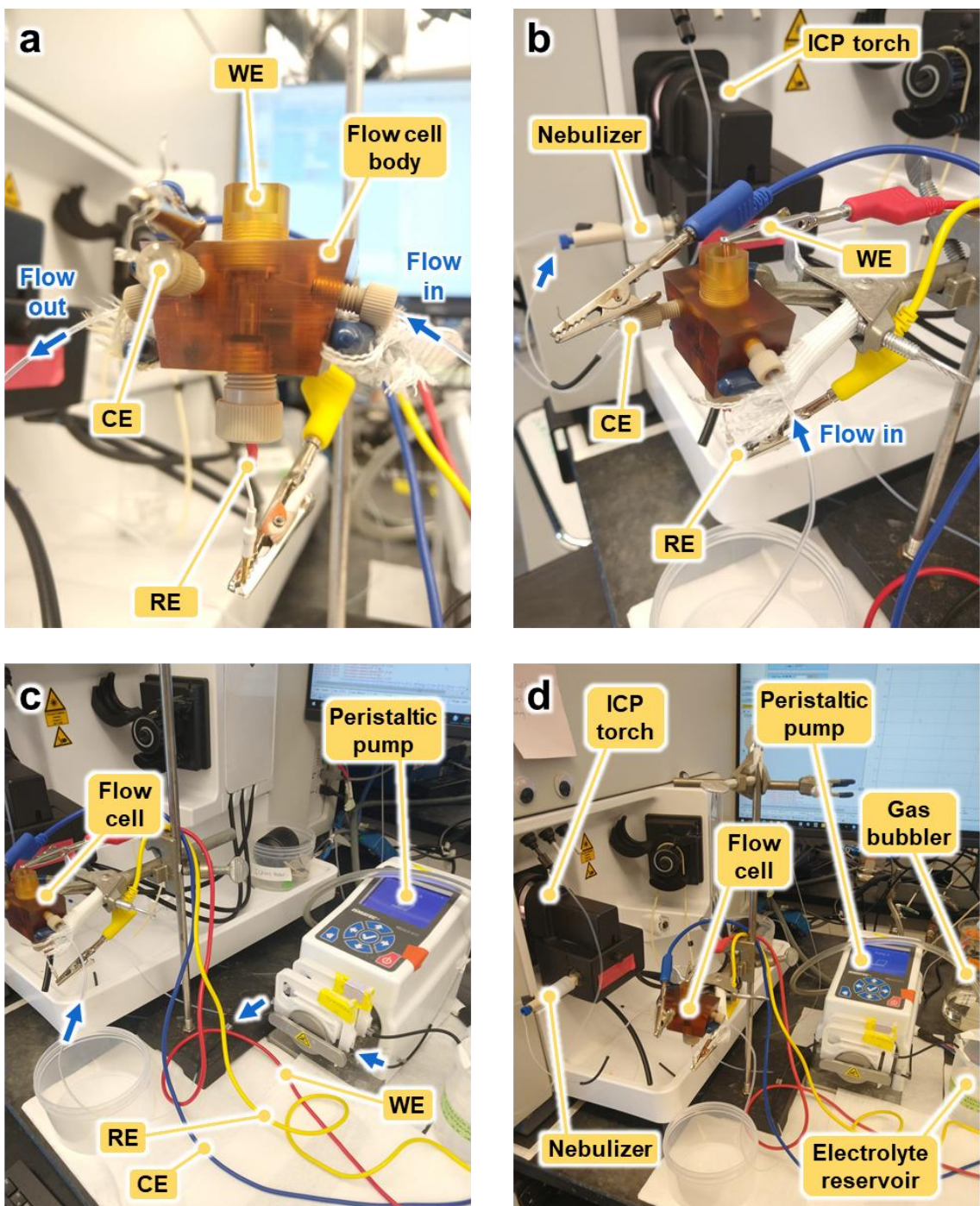


Figure S59. Photographs of the experimental setup for on-line ICP-MS experiments: (a) Close-up view of the electrochemical flow cell, showing the working electrode (WE), counter electrode (CE), and reference electrode (RE). (b) Downstream flow from the flow cell into the ICP-MS nebulizer. (c) Upstream flow into the flow cell from the peristaltic pump. (d) Overview of the entire experimental setup.

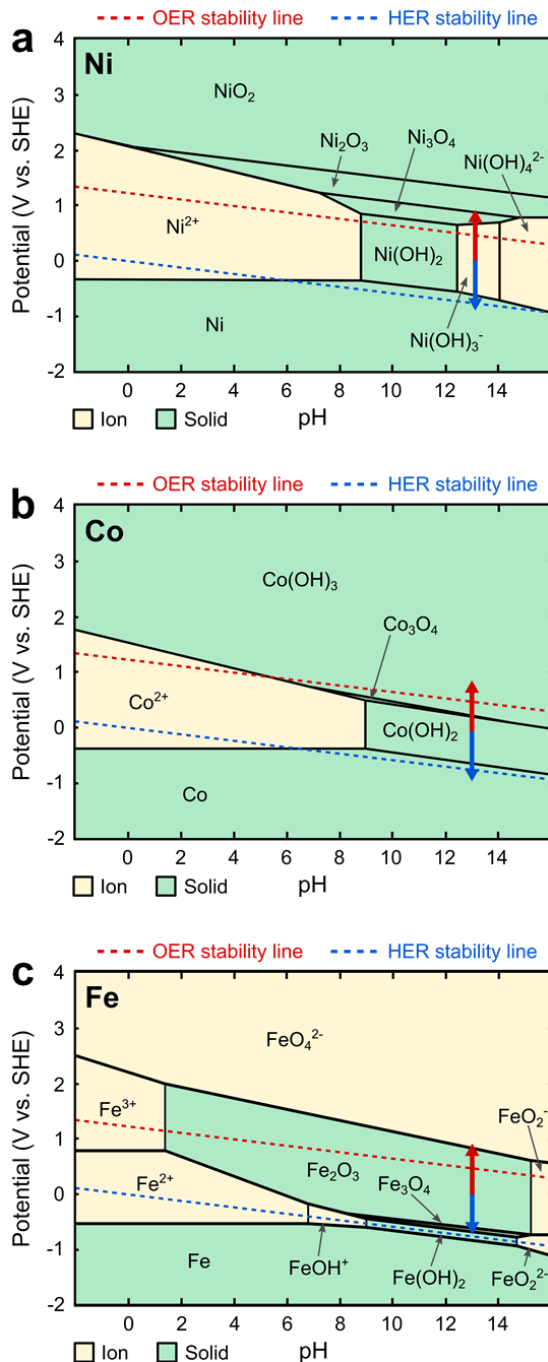


Figure S60. Electrochemical Pourbaix diagrams of (a) Ni, (b) Co, and (c) Fe using an ion concentration of $10^{-5} \text{ mol}\cdot\text{L}^{-1}$. The arrows indicate the potential transitions experienced by the materials during anodic steps (red arrow, upward) and the reverse cathodic step (blue arrow, downward) in 0.1 M KOH (pH 13). The plots were adapted from diagrams generated using the Materials Project.^{38–41}

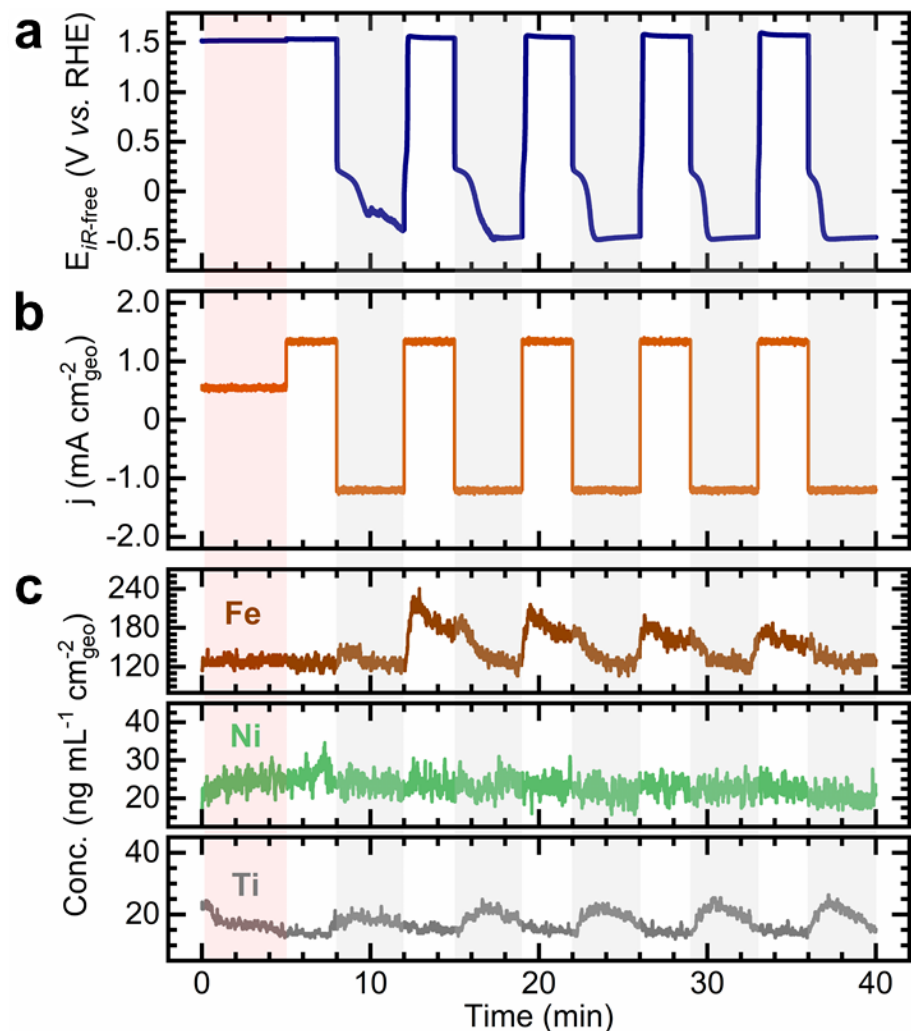


Figure S61. Metal dissolution measurements during variable operation of the $\text{NiFe}(\text{OH})_2/\text{TF}$ electrode in KOH electrolyte via on-line ICP-MS: (a) iR -corrected electrode potential profiles corresponding to (b) variable current density steps ($\pm 1.35 \text{ mA}\cdot\text{cm}^{-2}$) and (c) resulting concentration profiles for Fe, Ni, and Ti. The red-shaded area represents the initial preconditioning step at $0.5 \text{ mA}\cdot\text{cm}^{-2}$ for 5 min to oxidize the hydroxide film into oxyhydroxide. The grey-shaded areas indicate reverse current steps and serve as visual guides. Currents and concentrations are normalized to the geometric surface area of the electrode exposed to the electrolyte in the flow cell (0.197 cm^2). Experiments were carried out in unpurified 0.1 M KOH electrolyte at 20 °C with a flow rate of $2 \text{ mL}\cdot\text{min}^{-1}$.

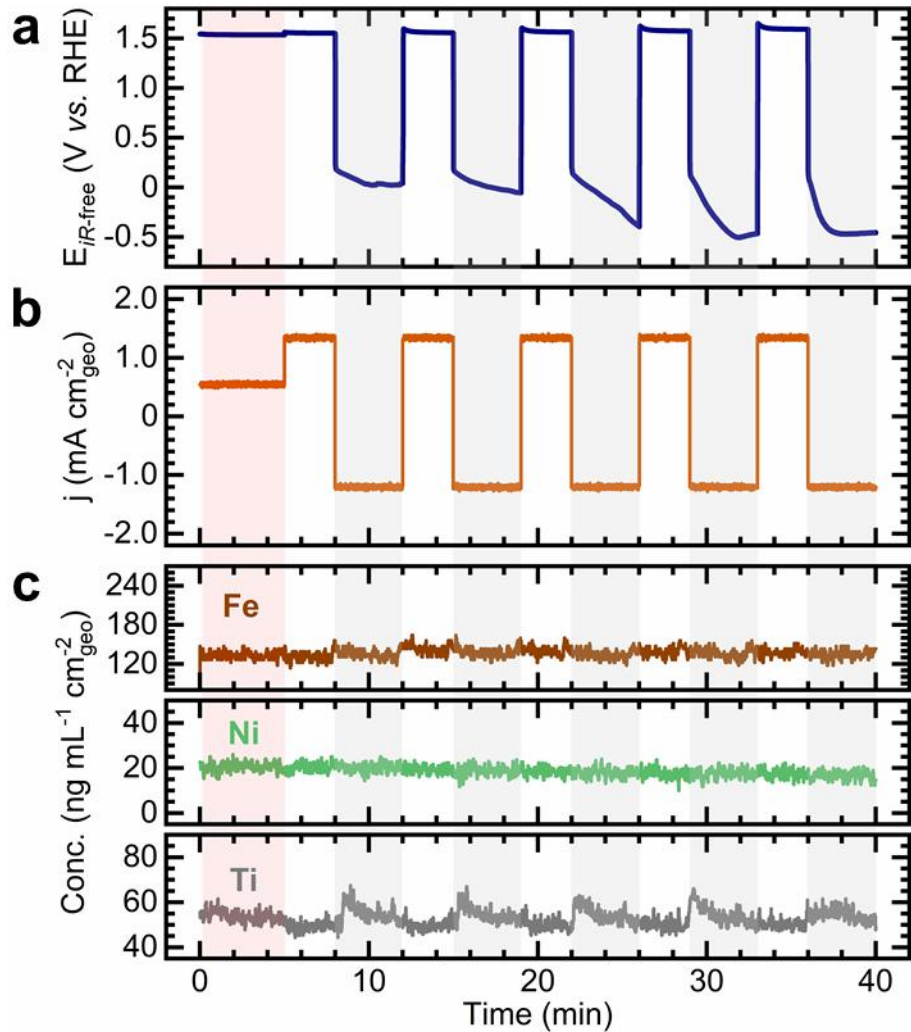


Figure S62. Metal dissolution measurements during variable operation of the $\text{NiFe}(\text{OH})_2/\text{TF}$ electrode in KOH electrolyte, spiked with KPi, via on-line ICP-MS: (a) iR -corrected electrode potential profiles corresponding to (b) variable current density steps ($\pm 1.35 \text{ mA}\cdot\text{cm}^{-2}$) and (c) resulting concentration profiles for Fe, Ni, and Ti. The red-shaded area represents the initial preconditioning step at $0.5 \text{ mA}\cdot\text{cm}^{-2}$ for 5 min to oxidize the hydroxide film into oxyhydroxide. The grey-shaded areas indicate reverse current steps and serve as visual guides. Currents and concentrations are normalized to the geometric surface area of the electrode exposed to the electrolyte in the flow cell (0.197 cm^2). Experiments were carried out in unpurified 0.1 M KOH electrolyte spiked with 5 mM KPi at 20 °C with a flow rate of $2 \text{ mL}\cdot\text{min}^{-1}$.

Accelerated catalyst degradation tests in a zero-gap water electrolyzer

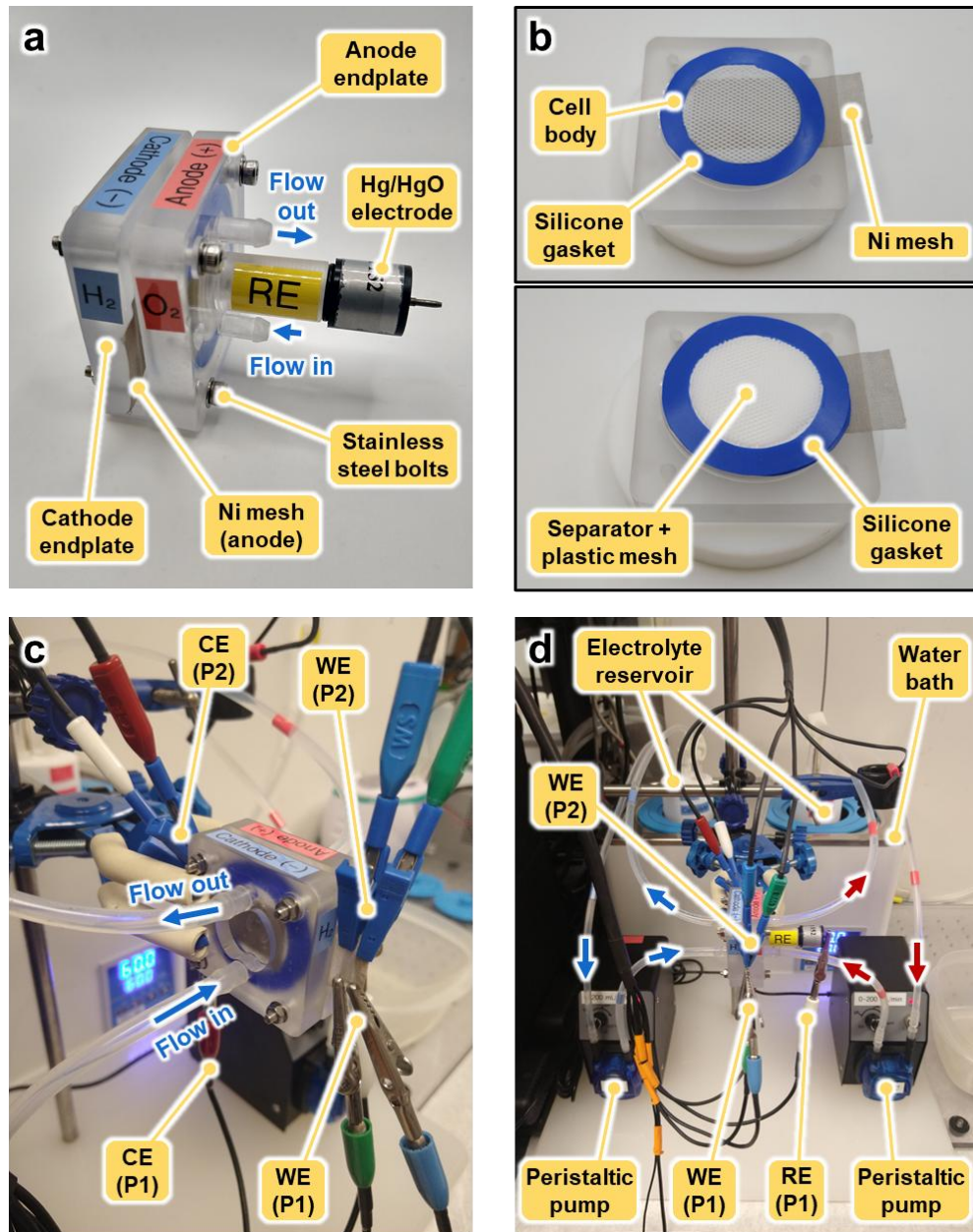


Figure S63. Zero-gap alkaline water electrolyzer for studying variable operation under industrially relevant conditions: (a) Assembled electrolyzer with a port connecting a Hg/HgO reference electrode. (b) Photographs illustrating the assembly process, where the separator is sandwiched between two Ni mesh electrodes. (c) Perspective view of the electrolyzer integrated into the flow system and connected to two potentiostats (P1 and P2). (d) Side view of the flow circuit, showing peristaltic pumps and electrolyte reservoirs for the anodic (red) and cathodic (blue) flow sections. Only P1 was connected to the reference electrode, which was used to monitor the electrode potential (O_2 or H_2 electrode, depending on the experiment), while P2 measured the total cell potential.

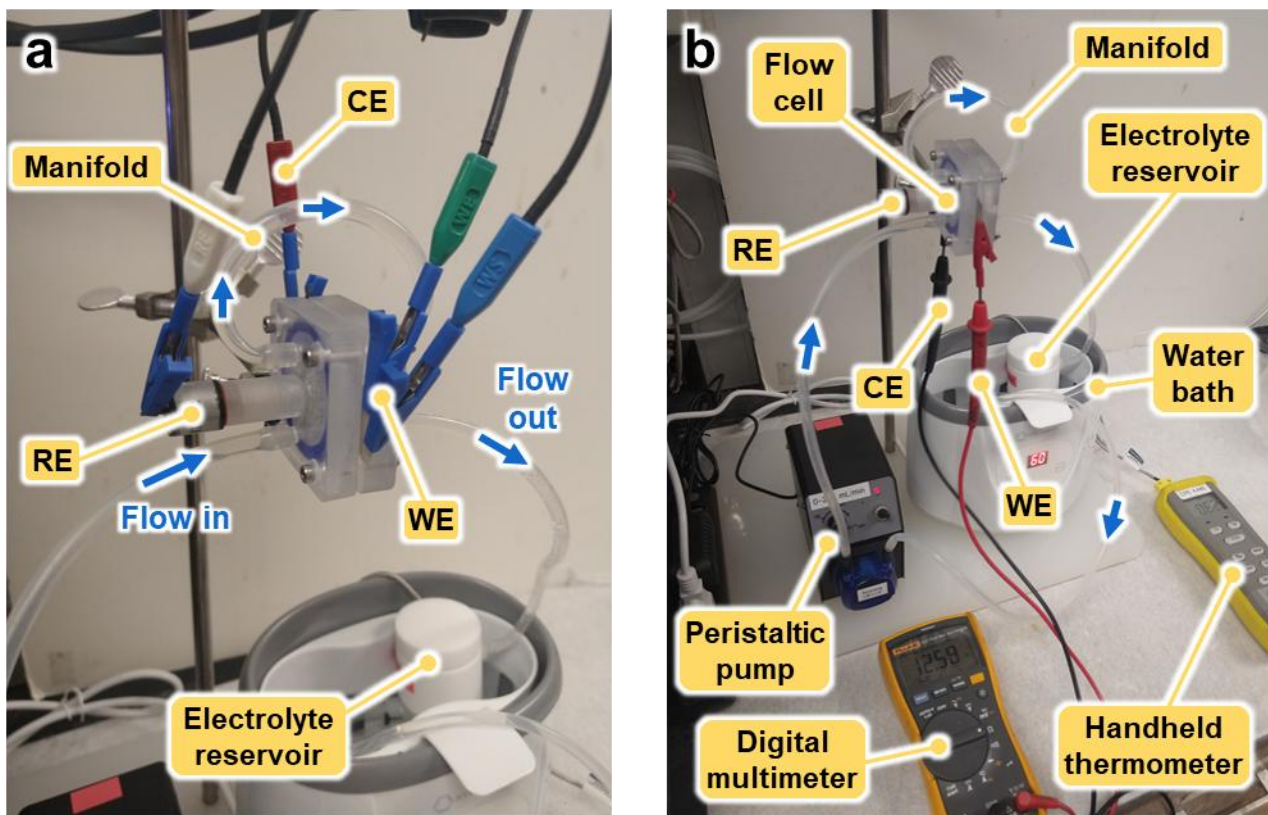


Figure S64. Configuration for estimating ionic resistance through the manifold in a zero-gap alkaline water electrolyzer: (a) Perspective view of the assembled electrolyzer, where a 7.6 cm section of silicone tubing serves as the manifold to ionically connect the Ni mesh electrodes. For this measurement only, the porous separator was replaced with a 1 mm-thick circular plastic sheet to block the internal ionic path and redirect ion flow exclusively through the manifold. (b) Full experimental setup, showing the measured resistance (~ 12.58 k Ω) through the manifold using a multimeter. Measurements were conducted in unpurified 7 M KOH at 50 °C with a flow rate of 200 mL·min $^{-1}$.

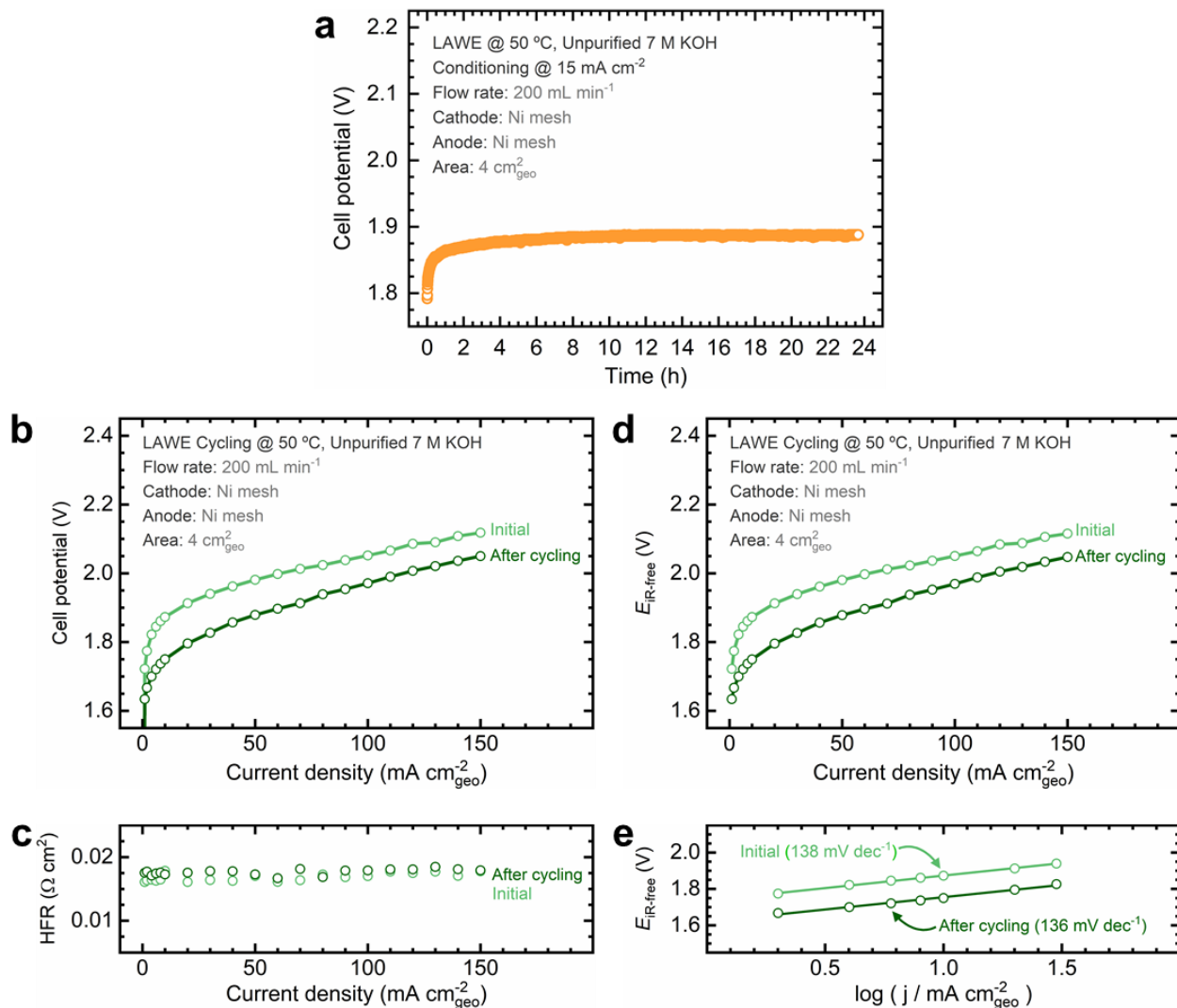


Figure S65. Full-cell electrochemical performance of the zero-gap alkaline water electrolyzer operating with Ni mesh electrodes before and after variable operation stability tests: (a) electrolyzer conditioning at 60 mA for 24 h; (b) full-cell polarization curves and (c) corresponding HFR values at each current step; (d) *iR*-corrected polarization curves constructed from (b) and (c); (e) Tafel plots constructed from (d). Uncertainty bars indicate the standard deviation derived from three replicate measurements. Experimental conditions: unpurified 7 M KOH electrolyte at 50 °C, 200 mL·min⁻¹.

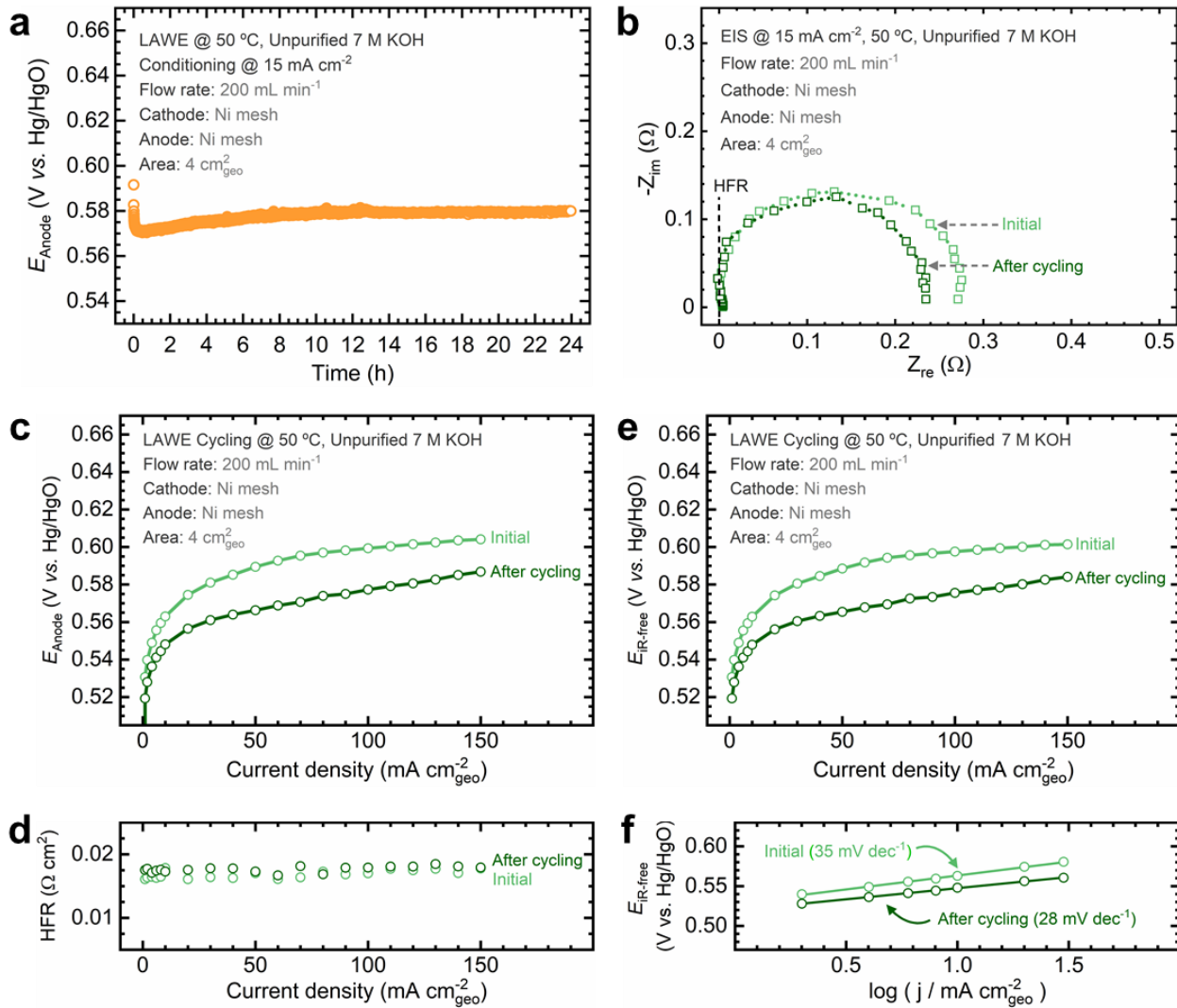


Figure S66. Electrochemical performance of the Ni mesh O₂ electrode in the zero-gap alkaline water electrolyzer before and after variable operation stability tests: (a) electrode potential during conditioning at 60 mA for 24 h; (b) Nyquist plots from EIS measurements; (c) polarization curves and (d) corresponding HFR values at each current step; (e) *iR*-corrected polarization curves constructed from (c) and (d); (f) Tafel plots constructed from (e). Uncertainty bars indicate the standard deviation derived from three replicate measurements. The electrode potential was measured by positioning the Ni mesh O₂ electrode in the endplate with the reference electrode port and recording measurements using potentiostat #1. Experimental conditions: unpurified 7 M KOH electrolyte at 50 °C, 200 mL·min⁻¹.

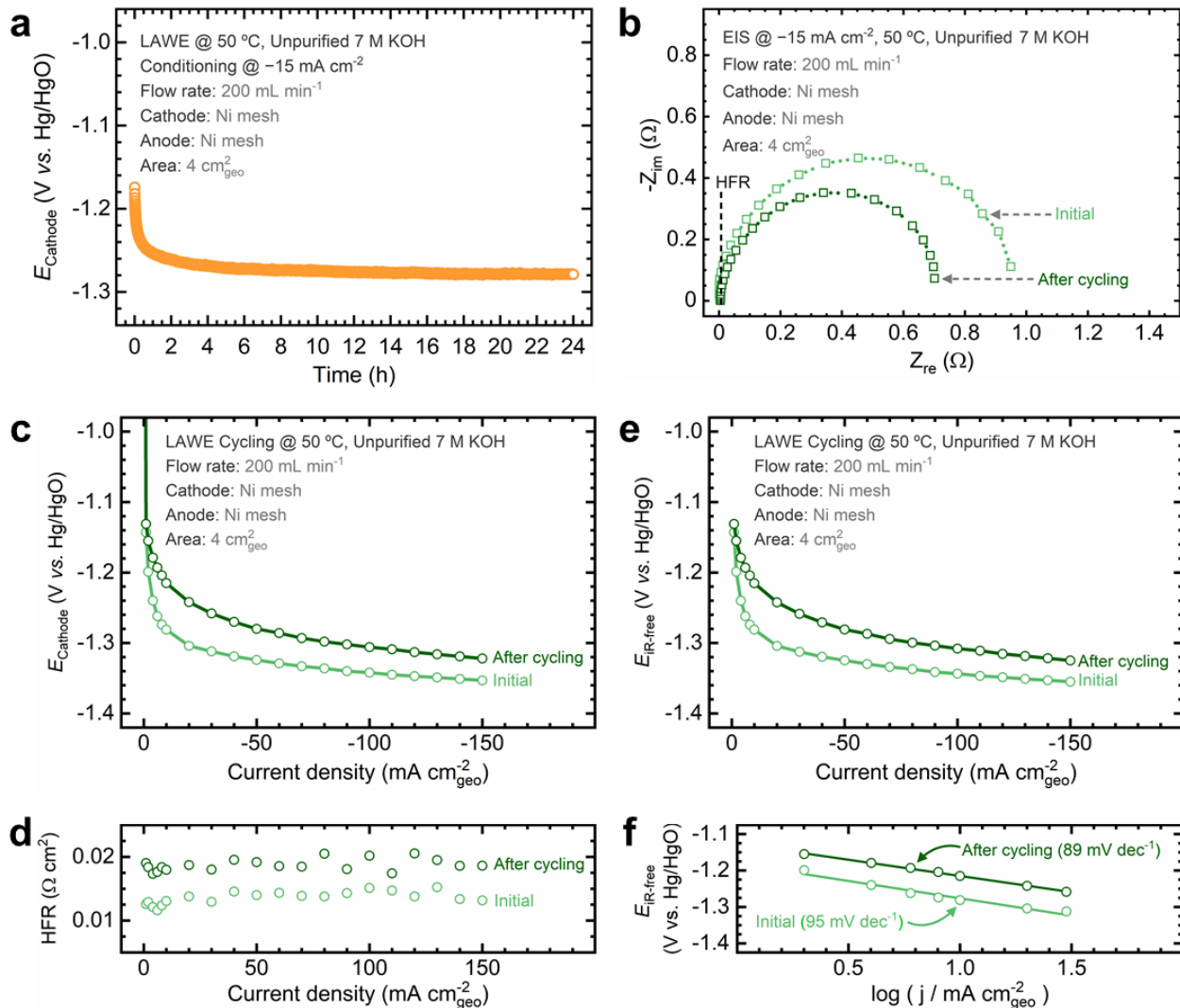


Figure S67. Electrochemical performance of the Ni mesh H₂ electrode (cathode) in the zero-gap alkaline water electrolyzer before and after variable operation stability tests: (a) electrode potential during conditioning at -60 mA for 24 h; (b) Nyquist plots from EIS measurements; (c) polarization curves and (d) corresponding HFR values at each current step; (e) *iR*-corrected polarization curves constructed from (c) and (d); (f) Tafel plots constructed from (e). Uncertainty bars indicate the standard deviation derived from three replicate measurements. The electrode potential was measured by positioning the Ni mesh H₂ electrode in the endplate with the reference electrode port and recording measurements using potentiostat #1. Experimental conditions: unpurified 7 M KOH electrolyte at 50 °C, 200 mL·min⁻¹.

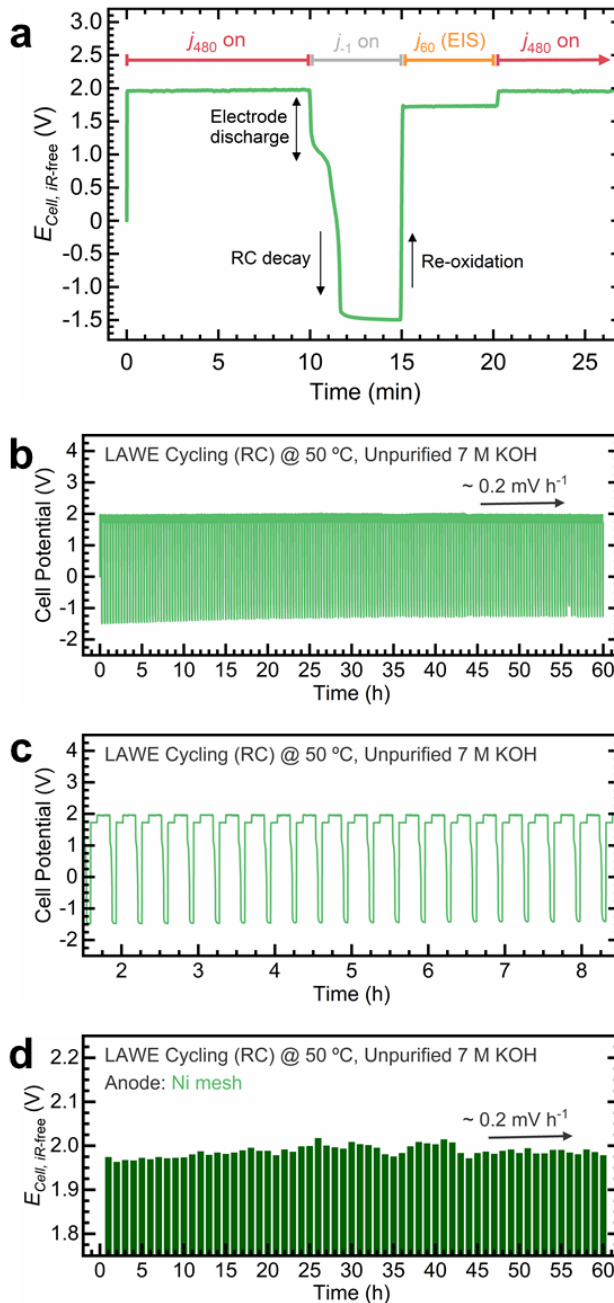


Figure S68. LAWE full-cell stability tests of Ni mesh electrodes under variable operation with a reverse current (RC) step in a zero-gap alkaline water electrolyzer: (a) Snapshot of a single cycle, showing a constant current step at 480 mA followed by a reverse current step of -1 mA to simulate shutdown, followed by an EIS measurement. (b) Full-cell potential progression over 240 cycles; (c) Detailed view of the cell potential profile under variable operation, revealing the reverse current steps with more detail. (d) iR -corrected cell potential throughout the stability test, with each bar representing the average potential during the constant current step per cycle. The arrows in (b) and (d) indicate the potential increase rate during the highlighted intervals. Experimental conditions: unpurified 7 M KOH electrolyte at 50 °C, 200 mL·min⁻¹.

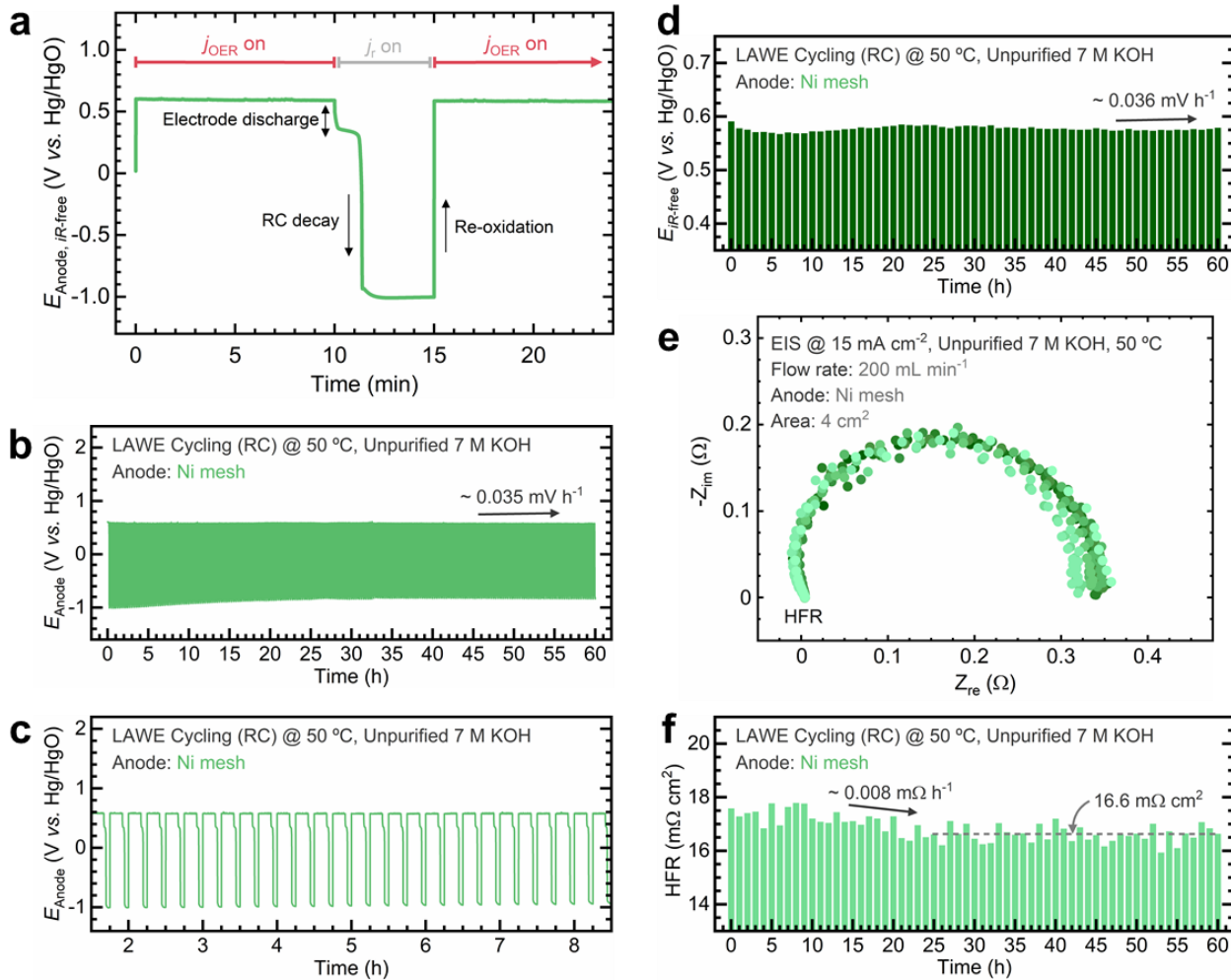


Figure S69. LAWE stability tests of the Ni mesh O₂ electrode (anode) under variable operation with an RC step in a zero-gap alkaline water electrolyzer: (a) Snapshot of a single cycle, showing a constant current step at 480 mA followed by a reverse current step of -1 mA to simulate shutdown. (b) Electrode potential progression over 240 cycles; (c) Detailed view of the O₂ electrode potential profile under variable operation, revealing the reverse current steps with more detail. (d) *iR*-corrected O₂ electrode potential throughout the stability test, with each bar representing the average potential during the constant current step per cycle. (e) Nyquist plots collected over the stability test. (f) HFR measured from Nyquist plots over the stability test. The arrows in (b) and (d) indicate the potential increase rate during the highlighted intervals. The arrow in (f) indicates the HFR decrease rate during the highlighted interval, while the dashed line represents the average HFR value once stabilized. Experimental conditions: unpurified 7 M KOH electrolyte at 50 °C, 200 mL·min⁻¹.

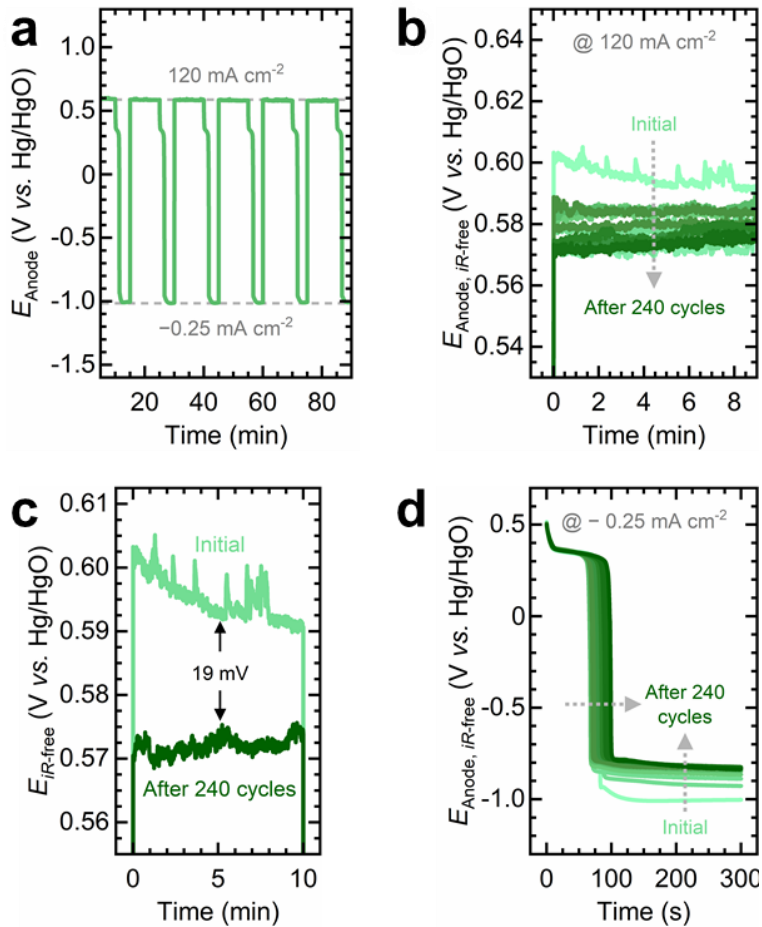


Figure S70. LAWE stability tests of the Ni mesh O₂ electrode (anode) under variable operation with an RC step in a zero-gap alkaline water electrolyzer: (a) Snapshot of the electrode potential profile under variable operation, highlighting the potential thresholds reached during the constant current and reverse current steps. (b) Comparison of the *iR*-corrected O₂ electrode potential across cycles. (c) *iR*-corrected O₂ electrode potential curves at the initial and final constant current steps, highlighting their potential differences. (d) Comparison of the *iR*-corrected O₂ electrode potential during the reverse current step across cycles. The arrows in (b) and (d) indicate the progression of potential profiles during cycling.

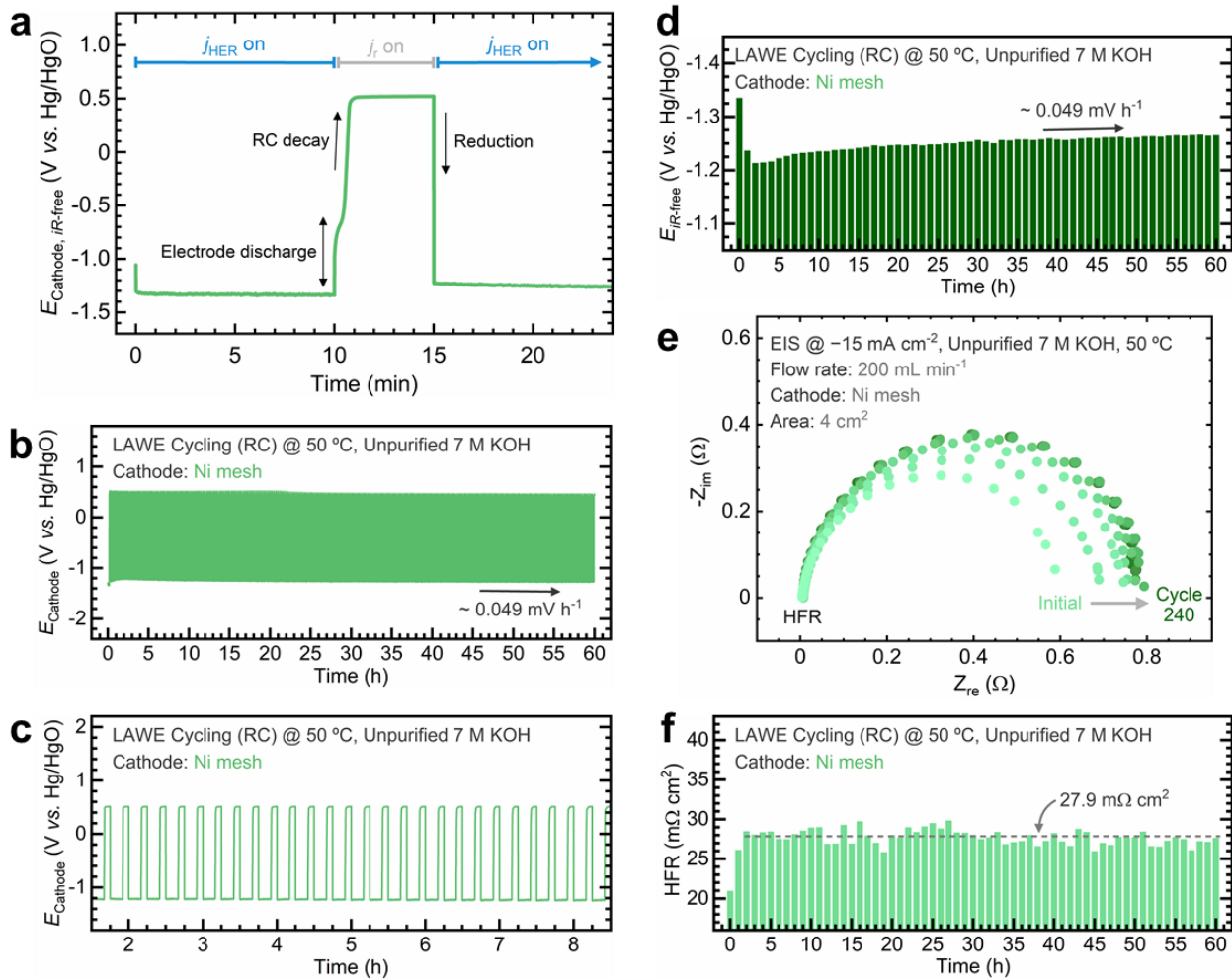


Figure S71. LAWE stability tests of the Ni mesh H₂ electrode (cathode) under variable operation with an RC step in a zero-gap alkaline water electrolyzer: (a) Snapshot of a single cycle, showing a constant current step at -480 mA followed by a reverse current step of 1 mA to simulate shutdown. (b) Electrode potential progression over 240 cycles; (c) Detailed view of the H₂ electrode potential profile under variable operation, revealing the reverse current steps in more detail. (d) *iR*-corrected H₂ electrode potential throughout the stability test, with each bar representing the average potential during the constant current step per cycle. (e) Nyquist plots collected over the stability test. (f) HFR measured from Nyquist plots over the stability test. The arrows in (b) and (d) indicate the potential increase rate during the highlighted intervals. The grey arrow in (e) represents the evolution of the semicircle throughout the stability test. The dashed line in (f) represents the average HFR value once stabilized. Experimental conditions: unpurified 7 M KOH electrolyte at 50 °C, 200 mL·min⁻¹.

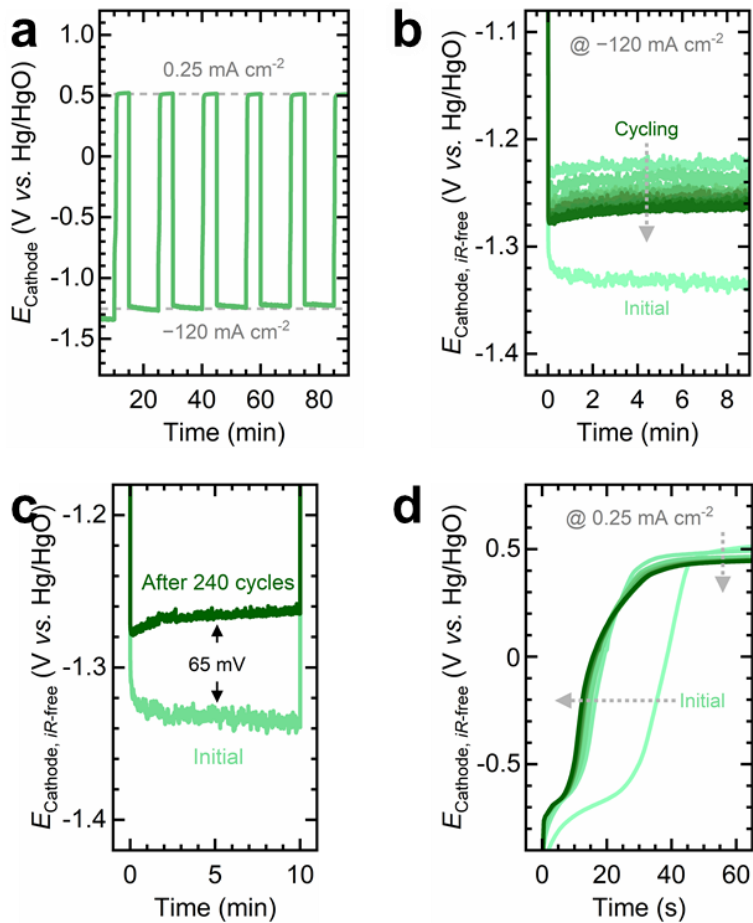


Figure S72. LAWE stability tests of the Ni mesh H₂ electrode (cathode) under variable operation with an RC step in a zero-gap alkaline water electrolyzer: (a) Snapshot of the electrode potential profile under variable operation, highlighting the potential thresholds reached during the constant current and reverse current steps. (b) Comparison of the *iR*-corrected H₂ electrode potential across cycles. (c) *iR*-corrected H₂ electrode potential curves at the initial and final constant current steps, highlighting their potential differences. (d) Comparison of the *iR*-corrected H₂ electrode potential during the reverse current step across cycles. The arrows in (b) and (d) indicate the progression of potential profiles during cycling.

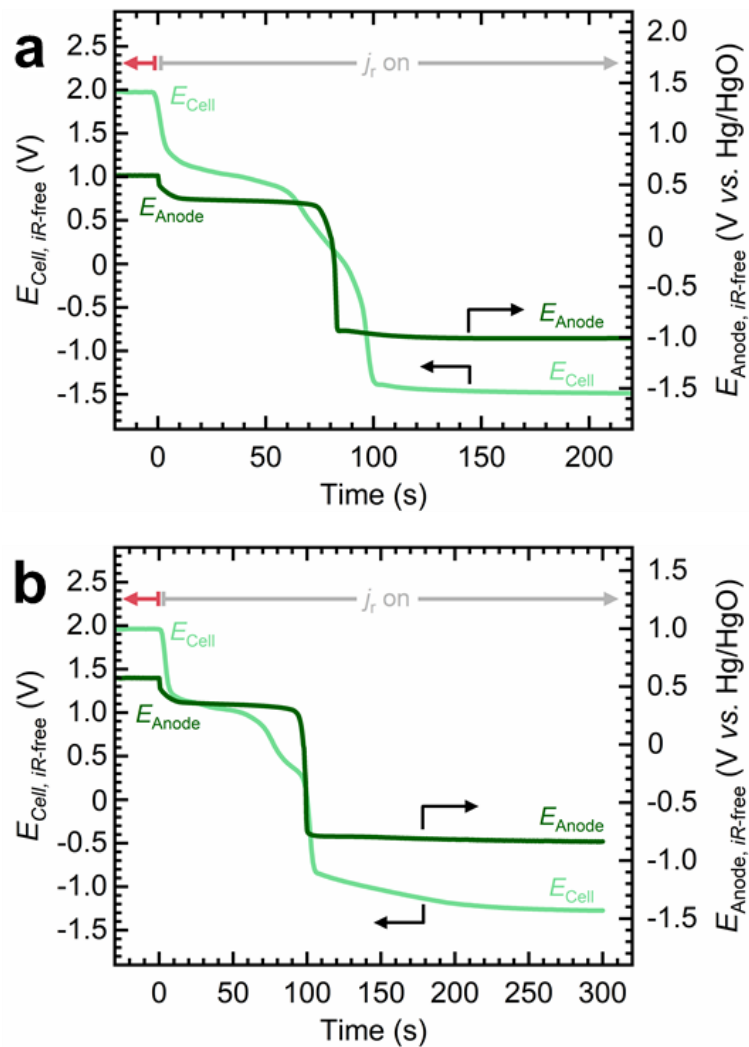


Figure S73. Decoupling the O₂ electrode potential during LAWE variable operation tests in a zero-gap alkaline water electrolyzer: Comparison of total cell potential (left y-axis) and O₂ electrode (anode) potential (right y-axis) decay during the reverse current step (a) before and (b) after 240 cycles (experiment shown in Fig. S70).

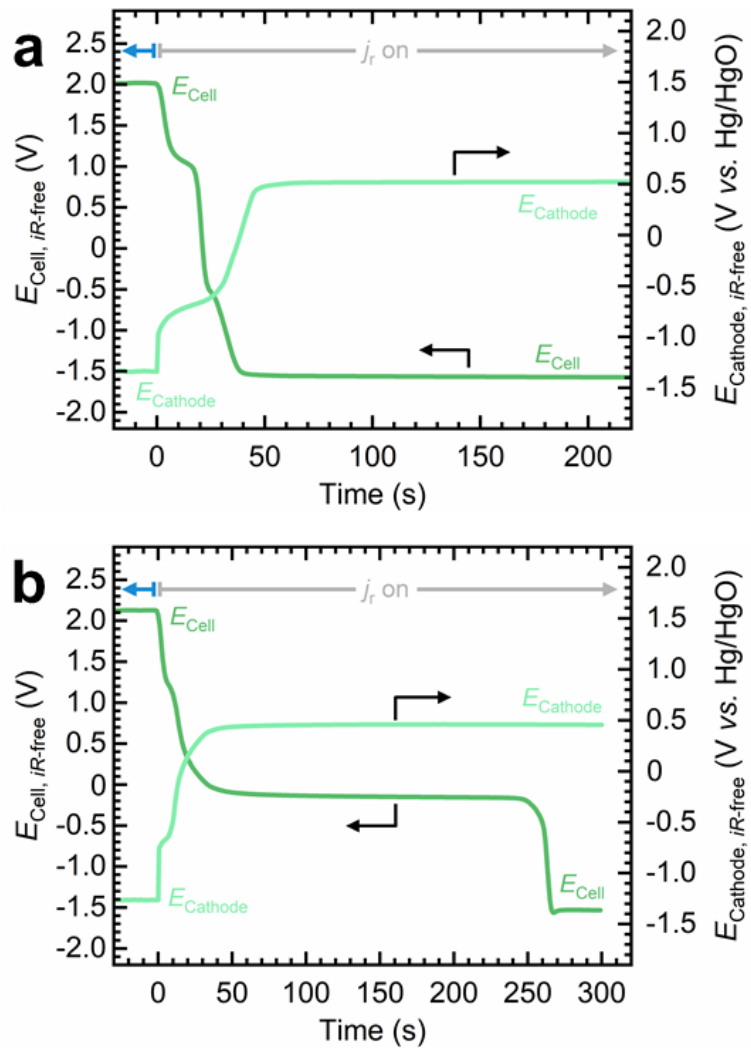


Figure S74. Decoupling the H₂ electrode potential during LAWE variable operation tests in a zero-gap alkaline water electrolyzer: Comparison of total cell potential (left y-axis) and H₂ electrode (cathode) potential (right y-axis) decay during the reverse current step (a) before and (b) after 240 cycles (experiment shown in **Fig. S72**).

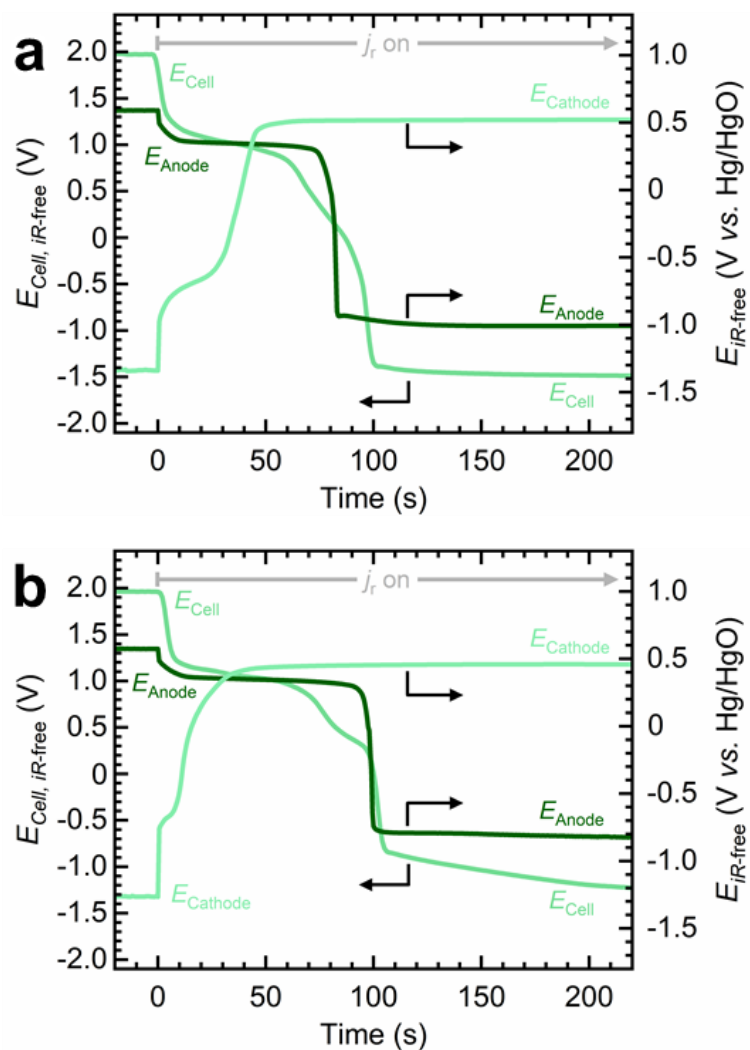


Figure S75. Decoupling the O_2 (anode) and H_2 (cathode) potentials during LAWE variable operation tests in a zero-gap alkaline water electrolyzer: Comparison of total cell potential (left y-axis) and the anode/cathode potential (right y-axis) decay during the reverse current step (a) before and (b) after 240 cycles.

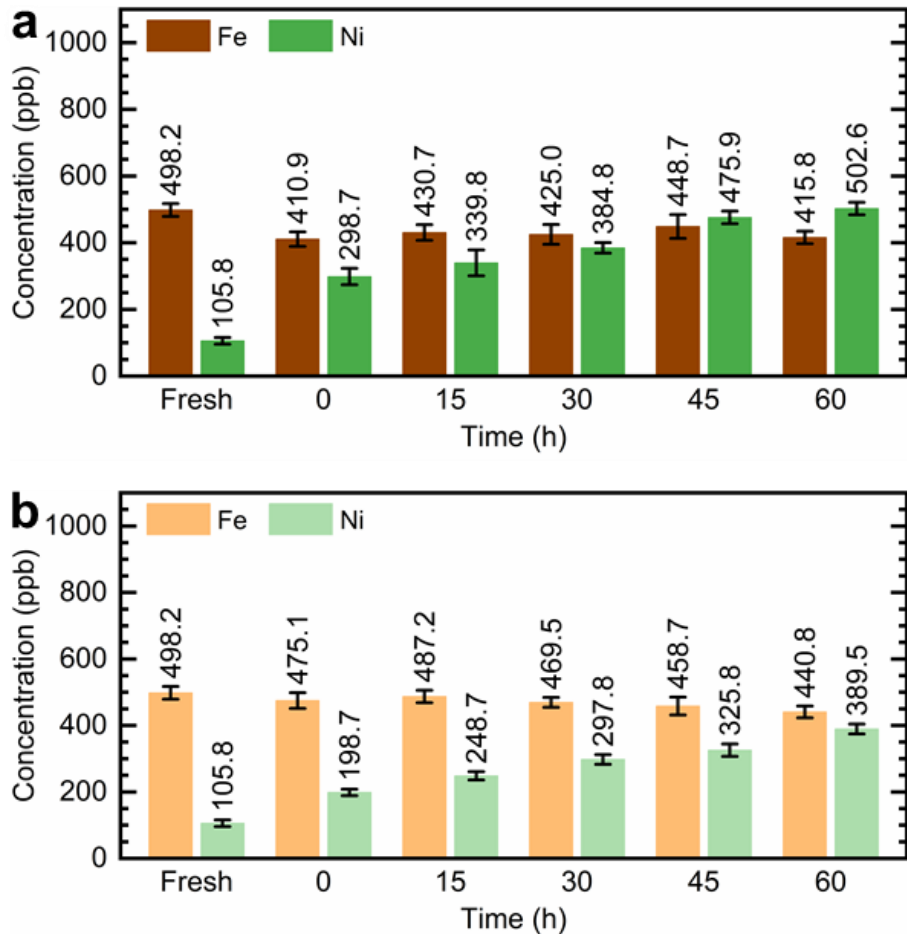


Figure S76. Ni and Fe concentrations in 7 M KOH electrolyte over cycling time during LAWE variable operation in a zero-gap electrolyzer: (a) metal concentrations in the anolyte (electrolyte recirculated on the O₂ electrode side) and (b) metal concentrations in the catholyte (electrolyte recirculated on the H₂ electrode side). Concentrations were determined via ex situ ICP-MS, with 250 µL electrolyte samples collected from the reservoirs at the specified intervals. Columns for the fresh condition represent the as-prepared KOH electrolyte, while time 0 corresponds to the electrolyte after 24 h of electrolyzer conditioning. Uncertainty bars represent the standard deviation from three replicate measurements.

Supporting note: Ni and Fe concentrations change significantly after conditioning, reflecting the formation of the (oxy)hydroxide layer. On the O₂ electrode, Fe is removed from the electrolyte as it incorporates into NiOOH, while Ni is released due to oxidation. Ni and Fe concentrations steadily increase during cycling due to variable operation. Ni dissolution is more pronounced on the O₂ electrode, likely due to the stronger impact of polarity reversals on its thicker (oxy)hydroxide film than the H₂ electrode.

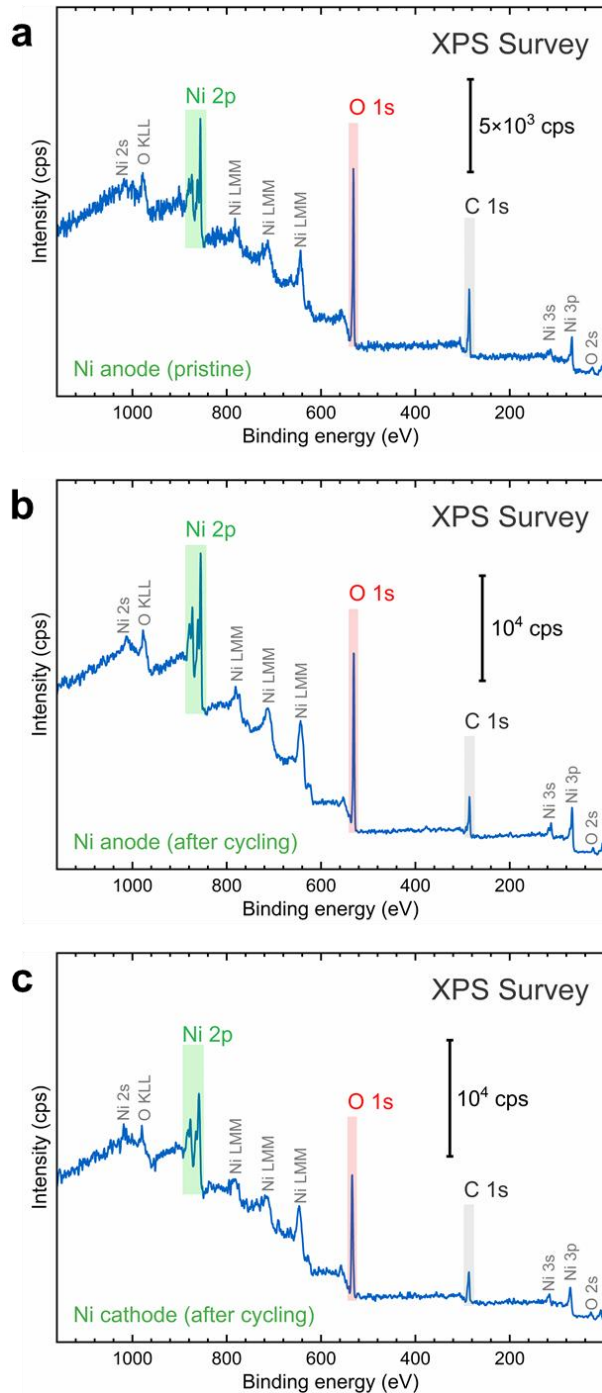


Figure S77. Ex situ XPS analysis of the Ni mesh electrodes used in LAWE stability tests under variable operation in a zero-gap alkaline water electrolyzer: XPS survey scans of the (a) pristine Ni mesh electrode after conditioning; (b) Ni mesh O₂ electrode (anode) and (c) Ni mesh H₂ electrode (cathode) after 240 cycles.

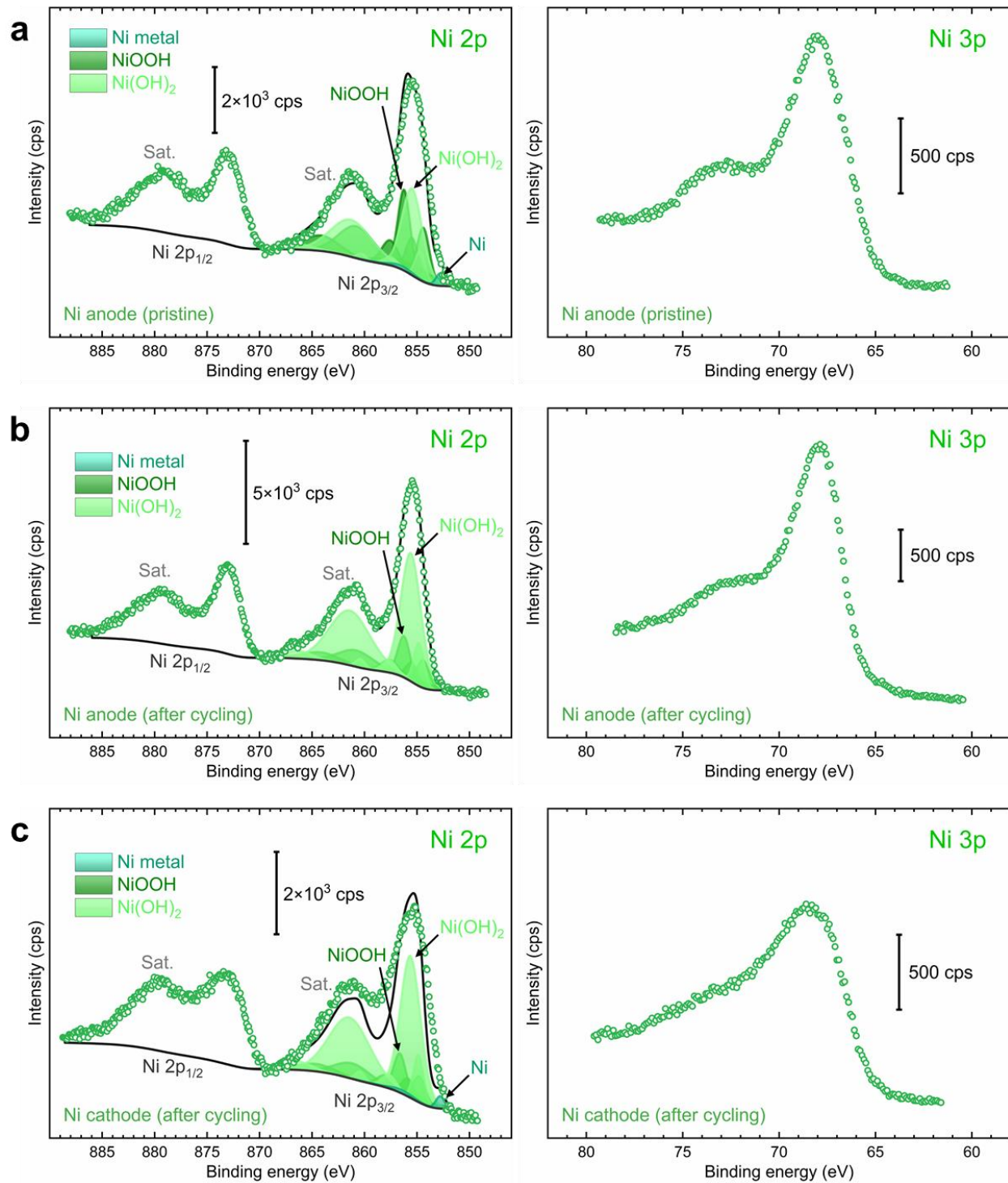


Figure S78. Ex situ XPS analysis of the Ni mesh electrodes used in LAWE stability tests under variable operation in a zero-gap alkaline water electrolyzer: XPS spectra of the Ni 2p (left) and Ni 3p (right) regions for the (a) pristine Ni mesh electrode after conditioning, (b) Ni mesh O₂ electrode (anode), and (c) Ni mesh H₂ electrode (cathode) after 240 cycles. Original XPS spectra are shown as open circles, while solid lines represent the fitted component envelopes. Individual components are color-coded for each species.

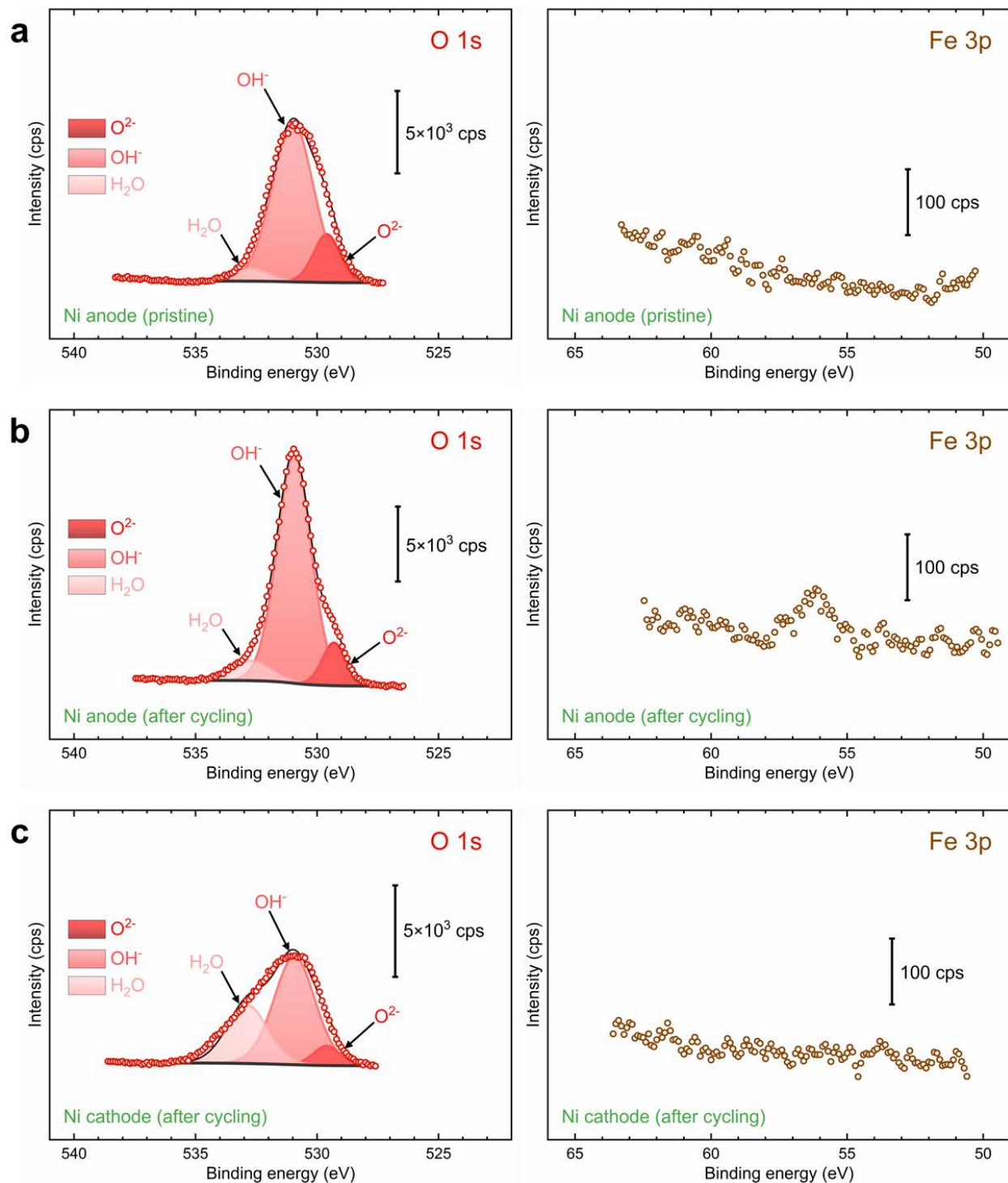


Figure S79. Ex situ XPS analysis of the Ni mesh electrodes used in LAWE stability tests under variable operation in a zero-gap alkaline water electrolyzer: XPS spectra of the O 1s (left) and Fe 3p (right) regions for the (a) pristine Ni mesh electrode after conditioning, (b) Ni mesh O₂ electrode (anode), and (c) Ni mesh H₂ electrode (cathode) after 240 cycles. Original XPS spectra are shown as open circles, while solid lines represent the fitted component envelopes. Individual components are color-coded for each species.

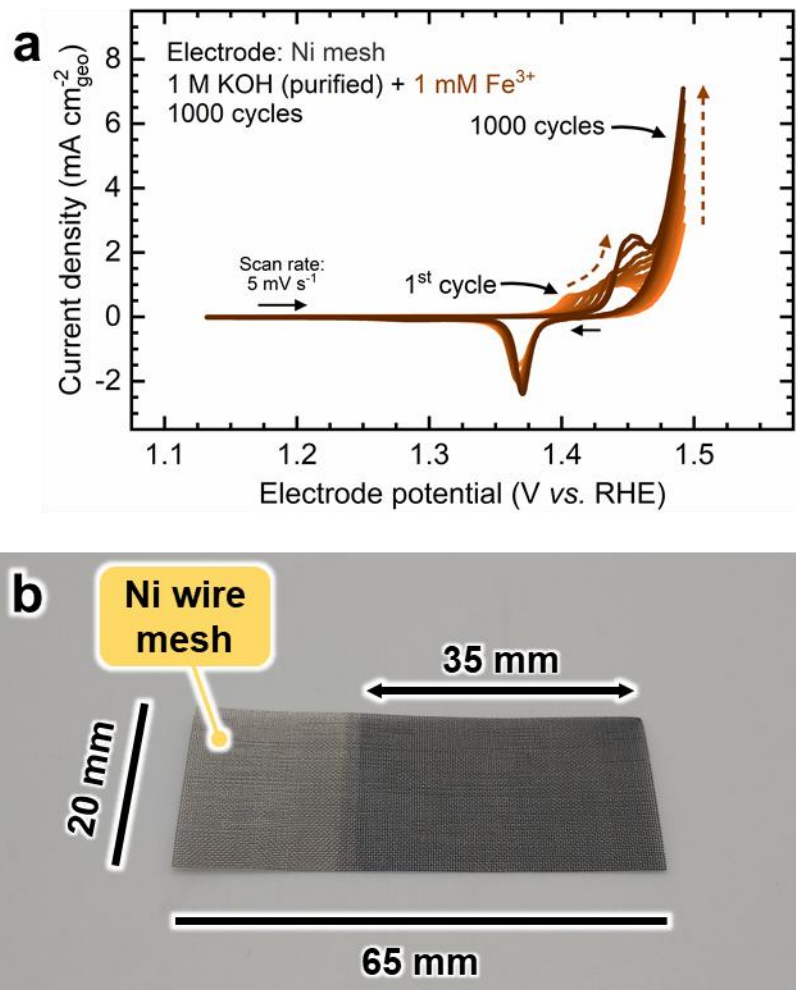


Figure S80. Electrochemical preparation of a Fe-doped Ni mesh electrode via in situ Fe incorporation: (a) Cyclic voltammetry scans used to form a thick Fe-doped Ni oxyhydroxide layer on a Ni mesh electrode immersed in purified 1 M KOH electrolyte containing 1 mM Fe³⁺ ions. (b) Photograph of the Ni mesh electrode showing a distinct color change in the portion exposed to the electrolyte. The dashed arrow in (a) shows the increase in OER activity during CV cycling.

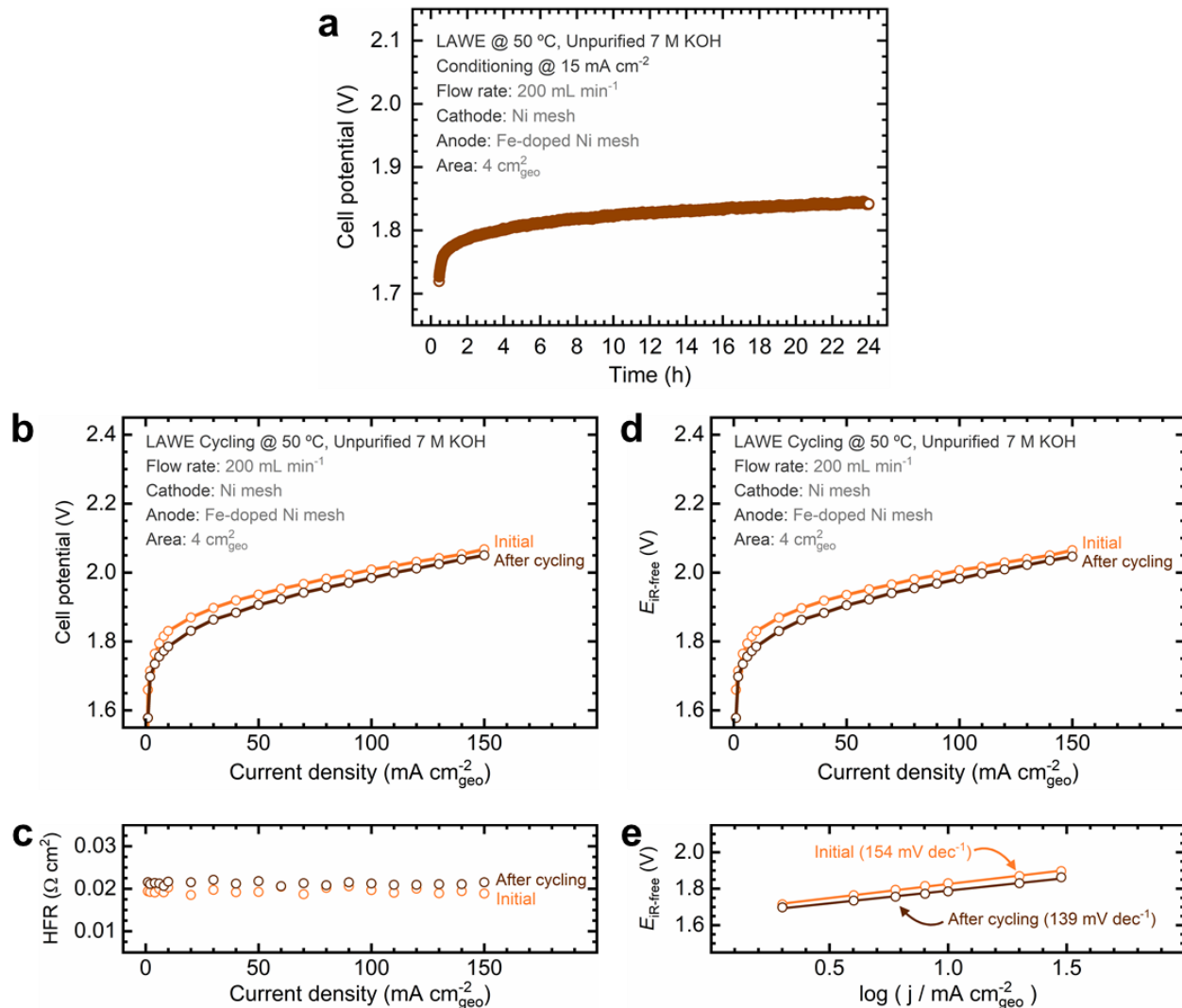


Figure S81. Full-cell electrochemical performance of the zero-gap alkaline water electrolyzer operating with a Fe-doped Ni mesh O₂ electrode (anode) before and after variable operation stability tests: (a) electrolyzer conditioning at 60 mA for 24 h; (b) full-cell polarization curves and (c) corresponding HFR values at each current step; (d) *iR*-corrected polarization curves constructed from (b) and (c); (e) Tafel plots constructed from (d). Experimental conditions: unpurified 7 M KOH electrolyte at 50 °C, 200 mL·min⁻¹.

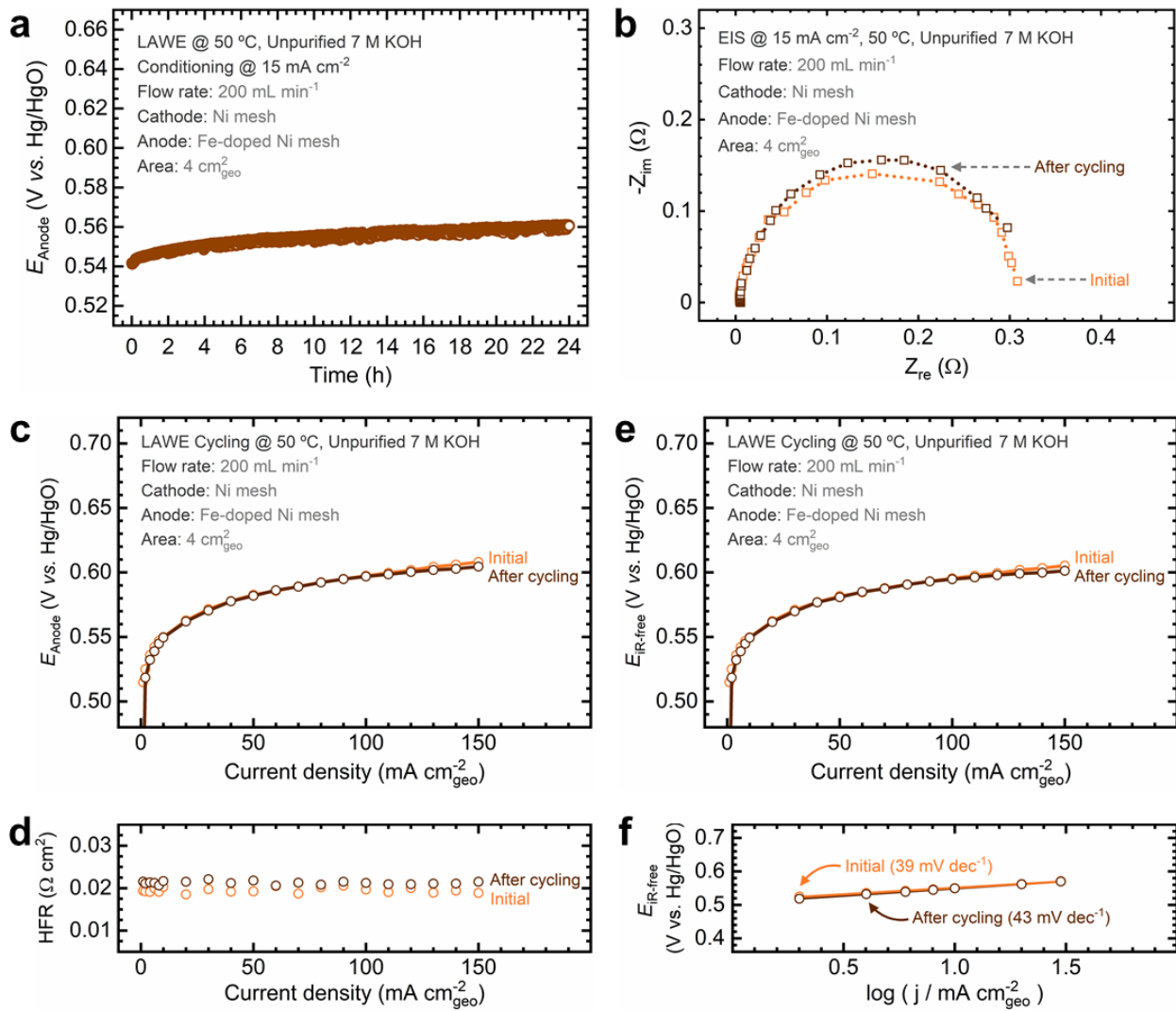


Figure S82. Electrochemical performance of the Fe-doped Ni mesh O₂ electrode (anode) in the zero-gap alkaline water electrolyzer before and after variable operation stability tests: (a) electrode potential during conditioning at 60 mA for 24 h; (b) Nyquist plots from EIS measurements; (c) polarization curves and (d) corresponding HFR values at each current step; (e) iR -corrected polarization curves constructed from (c) and (d); (f) Tafel plots constructed from (e). The O₂ electrode potential was measured by positioning the Ni mesh anode in the endplate with the reference electrode port and recording measurements using potentiostat #1. Experimental conditions: unpurified 7 M KOH electrolyte at 50 °C, 200 mL·min⁻¹.

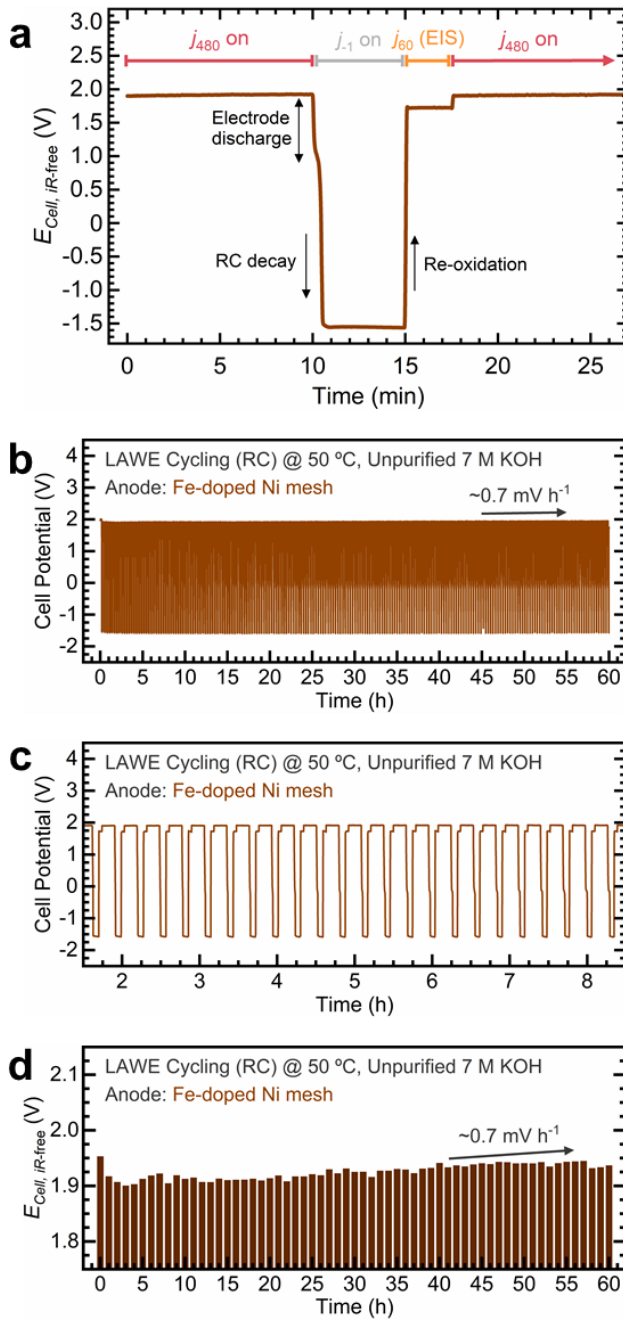


Figure S83. LAWE full-cell stability tests of the Fe-doped Ni mesh O₂ electrode (anode) under variable operation with a reverse current (RC) step in a zero-gap alkaline water electrolyzer: (a) Snapshot of a single cycle, showing a constant current step at 480 mA followed by a reverse current step of -1 mA to simulate shutdown, followed by an EIS measurement. (b) Full-cell potential progression over 240 cycles; (c) Detailed view of the cell potential profile under variable operation, revealing the reverse current steps with more detail. (d) iR -corrected cell potential throughout the stability test, with each bar representing the average potential during the constant current step per cycle. The arrows in (b) and (d) indicate the potential increase rate during the highlighted intervals. Experimental conditions: unpurified 7 M KOH electrolyte at 50 °C, 200 mL·min⁻¹.

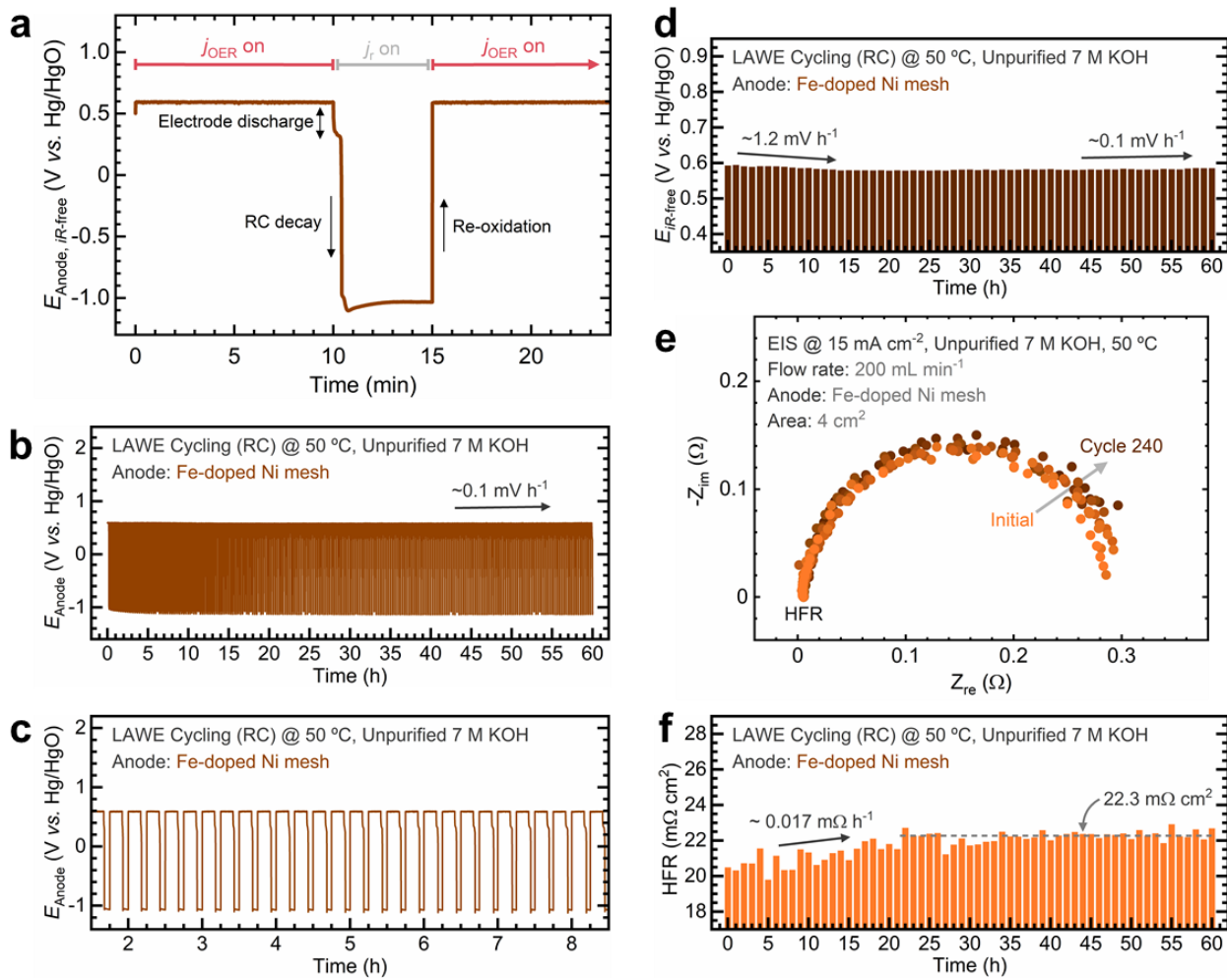


Figure S84. LAWE stability tests of the Fe-doped Ni mesh O₂ electrode (anode) under variable operation with an RC step in a zero-gap alkaline water electrolyzer: (a) Snapshot of a single cycle, showing a constant current step at 480 mA followed by a reverse current step of -1 mA to simulate shutdown. (b) O₂ electrode potential progression over 240 cycles; (c) Detailed view of the O₂ electrode potential profile under variable operation, revealing the reverse current steps with more detail. (d) *iR*-corrected O₂ electrode potential throughout the stability test, with each bar representing the average potential during the constant current step per cycle. (e) Nyquist plots collected over the stability test. (f) HFR measured from Nyquist plots over the stability test. The arrows in (b) and (d) indicate the potential increase (upwards)/decrease (downwards) rate during the highlighted intervals. The grey arrow in (e) represents the evolution of the semicircle throughout the stability test. The arrow in (f) indicates the HFR increase rate during the highlighted interval, while the dashed line represents the average HFR value once stabilized. Experimental conditions: unpurified 7 M KOH electrolyte at 50 °C, 200 mL·min⁻¹.

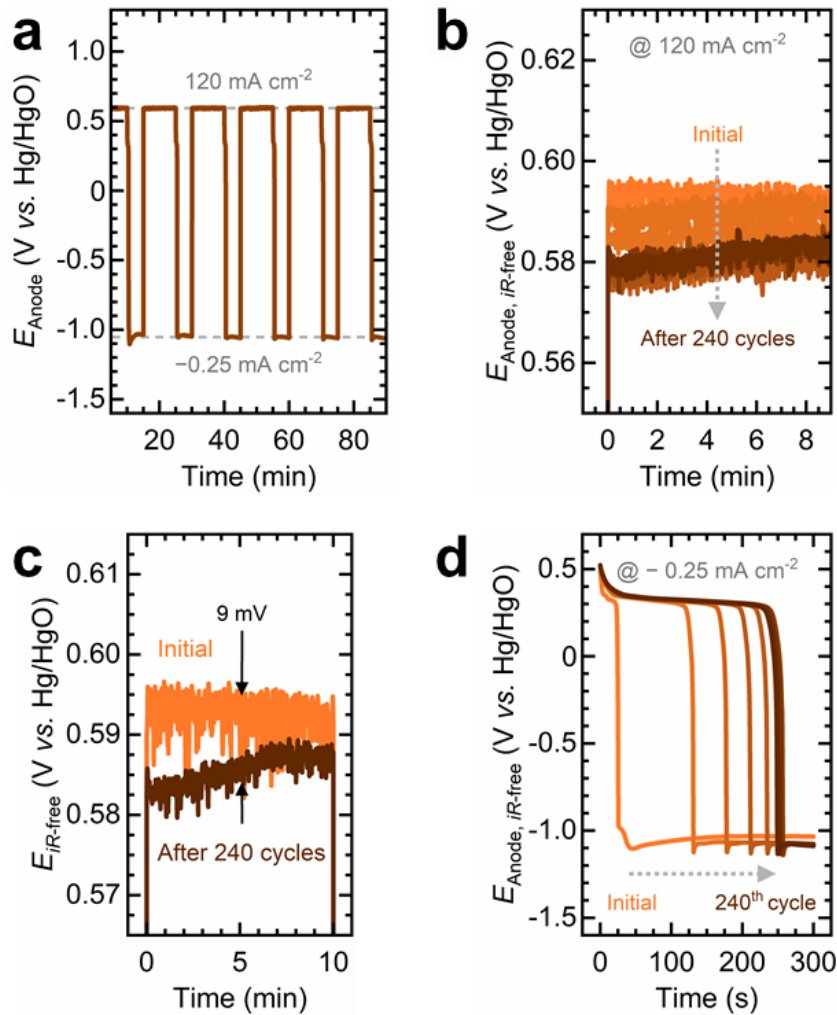


Figure S85. LAWE stability tests of the Fe-doped Ni mesh O₂ electrode (anode) under variable operation with an RC step in a zero-gap alkaline water electrolyzer: (a) Snapshot of the O₂ electrode potential profile under variable operation, highlighting the potential thresholds reached during the constant current and reverse current steps. (b) Comparison of the *iR*-corrected O₂ electrode potential across cycles. (c) *iR*-corrected O₂ electrode potential curves at the initial and final constant current steps, highlighting their potential differences. (d) Comparison of the *iR*-corrected O₂ electrode potential during the reverse current step across cycles. The arrows in (b) and (d) indicate the progression of potential profiles during cycling.

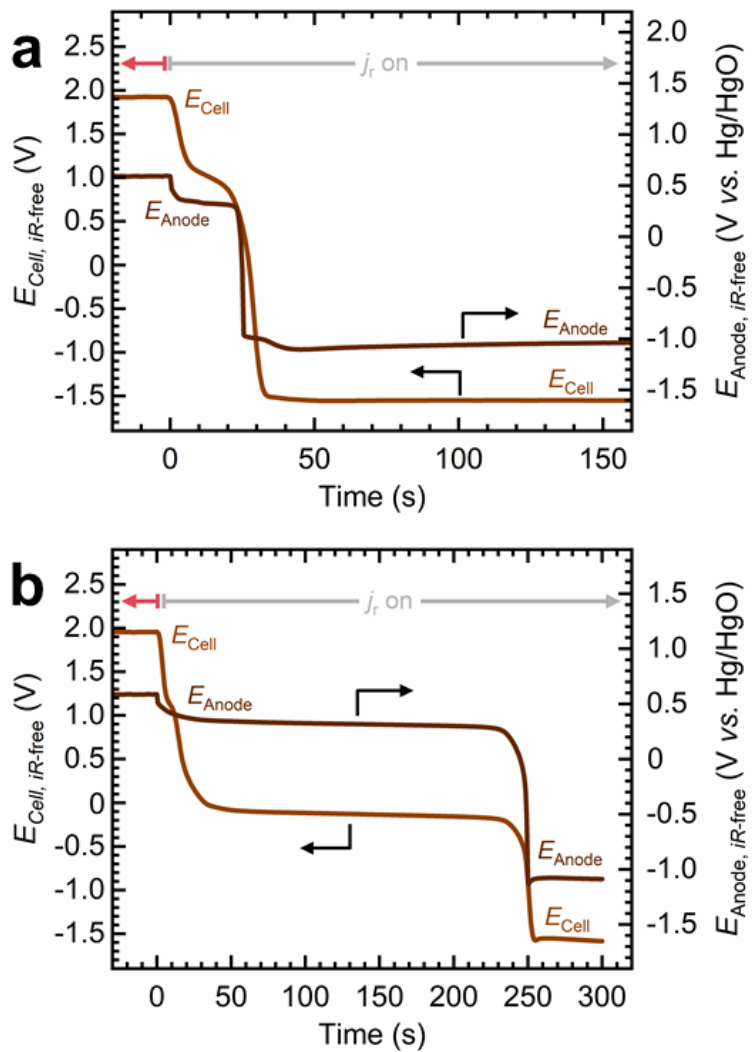


Figure S86. Decoupling the Fe-doped Ni mesh O₂ electrode (anode) potential during LAWE variable operation tests in a zero-gap alkaline water electrolyzer: Comparison of total cell potential (left y-axis) and anode potential (right y-axis) decay during the reverse current step (a) before and (b) after 240 cycles (experiment shown in **Figure S85**).

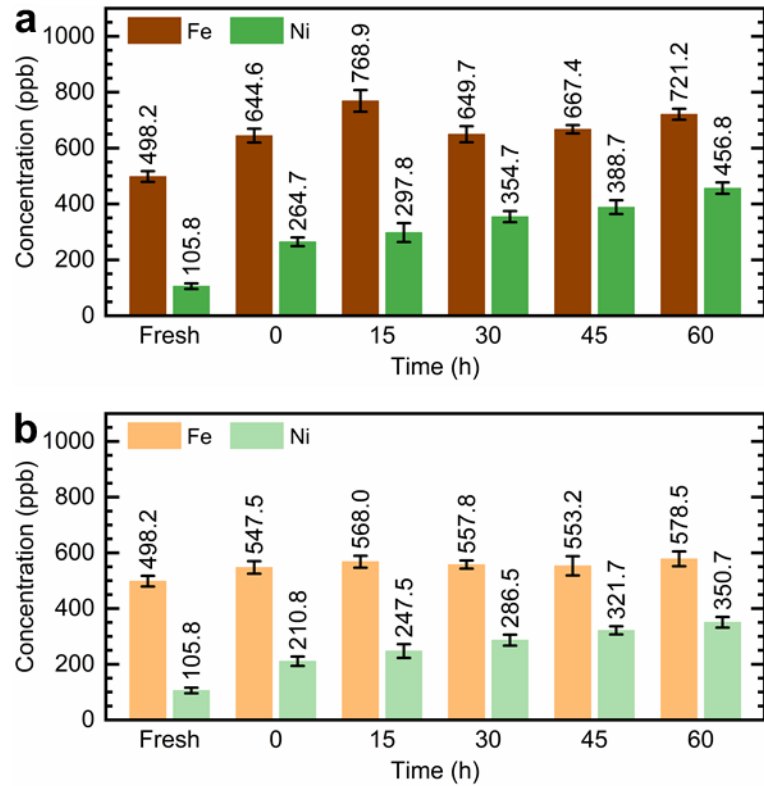


Figure S87. Ni and Fe concentrations in 7 M KOH electrolyte over cycling time during LAWE variable operation in a zero-gap electrolyzer, using a Fe-doped Ni mesh as the O₂ electrode: (a) metal concentrations in the anolyte (electrolyte recirculated on the O₂ electrode side) and (b) metal concentrations in the catholyte (electrolyte recirculated on the H₂ electrode side). Concentrations were determined via ex situ ICP-MS, with 250 µL electrolyte samples collected from the reservoirs at the specified intervals. Columns for the fresh condition represent the as-prepared KOH electrolyte, while time 0 corresponds to the electrolyte after 24 h of electrolyzer conditioning. Uncertainty bars represent the standard deviation from three replicate measurements.

Supporting note: Ni and Fe concentrations change significantly after conditioning, reflecting the formation of the (oxy)hydroxide layer. On the O₂ electrode, Fe is released into the electrolyte, possibly due to the dynamic exchange of Fe during conditioning until a more stable NiFe composition is achieved. Meanwhile, Ni is released due to oxidation. Ni and Fe concentrations steadily increase during cycling due to variable operation. Ni dissolution is more pronounced on the O₂ electrode, likely due to the stronger impact of polarity reversal on its thicker (oxy)hydroxide film than the H₂ electrode. Furthermore, the Fe concentration on the catholyte slowly increases at the beginning and then stabilizes, suggesting Fe crossover.

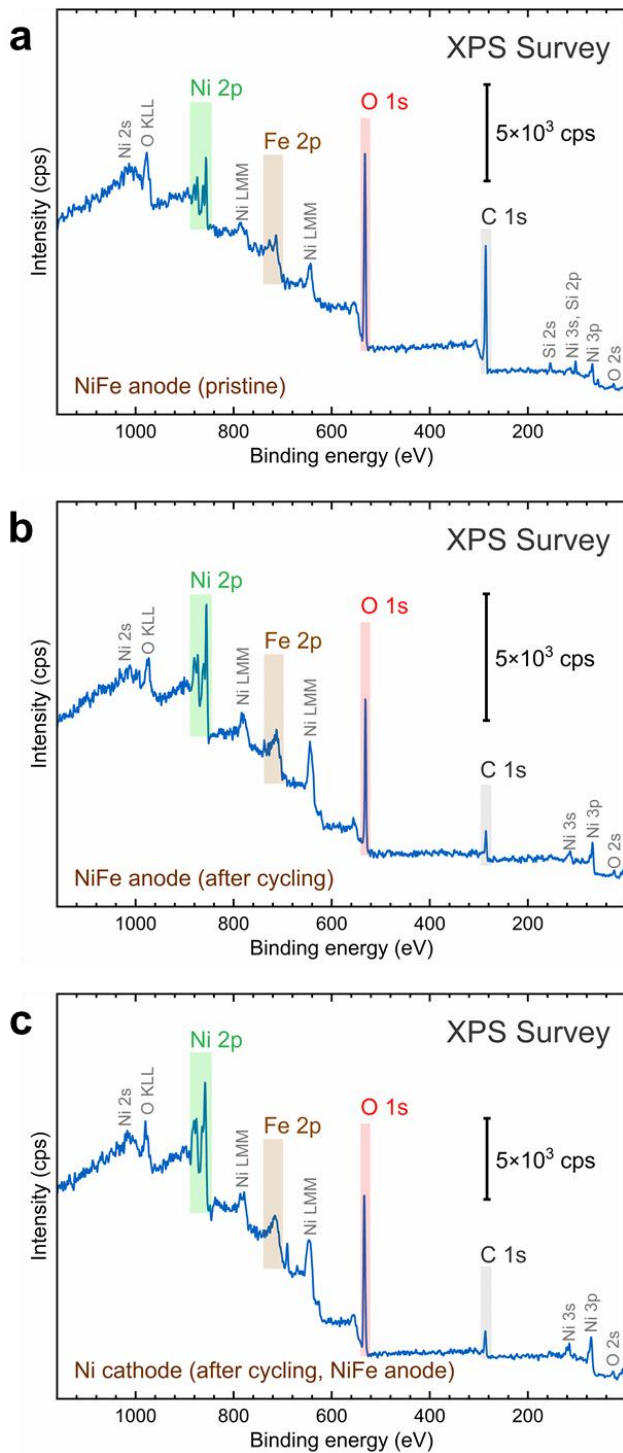


Figure S88. Ex situ XPS analysis of the Fe-doped Ni mesh O₂ electrode (anode) used in LAWE stability tests under variable operation in a zero-gap alkaline water electrolyzer: XPS survey scans of the (a) as-prepared Fe-doped Ni mesh O₂ electrode after conditioning; (b) Fe-doped Ni mesh O₂ electrode and (c) Ni mesh H₂ electrode (cathode) after 240 cycles.

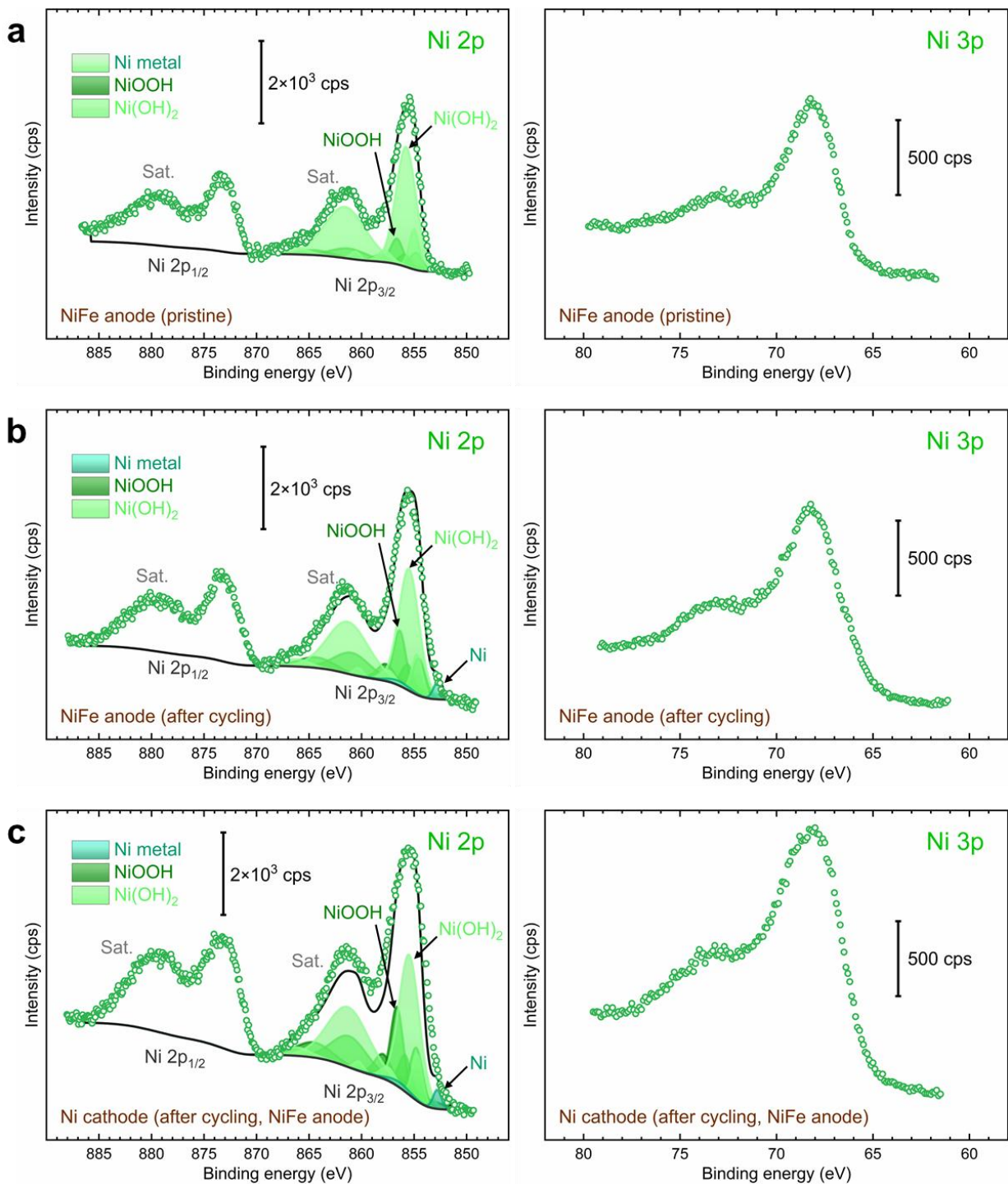


Figure S89. Ex situ XPS analysis of the Fe-doped Ni mesh O₂ electrode (anode) used in LAWE stability tests under variable operation in a zero-gap alkaline water electrolyzer: XPS spectra of the Ni 2p (left) and Ni 3p (right) regions for the (a) as-prepared Fe-doped Ni mesh anode after conditioning, (b) the Fe-doped Ni mesh anode, and (c) the Ni mesh H₂ electrode (cathode) after 240 cycles. Original XPS spectra are shown as open circles, while solid lines represent the fitted component envelopes. Individual components are color-coded for each species.

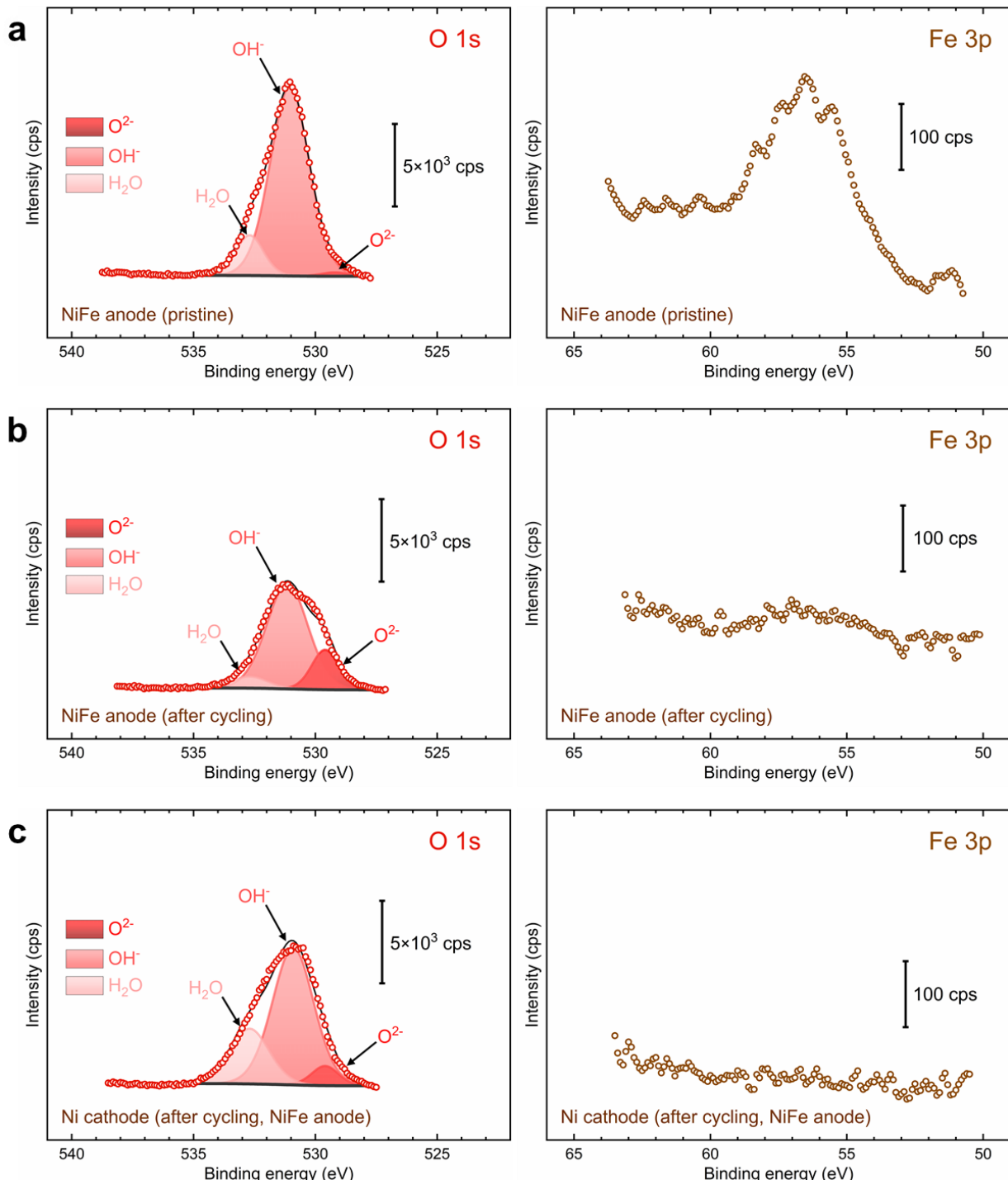


Figure S90. Ex situ XPS analysis of the Fe-doped Ni mesh O₂ electrode (anode) used in LAWE stability tests under variable operation in a zero-gap alkaline water electrolyzer: XPS spectra of the O 1s (left) and Fe 3p (right) regions for the (a) as-prepared Fe-doped Ni mesh anode after conditioning, (b) the Fe-doped Ni mesh anode, and (c) the Ni mesh H₂ electrode (cathode) after 240 cycles. Original XPS spectra are shown as open circles, while solid lines represent the fitted component envelopes. Individual components are color-coded for each species.

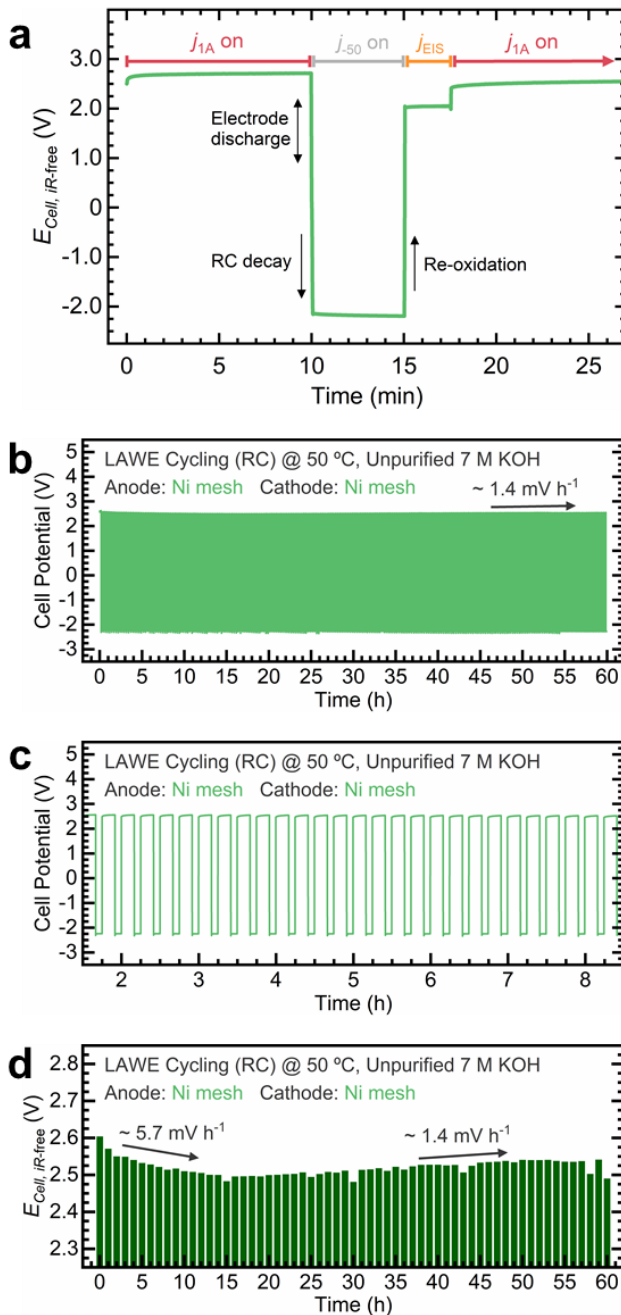


Figure S91. LAWE stability tests of Ni mesh electrodes under variable operation at high current density with a reverse current (RC) step in a zero-gap alkaline water electrolyzer: (a) Snapshot of a single cycle, showing a constant current step at $1 \text{ A}\cdot\text{cm}^{-2}$ followed by a reverse current step of $-50 \text{ mA}\cdot\text{cm}^{-2}$ to simulate shutdown, followed by an EIS measurement. (b) Full-cell potential progression over 240 cycles; (c) Detailed view of the cell potential profile under variable operation, revealing the reverse current steps with more detail. (d) iR -corrected cell potential throughout the stability test, with each bar representing the average potential during the constant current step per cycle. The arrows in (b) and (d) indicate the cell potential increase rate during the highlighted intervals. Experimental conditions: unpurified 7 M KOH electrolyte at 50 °C, $200 \text{ mL}\cdot\text{min}^{-1}$.

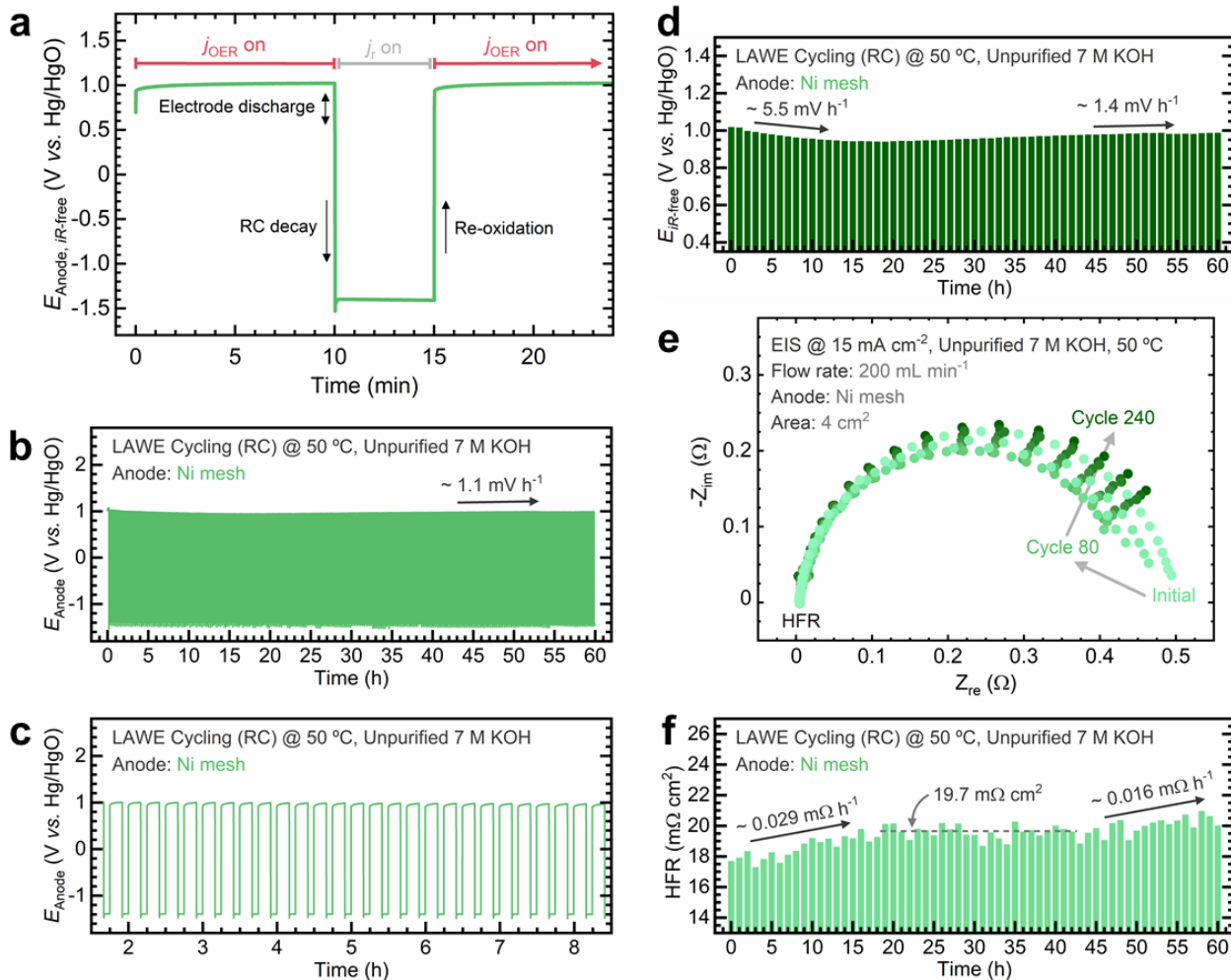


Figure S92. LAWE stability tests of the Ni mesh O₂ electrode (anode) under variable operation at high current density with a reverse current (RC) step in a zero-gap alkaline water electrolyzer: (a) Snapshot of a single cycle, showing a constant current step at 1 A·cm⁻² followed by a reverse current step of -50 mA·cm⁻² to simulate shutdown, followed by an EIS measurement; O₂ electrode potential progression over 240 cycles; (c) Detailed view of the O₂ electrode potential profile under variable operation, revealing the reverse current steps with more detail. (d) *iR*-corrected electrode potential throughout the stability test, with each bar representing the average potential during the constant current step per cycle. (e) Nyquist plots collected over the stability test. (f) HFR measured from Nyquist plots over the stability test. The grey arrows in (e) represent the evolution of the semicircle throughout the stability test. The arrows in (f) indicate the HFR increase rate during the highlighted interval, while the dashed line represents the average HFR value once stabilized. Experimental conditions: unpurified 7 M KOH electrolyte at 50 °C, 200 mL·min⁻¹, electrode area: 4 cm²_{geo}.

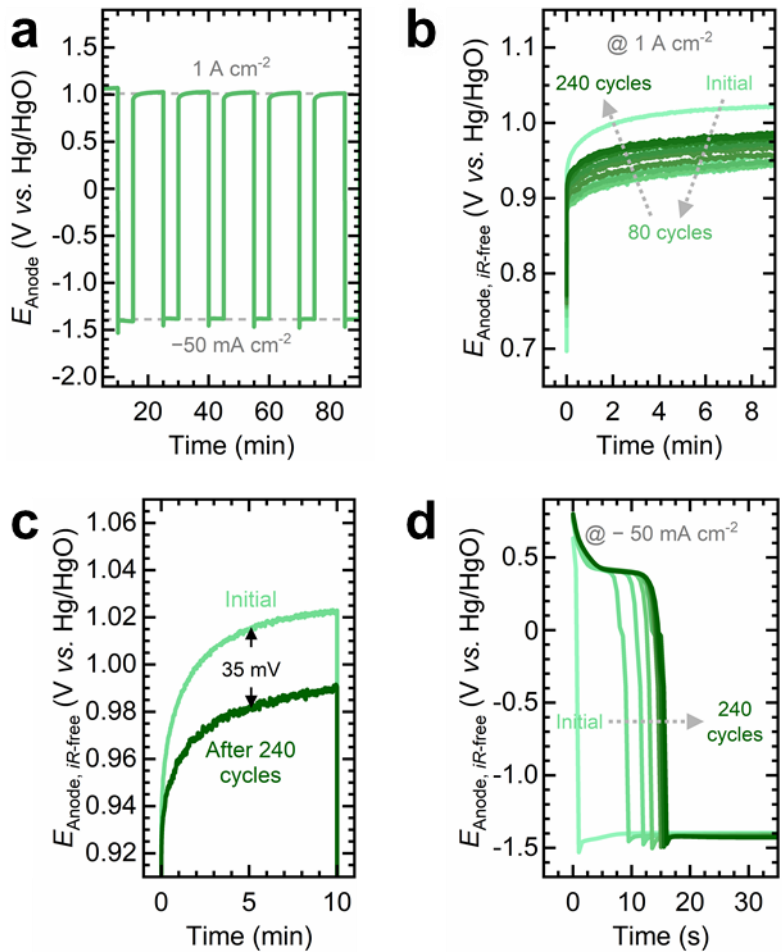


Figure S93. LAWE stability tests of the Ni mesh O₂ electrode (anode) under variable operation at $1 \text{ A}\cdot\text{cm}^{-2}$ with a reverse current (RC) step ($-50 \text{ mA}\cdot\text{cm}^{-2}$) in a zero-gap alkaline water electrolyzer: (a) Snapshot of the O₂ electrode potential profile under variable operation, highlighting the potential thresholds reached during the constant current and reverse current steps. (b) Comparison of the *iR*-corrected O₂ electrode potential across cycles. (c) *iR*-corrected O₂ electrode potential curves at the initial and final constant current steps, highlighting their potential differences. (d) Comparison of the *iR*-corrected O₂ electrode potential during the reverse current step across cycles. The arrows in (b) and (d) indicate the progression of potential profiles during cycling.

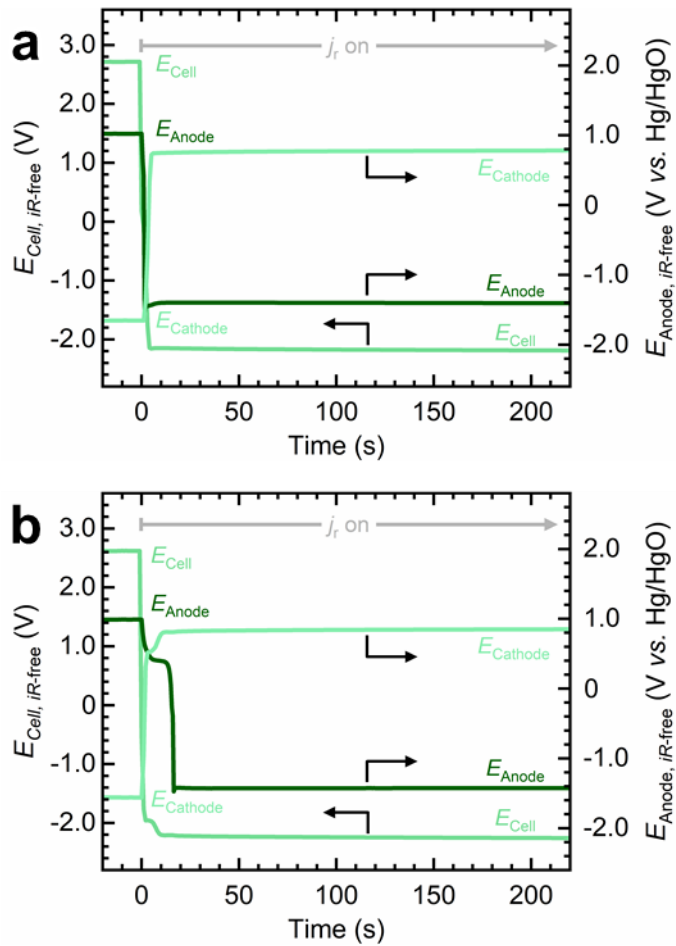


Figure S94. Decoupling the O_2 (anode) and H_2 (cathode) potentials during LAWE variable operation tests at $1\text{ A}\cdot\text{cm}^{-2}$ with a reverse current (RC) step ($-50\text{ mA}\cdot\text{cm}^{-2}$) in a zero-gap alkaline water electrolyzer: Comparison of total cell potential (left y-axis) and the anode/cathode potential (right y-axis) decay during the reverse current step (a) before and (b) after 240 cycles (experiment shown in **Figure S93**).

Supporting note: Despite not exhibiting a drastic decay in performance, the experiment at $1\text{ A}\cdot\text{cm}^{-2}$ reveals a more pronounced degradation compared to the test at $120\text{ mA}\cdot\text{cm}^{-2}$ (**Figures S68–S75**). At high current density, the total cell potential increases at a rate of $1.4\text{ mV}\cdot\text{h}^{-1}$ (**Figure S91**), which is seven times faster than the $0.2\text{ mV}\cdot\text{h}^{-1}$ observed under mild conditions (**Figure S68**). As shown in **Figure S92**, the O_2 electrode initially exhibits an electrode potential drop, confirmed by EIS: the semicircle in the Nyquist plots shrinks up to 80 cycles and then expands again. By contrast, the performance at mild current densities remains nearly constant over 240 cycles (**Figure S69**).

The initial decrease in the O_2 electrode potential, followed by a steady increase, can also be observed in **Figure S93**. The O_2 electrode at high currents initially drops by 35 mV, compared to 19 mV at mild currents (**Figure S70**). However, the potential stabilizes in the

mild current test after 240 cycles, whereas it continues to rise steadily in the high current test (**Figures S70b** and **S93b**). During the reverse current step, discharge behavior differs notably: the redox feature at high current density completes discharge in ~15 s (**Figure S93d**), while under mild conditions, the same takes ~100 s (**Figure S70d**). The negative potential at high current remains steady (nominally -1.4 V vs. Hg/HgO), while it becomes more positive over time in the mild test (from -1.0 to -0.8 V vs. Hg/HgO).

Figure S94 illustrates the decoupled potentials before and after 240 cycles, confirming NiOOH growth on the O₂ electrode. The longer discharge time indicates thicker NiOOH formation from repeated reoxidation. However, this time is still shorter than that observed at lower currents (**Figure S75**). The H₂ electrode also shows a small redox feature (**Figure S94b**), indicating NiOOH formation during the reverse current step. However, it is thinner than at the O₂ electrode and smaller than what is observed under mild conditions (**Figure S75b**).

These findings suggest that the more negative reverse current at high current density (-50 mA·cm⁻²) drives faster discharge of the NiOOH phase, rapidly shifting the electrode to reducing conditions. It is likely that the O₂ electrode—after successive reoxidation steps—undergoes full reduction to a metallic state. Due to challenging operating conditions (7 M KOH, 50 °C), we are unable to use our *in situ* SERS setup to confirm these changes. Further investigation into the structural evolution under industrial conditions is encouraged.

Nevertheless, the cell and electrode potential increase rates are clearly more severe near the end of high current density testing compared to mild conditions. This behavior may result from deeper reduction of the NiOOH layer on the O₂ electrode and concurrent NiOOH formation on the H₂ electrode. More work is needed to fully elucidate the consequences of these intensified transformations under high current operation.

References

- (1) Márquez, R. A.; Kawashima, K.; Son, Y. J.; Castelino, G.; Miller, N.; Smith, L. A.; Chukwuneke, C. E.; Mullins, C. B. Getting the Basics Right: Preparing Alkaline Electrolytes for Electrochemical Applications. *ACS Energy Lett.* **2023**, 8 (2), 1141–1146. <https://doi.org/10.1021/acsenergylett.2c02847>.
- (2) Trotochaud, L.; Young, S. L.; Ranney, J. K.; Boettcher, S. W. Nickel–Iron Oxyhydroxide Oxygen-Evolution Electrocatalysts: The Role of Intentional and Incidental Iron Incorporation. *J. Am. Chem. Soc.* **2014**, 136 (18), 6744–6753. <https://doi.org/10.1021/ja502379c>.
- (3) Kucernak, A. R.; Wang, H.; Lin, X. Avoid Using Phosphate Buffered Saline (PBS) as an Electrolyte for Accurate OER Studies. *ACS Energy Lett.* **2024**, 9 (8), 3939–3946. <https://doi.org/10.1021/acsenergylett.4c01589>.
- (4) Stevens, M. B.; Enman, L. J.; Batchellor, A. S.; Cosby, M. R.; Vise, A. E.; Trang, C. D. M.; Boettcher, S. W. Measurement Techniques for the Study of Thin Film Heterogeneous Water Oxidation Electrocatalysts. *Chem. Mater.* **2017**, 29 (1), 120–140. <https://doi.org/10.1021/acs.chemmater.6b02796>.
- (5) Burke, M. S.; Kast, M. G.; Trotochaud, L.; Smith, A. M.; Boettcher, S. W. Cobalt–Iron (Oxy)Hydroxide Oxygen Evolution Electrocatalysts: The Role of Structure and Composition on Activity, Stability, and Mechanism. *J. Am. Chem. Soc.* **2015**, 137 (10), 3638–3648. <https://doi.org/10.1021/jacs.5b00281>.
- (6) Hoang, T. T. H.; Gewirth, A. A. High Activity Oxygen Evolution Reaction Catalysts from Additive-Controlled Electrodeposited Ni and NiFe Films. *ACS Catal.* **2016**, 6 (2), 1159–1164. <https://doi.org/10.1021/acscatal.5b02365>.
- (7) Son, Y. J.; Marquez, R. A.; Kawashima, K.; Smith, L. A.; Chukwuneke, C. E.; Babauta, J.; Mullins, C. B. Navigating iR Compensation: Practical Considerations for Accurate Study of Oxygen Evolution Catalytic Electrodes. *ACS Energy Lett.* **2023**, 8 (10), 4323–4329. <https://doi.org/10.1021/acsenergylett.3c01658>.
- (8) Chen, R.; Yang, C.; Cai, W.; Wang, H.-Y.; Miao, J.; Zhang, L.; Chen, S.; Liu, B. Use of Platinum as the Counter Electrode to Study the Activity of Nonprecious Metal Catalysts for the Hydrogen Evolution Reaction. *ACS Energy Lett.* **2017**, 2 (5), 1070–1075. <https://doi.org/10.1021/acsenergylett.7b00219>.
- (9) Marquez, R. A.; Kalokowski, E.; Espinosa, M.; Bender, J. T.; Son, Y. J.; Kawashima, K.; Chukwuneke, C. E.; Smith, L. A.; Celio, H.; Dolocan, A.; Zhan, X.; Miller, N.; Milliron, D. J.; Resasco, J.; Mullins, C. B. Transition Metal Incorporation: Electrochemical, Structure, and Chemical Composition Effects on Nickel Oxyhydroxide Oxygen-Evolution Electrocatalysts. *Energy Environ. Sci.* **2024**, 17 (5), 2028–2045. <https://doi.org/10.1039/D3EE03617K>.
- (10) Marquez, R. A.; Espinosa, M.; Kalokowski, E.; Son, Y. J.; Kawashima, K.; Le, T. V.; Chukwuneke, C. E.; Mullins, C. B. A Guide to Electrocatalyst Stability Using Lab-Scale Alkaline Water Electrolyzers. *ACS Energy Lett.* **2024**, 9 (2), 547–555. <https://doi.org/10.1021/acsenergylett.3c02758>.
- (11) de Groot, M. T. Alkaline Water Electrolysis: With or without Iron in the Electrolyte? *Curr. Opin. Chem. Eng.* **2023**, 42, 100981. <https://doi.org/10.1016/j.coche.2023.100981>.

- (12) Demnitz, M.; Lamas, Y. M.; Garcia Barros, R. L.; de Leeuw den Bouter, A.; van der Schaaf, J.; Theodorus de Groot, M. Effect of Iron Addition to the Electrolyte on Alkaline Water Electrolysis Performance. *iScience* **2023**, 27 (1), 108695. <https://doi.org/10.1016/j.isci.2023.108695>.
- (13) Ehlers, J. C.; Feidenhans'l, A. A.; Therkildsen, K. T.; Larrazábal, G. O. Affordable Green Hydrogen from Alkaline Water Electrolysis: Key Research Needs from an Industrial Perspective. *ACS Energy Lett.* **2023**, 8 (3), 1502–1509. <https://doi.org/10.1021/acsenergylett.2c02897>.
- (14) Kawashima, K.; Márquez, R. A.; Son, Y. J.; Guo, C.; Vaidyula, R. R.; Smith, L. A.; Chukwuneke, C. E.; Mullins, C. B. Accurate Potentials of Hg/HgO Electrodes: Practical Parameters for Reporting Alkaline Water Electrolysis Overpotentials. *ACS Catal.* **2023**, 13 (3), 1893–1898. <https://doi.org/10.1021/acscatal.2c05655>.
- (15) Guruprasad, N.; van der Schaaf, J.; de Groot, M. T. Unraveling the Impact of Reverse Currents on Electrode Stability in Anion Exchange Membrane Water Electrolysis. *Journal of Power Sources* **2024**, 613, 234877. <https://doi.org/10.1016/j.jpowsour.2024.234877>.
- (16) Jerkiewicz, G. Standard and Reversible Hydrogen Electrodes: Theory, Design, Operation, and Applications. *ACS Catal.* **2020**, 10 (15), 8409–8417. <https://doi.org/10.1021/acscatal.0c02046>.
- (17) Feltham, A. M.; Spiro, M. Platinized Platinum Electrodes. *Chem. Rev.* **1971**, 71 (2), 177–193. <https://doi.org/10.1021/cr60270a002>.
- (18) Louie, M. W.; Bell, A. T. An Investigation of Thin-Film Ni–Fe Oxide Catalysts for the Electrochemical Evolution of Oxygen. *J. Am. Chem. Soc.* **2013**, 135 (33), 12329–12337. <https://doi.org/10.1021/ja405351s>.
- (19) Son, Y. J.; Kim, S.; Leung, V.; Kawashima, K.; Noh, J.; Kim, K.; Marquez, R. A.; Carrasco-Jaim, O. A.; Smith, L. A.; Celio, H.; Milliron, D. J.; Korgel, B. A.; Mullins, C. B. Effects of Electrochemical Conditioning on Nickel-Based Oxygen Evolution Electrocatalysts. *ACS Catal.* **2022**, 12 (16), 10384–10399. <https://doi.org/10.1021/acscatal.2c01001>.
- (20) Reference Test Method for Making Potentiodynamic Anodic Polarization Measurements. ASTM G5-14. ASTM International. **2014** <https://doi.org/10.1520/G0005-14>.
- (21) Practice for Conventions Applicable to Electrochemical Measurements in Corrosion Testing. ASTM G3-14. ASTM International. **2014** <https://doi.org/10.1520/G0003-14>.
- (22) Test Method for Conducting Potentiodynamic Polarization Resistance Measurements. ASTM G59-97 (Reapproved 2014). ASTM International. **2014** <https://doi.org/10.1520/G0059-97R14>.
- (23) Practice for Calculation of Corrosion Rates and Related Information from Electrochemical Measurements. ASTM G102-89 (Reapproved 2015). ASTM International. **2015** <https://doi.org/10.1520/G0102-89R15E01>.
- (24) van Limpt, R. T. M.; Lavorenti, M.; Verheijen, M. A.; Tsampas, M. N.; Creatore, M. Control by Atomic Layer Deposition over the Chemical Composition of Nickel Cobalt Oxide for the Oxygen Evolution Reaction. *J. Vac. Sci. Technol. A* **2023**, 41 (3), 032407. <https://doi.org/10.1116/6.0002414>.
- (25) Aleman, A. M.; Crago, C. F.; Kamat, G. A.; Mule, A. S.; Avilés, J. E.; Matthews, J. E.; Keyes, N.; Hannagan, R. T.; Nielander, A. C.; Stevens, M. B.; Jaramillo, T. F. Multimodal in Situ Characterization Uncovers Unexpected Stability of a Cobalt Electrocatalyst for Acidic Sustainable Energy Technologies. *J. Am. Chem. Soc.* **2025**, In Press.

- (26) Yan, K.; Lee, S.-W.; Yap, K. M. K.; Mule, A. S.; Hannagan, R. T.; Matthews, J. E.; Kamat, G. A.; Lee, D. U.; Stevens, M. B.; Nielander, A. C.; Jaramillo, T. F. On-Line Inductively Coupled Plasma Mass Spectrometry Reveals Material Degradation Dynamics of Au and Cu Catalysts during Electrochemical CO_2 Reduction. *J. Am. Chem. Soc.* **2025**. <https://doi.org/10.1021/jacs.4c13233>.
- (27) Sakas, G.; Ibáñez-Rioja, A.; Pöyhönen, S.; Kosonen, A.; Ruuskanen, V.; Kauranen, P.; Ahola, J. Influence of Shunt Currents in Industrial-Scale Alkaline Water Electrolyzer Plants. *Renewable Energy* **2024**, 225, 120266. <https://doi.org/10.1016/j.renene.2024.120266>.
- (28) Rasten, E. (Invited) Shunt-Currents in Alkaline Water-Electrolyzers and Renewable Energy. *ECS Trans.* **2024**, 113 (9), 25–41. <https://doi.org/10.1149/11309.0025ecst>.
- (29) Bernt, M.; Gasteiger, H. A. Influence of Ionomer Content in IrO₂/TiO₂ Electrodes on PEM Water Electrolyzer Performance. *J. Electrochem. Soc.* **2016**, 163 (11), F3179. <https://doi.org/10.1149/2.0231611jes>.
- (30) Bernt, M.; Siebel, A.; Gasteiger, H. A. Analysis of Voltage Losses in PEM Water Electrolyzers with Low Platinum Group Metal Loadings. *J. Electrochem. Soc.* **2018**, 165 (5), F305–F314. <https://doi.org/10.1149/2.0641805jes>.
- (31) Bender, G.; Carmo, M.; Smolinka, T.; Gago, A.; Danilovic, N.; Mueller, M.; Ganci, F.; Fallisch, A.; Lettenmeier, P.; Friedrich, K. A.; Ayers, K.; Pivovar, B.; Mergel, J.; Stolten, D. Initial Approaches in Benchmarking and Round Robin Testing for Proton Exchange Membrane Water Electrolyzers. *Int. J. Hydrogen Energy* **2019**, 44 (18), 9174–9187. <https://doi.org/10.1016/j.ijhydene.2019.02.074>.
- (32) Ju, W.; Heinz, M. V. F.; Pusterla, L.; Hofer, M.; Fumey, B.; Castiglioni, R.; Pagani, M.; Battaglia, C.; Vogt, U. F. Lab-Scale Alkaline Water Electrolyzer for Bridging Material Fundamentals with Realistic Operation. *ACS Sustainable Chem. Eng.* **2018**, 6 (4), 4829–4837. <https://doi.org/10.1021/acssuschemeng.7b04173>.
- (33) Möckl, M.; Ernst, M. F.; Kornherr, M.; Allebrod, F.; Bernt, M.; Byrknes, J.; Eickes, C.; Gebauer, C.; Moskovtseva, A.; Gasteiger, H. A. Durability Testing of Low-Iridium PEM Water Electrolysis Membrane Electrode Assemblies. *J. Electrochem. Soc.* **2022**, 169 (6), 064505. <https://doi.org/10.1149/1945-7111/ac6d14>.
- (34) Biesinger, M. C.; Payne, B. P.; Lau, L. W. M.; Gerson, A.; Smart, R. St. C. X-Ray Photoelectron Spectroscopic Chemical State Quantification of Mixed Nickel Metal, Oxide and Hydroxide Systems. *Surf. Interface Anal.* **2009**, 41 (4), 324–332. <https://doi.org/10.1002/sia.3026>.
- (35) Biesinger, M. C.; Payne, B. P.; Grosvenor, A. P.; Lau, L. W. M.; Gerson, A. R.; Smart, R. St. C. Resolving Surface Chemical States in XPS Analysis of First Row Transition Metals, Oxides and Hydroxides: Cr, Mn, Fe, Co and Ni. *Applied Surface Science* **2011**, 257 (7), 2717–2730. <https://doi.org/10.1016/j.apsusc.2010.10.051>.
- (36) Grosvenor, A. P.; Biesinger, M. C.; Smart, R. St. C.; McIntyre, N. S. New Interpretations of XPS Spectra of Nickel Metal and Oxides. *Surf. Sci.* **2006**, 600 (9), 1771–1779. <https://doi.org/10.1016/j.susc.2006.01.041>.
- (37) Glenn, J. R.; Lindquist, G. A.; Roberts, G. M.; Boettcher, S. W.; Ayers, K. E. Standard Operating Procedure for Post-Operation Component Disassembly and Observation of Benchtop Water Electrolyzer Testing. *Front. Energy Res.* **2022**, 10. <https://doi.org/10.3389/fenrg.2022.908672>.

- (38) Jain, A.; Ong, S. P.; Hautier, G.; Chen, W.; Richards, W. D.; Dacek, S.; Cholia, S.; Gunter, D.; Skinner, D.; Ceder, G.; Persson, K. A. Commentary: The Materials Project: A Materials Genome Approach to Accelerating Materials Innovation. *APL Materials* **2013**, *1* (1), 011002. <https://doi.org/10.1063/1.4812323>.
- (39) Singh, A. K.; Zhou, L.; Shinde, A.; Suram, S. K.; Montoya, J. H.; Winston, D.; Gregoire, J. M.; Persson, K. A. Electrochemical Stability of Metastable Materials. *Chem. Mater.* **2017**, *29* (23), 10159–10167. <https://doi.org/10.1021/acs.chemmater.7b03980>.
- (40) Patel, A. M.; Nørskov, J. K.; Persson, K. A.; Montoya, J. H. Efficient Pourbaix Diagrams of Many-Element Compounds. *Phys. Chem. Chem. Phys.* **2019**, *21* (45), 25323–25327. <https://doi.org/10.1039/C9CP04799A>.
- (41) Persson, K. A.; Waldwick, B.; Lazic, P.; Ceder, G. Prediction of Solid-Aqueous Equilibria: Scheme to Combine First-Principles Calculations of Solids with Experimental Aqueous States. *Phys. Rev. B* **2012**, *85* (23), 235438. <https://doi.org/10.1103/PhysRevB.85.235438>.